MINISTÉRIO DA EDUCAÇÃO
UNIVERSIDADE FEDERAL DO RIO GRANDE DO SUL
PROGRAMA DE PÓS-GRADUAÇÃO EM ENGENHARIA MECÂNICA

ANALYSIS OF STATIONARY AND NON-STATIONARY PHENOMENA IN TURBULENT SUBCRITICAL FLOW BEHIND TWO PARALLEL CYLINDERS

por

Ana Paula Ost

Tese para obtenção do Título de
Doutora em Engenharia

Porto Alegre, 01 de fevereiro de 2022

ANÁLISE DE FENÔMENOS ESTACIONÁRIOS E NÃO ESTACIONÁRIOS EM ESCOAMENTOS TURBULENTOS

por

Ana Paula Ost
Mestra em Engenharia Mecânica

Tese submetida ao Programa de Pós-Graduação em Engenharia Mecânica, da Escola de Engenharia da Universidade Federal do Rio Grande do Sul, como parte dos requisitos necessários para a obtenção do Título de

Doutora em Engenharia

Área de Concentração: Fenômenos de Transporte

Orientador: Prof. Dr. Sérgio Viçosa Möller

Aprovada por:

Prof. Dr. Celso Pupo Pesce, ...POLI/USP

Prof.ª Dr.ª Maria Luiza Sperb Indrusiak,................................Consultoria Independente

Prof. Dr. Herbert Martins Gomes,..PROMEC/UFRGS

Prof. Dr. Bardo Ernst Josef Bodmann..PROMEC/UFRGS

Prof. Dr. Fernando Marcelo Pereira
Coordenador do PROMEC

Porto Alegre, 01 de fevereiro de 2022

“The reality we can put into words is never reality itself.”
Werner Heisenberg

Science cannot solve the ultimate mystery of nature.
And that is because, in the last analysis,
we ourselves are a part of the mystery
that we are trying to solve.

Max Planck

"Forty-two," said Deep Thought (...) "I checked it very thoroughly,"
(...)"and that quite definitely is the answer.
I think the problem, to be quite honest with you,
is that you've never actually known what the question is.”

— Douglas Adams, The Hitchhiker's Guide to the Galaxy

AGRADECIMENTOS

Agradeço ao meu orientador professor Dr. Sérgio V. Möller, por seus sábios conselhos e ao professor Dr. Bardo Bodmann pelo auxílio teórico para compreensão dos conceitos de caos aplicados neste trabalho. Agradeço também aos meus colegas de laboratório, especialmente a Drª Roberta F. Neumeister por toda ajuda e colaboração. Um muito obrigada ao professor Dr. Alexandre V. de Paula por contribuir com este trabalho cedendo uma parte de seu algoritmo para a análise estatística dos sinais. Um agradecimento especial ao Dr. Luiz Felipe F. Chaves Barcelos pela parceria, pela paciência, por ouvir incontáveis discussões sobre resultados e pelos preciosos *insights* nos momentos de dúvida. Obrigada a Capes pelo apoio financeiro.

ABSTRACT

This study presents the analysis of the bistable phenomenon for turbulent flows around two cylinders side-by-side using two methods for data analysis and chaos theory for dynamic analysis. The experimental data were acquired for various Reynolds numbers and pitch-to-diameter ratio p/D of 1.16, 1.26, and 1.60, cylinders diameter was 25.1 mm. The experimental technique consists of measuring the velocity fluctuations in an aerodynamic channel using hot-wire anemometry. The study presents the application of the Hilbert-Huang transform (HHT) as a tool of analysis for non-stationary and non-linear signals. The method was first validated using single cylinders and then extended for two cylinders side-by-side. Results show that the HHT method may provide information about particular events in time-frequency space and about the physics of flow scales. The statistical analysis of the experimental data is performed to identify statistical patterns that can be used to characterize the bistable flow. The signals are scanned by a moving window for the statistical analysis, creating blocks of probability density functions (PDFs). The four first statistical moments of each PDF are calculated, and a tendency of behavior based on their variations is established. The dynamics of the bistable flow system are studied applying chaos theory tools, like the largest Lyapunov exponent. The strange attractors of the velocity-time series are reconstructed, and their topology is useful to understand the physics of the bistable system. Each flow wake mode is analyzed separately. A general model of the bistable flow is reconstructed using probability functions. The application of a set of tools in the analysis of the turbulent wake behind cylinders is useful for the comprehension of turbulent phenomena, producing meaningful results and allowing the identification of turbulent structures and flow scales, and a better understanding of the system dynamics.

Keywords: Hilbert-Huang transform, Empirical Mode Decomposition, Bistability, Chaos theory, Dynamic systems.

RESUMO

Este estudo apresenta a análise do fenômeno da biestabilidade no escoamento em torno de dois cilindros lado a lado usando dois métodos para análise de sinais, e teoria do caos para a análise da dinâmica. Os dados experimentais foram adquiridos para vários números de Reynolds e várias razões de aspecto p/D de 1,16, 1,26 e 1,60, o diâmetro dos cilindros é de 25,1 mm. A técnica experimental utilizada consiste em medir as flutuações de velocidade em um canal aerodinâmico utilizando anemometria de fio quente. O estudo apresenta a aplicação da transformada de Hilbert-Huang (HHT) como ferramenta de análise para sinais não estacionários e não lineares. O método é primeiramente validado utilizando sinais experimentais para um cilindro sobre escoamento turbulento e após aplicado ao escoamento sobre dois cilindros lado a lado. Resultados mostram que o método de HHT fornece não só uma definição mais precisa de eventos específicos no espaço tempo-frequência, mas também permite uma interpretação física mais significativa dos processos dinâmicos das escalas do escoamento. A análise estatística dos dados experimentais é feita com o objetivo de identificar padrões estatísticos que possam ser utilizados para caracterização do escoamento biestável. Para a análise estatística os dados são varridos por uma janela móvel, criando blocos de funções densidade de probabilidade (PDFs). Os quatro primeiros momentos estatísticos são calculados e é possível estabelecer uma tendência de comportamento baseada em suas variações. A dinâmica do sistema biestável é estudada aplicando ferramentas da teoria do caos, como o maior expoente de Lyapunov. O atrator estranho da série temporal da velocidade é reconstruído e sua topologia é utilizada para melhor compreensão do comportamento físico do fenômeno da biestabilidade. Cada esteira do escoamento biestável é analisada separadamente. Um modelo geral do escoamento biestável é reconstruído utilizando funções de probabilidade. A aplicação de um conjunto de ferramentas para a análise da turbulência das esteiras dos cilindros é útil para a melhor compreensão de fenômenos turbulentos, produzindo resultados significativos e permitindo a identificação de estruturas turbulentas e escalas do escoamento e um entendimento sobre a dinâmica do sistema.

Palavras-chave: Transformada de Hilbert-Huang, *Empirical Mode Decomposition*, Biestabilidade, Teoria do Caos, Sistemas Dinâmicos.

SUMMARY

FIGURES LIST

LIST OF ACRONYMS AND ABBREVIATIONS

2D	*Two dimensional*
3D	*Three dimensional*
CGT	*Counter-gradient transport*
CWT	*Continuous wavelet transform*
DWPT	*Discrete wavelet packet transform*
DWT	*Discrete Wavelet Transform*
EEMD	*Ensemble Empirical Mode Decomposition*
EMD	*Empirical Mode Decomposition*
FIV	*Flow-induced Vibration*
FFN	*False Nearest Neighbor*
FFT	*Fast Fourier Transform*
HHT	*Hilbert-Huang transform*
HSA	*Hilbert Spectral Analysis*
IMF	*Intrinsic Mode Function*
LES	*Large-eddy simulations*
MEMS	*Micro Electro Mechanical Systems*
MSE	*Mean Square Energy*
NA	*Not available or Not applicable*
NHES	*Normalized Hilbert Energy Spectra*
NHSA	*Normalized Hilbert Spectral Analysis*
NHT	*Normalized Hilbert Transform*
PDF	*Probability Density Function*
PIV	*Particle Image Velocimetry*
PSD	*Power Spectral Density*
USB	*Universal Serial Bus*
VIV	*Vortex-induced vibration*

SYMBOL LIST

$\langle u \rangle$	Mean velocity [m/s]
$a(t)$	Instantaneous amplitude
$a_j(t)$	Instantaneous amplitude of the j^{th} IMF component [m/s]
B	Aerodynamic channel width [m]
b/a	Spacing ratio in Kármán-Bénard street
c_1,c_n	First IMF component after EMD, same as h_{1k}, n^{th} IMF component.
C_d	Drag coefficient
C_f	Skin friction coefficient or torque coefficient
$C_f(t)$	Normalized IMF or carrier function
$c_i(t)$	Intrinsic mode function, where i is the number of the IMF
$c_j(t)$	Ensemble mean of the j^{th} IMF
$c_{ji}(t)$	The j^{th} IMF component of the i^{th} realization of noise-added data
C_l	Lift coefficient
C_p	Pressure coefficient
C_{pb}	Base pressure coefficient
D	Diameter [m]
e	Absolute Roughness
$E(t)$	Spline envelop for normalized HHT
f	Vortex shedding frequency [Hz]
$f(t)$	Generic function
F	Power spectra frequency vector
$F(\omega)$	Fourier spectrum of the signal
$F_q(\omega)$	Fourier spectrum of the quadrature function
$g(t)$	Generic function
$h(\omega)$	Marginal Hilbert spectrum
$H(\omega, t)$	Hilbert Energy spectrum
h_1, h_{1k}	The first component of EMD decomposition, IMF component after repeating sifting k times
k	Wavenumber
$k*$	Dimensionless wavenumber

L	Aerodynamic channel height [m]
L_f	Vortex length of the formation
m_1, m_{1k}	Mean between upper and lower envelopes, mean after repeating sifting k^{th} times
n	Number of steps in the Empirical Mode Decomposition
N	Number of trials of the decomposition, length of time series
p	Pitch, distance between cylinders center [m]
P	Cauchy principal value
r_1, r_j	First residue component, subsequent results.
Re	Reynolds number [UD/n]
$r_k(t)$	Residue after k^{th} trials of the EEMD
$r_{ki}(t)$	Residue after extracting k IMFs in the i^{th} realization of the noise added data
$r_n(t)$	Residue after n^{th} sifting times
St	Strouhal number [fD/U]
T	Sampling time [s], period
t, t'	Time [s]
Tu	Turbulence intensity (%)
U	Free stream velocity or reference velocity [m/s]
u	Mean velocity along axis x.
u'	Fluctuating velocity component in axis x
u_{rms}	Root mean square of velocity component in axis x.
v	Mean velocity along y.
v_{rms}	Root mean square of velocity component in y.
w	Transversal distance [m]
$w_i(t)$	Noise series
x	Downstream distance [m]
$x(t)$	Data expressed in IMF form
$X(t)$, $X(t')$	Time series
$X_H(t)$	IMF data after Hilbert-transform
$xh(t)$	Hilbert transform of $x(t)$
$X_i(t)$	The i^{th} observation of the noise added time series
$xq(t)$	Quadrature of the signal $x(t)$
$Y(t)$	Hilbert transform of time series

$Y_i(t)$	Normalized IMF
$Z(t)$	Analytical signal
$\Delta E(t)$, ΔE	Error index
$\theta(t)$	Phase function
v	Kinematic viscosity [m²/s]
$\Phi(f)$	Energy spectrum as a frequency function [m^2/s]
$\Phi(k)$	Energy spectrum as a wavenumber function [m^2/s]
$\Phi^*(k^*)$	Dimensionless energy spectrum
$\omega(t)$	Instantaneous frequency [Hz]
$\omega_j(t)$	Instantaneous frequency of the j^{th} IMF component [Hz]

1 INTRODUCTION

Single cylinders and cylinder arrangements can simulate a wide range of practical situations, such as tube heat exchangers, chimney groups, cores of nuclear reactors, and offshore platforms. Two side-by-side cylinders are a classical representation of multiple structures, and the understanding of the flow around them can be enlightening for the comprehension of the flow around those structures.

The cross-flow through circular cylinders of the same diameter placed side-by-side can present a wake with different modes, depending on the pitch-to-diameter ratio p/D [Sumner et al., 1999]. For intermediate pitch ratios ($1.2 < p/D < 2.0$), the flow is characterized by a wide near-wake behind one of the cylinders and a narrow near-wake behind the other. This phenomenon generates two dominant vortex shedding frequencies; the lower frequency associated with the wide wake and the higher frequency with the narrow wake. The gap flow is biased towards the back of the cylinders, switches sides, from one side to the other, at irregular time intervals. This switching of the gap flow is known as bistability.

Reviews on two-cylinder flows were made by Zdravkovich, 1977; Sumner, 2010, and more recently by Zhou and Alam, 2016, where the effects of the space rations p/D, the orientations concerning the flow incidence, and the Reynolds number were investigated. A collection of previous results for many configurations were presented and made clear that the flow around two cylinders is complex and still has many aspects that need investigation.

Experimental evidence was found by De Paula and Möller, 2018, that the flow through two cylinders or tube banks showed the presence of instabilities associated with the bistability phenomenon. Even though the dynamics of the bistability are not completely understood, their results showed the presence of positive Lyapunov exponents evidencing that bistability has a chaotic behavior.

Instabilities in the wake of two cylinders have been the subject of studies for decades. The theory of instability was studied by authors like Parkinson and Smith, 1964, and Novak, 1969, 1972. The experimental part also receives attention, especially the study of instability features of bluff bodies with different cross-sections. Those studies are interesting because bluff bodies are simplifications of structural elements, like buildings for example. Consequently, when designing certain structures such as particularly high and slender buildings, one may find that critical velocities of aeroelastic instabilities such as vortex-induced excitation and galloping are within the design wind speed [Alam and Meyer, 2013].

Strange attractors have been used in the study of turbulent flow especially since Lorenz's studies, Lorenz, 1963. Ruelle and Takens, 1971 were some of the first to suggest that strange attractors could arise after a finite sequence of bifurcations and might provide a model for turbulent motion. Since then, many theories and methodologies were created to allow the dynamical analysis of experimental data for turbulent flows using chaos theory.

Engineering and many other areas require data analysis as a mean to determine parameters necessary to construct models and to confirm those models represent the phenomenon. Data analysis is an indispensable step in understanding the physical processes. Usually, this data is analyzed using tools that are either for linear but nonstationary processes such as wavelets [Cohen, 1995; Daubechies, 1992] and Fourier analysis [Flandrin, 1999a; Bendat and Piersol, 2010] or nonlinear but stationary and statistically deterministic processes like the methods summarized by Tong, 1993; Diks, 1999; and Kantz and Schreiber, 2004.

The Fourier analysis is one of the major accomplishments of physics and mathematics. Historically, Fourier spectral analysis has provided a general method for examining the global energy-frequency distributions. Its mathematical structure is naturally suited to common transform methods through its simplicity and has collaborated to the development of a large number of algorithms, programs, processors, and machines for frequency analysis. However Fourier analysis has some limitations, and restrictions concerning its physical interpretations and its range of applicability: to localize an event in time, the window width must be narrow, and the frequency resolution requires a longer time series, limiting its applicability. By performing the Fourier transform the signal is projected in the frequency domain, losing the link with the time domain, falling in the Heisenberg uncertainty principle [Flandrin, 1999a; Abbate et al., 2002; Huang et al., 1998].

Wavelet transform arises from the idea of stretching and compressing the window of the windowed Fourier transform, to better fit the frequencies to be localized, hence allowing the definition of the scales in time and frequency domains, [Indrusiak and Möller, 2011]. Continuous or discrete, wavelet analysis is basically a linear analysis for non-stationary data. The method is very suitable for analyzing data with gradual frequency changes, and one of the many characteristics is that it provides a uniform resolution for all scales; however, the time scale has also uniformly poor resolution. It has many applications in edge detection and image compression, limited applications in time-frequency distribution in time series [Indrusiak et al., 2005; Indrusiak et al., 2016; Farge, 1992]. One of many disadvantages of the method is the choice of the appropriated wavelet and the interpretation of the results. As an example given by Huang et al., 1998, to define a change occurring locally, one must look for the high-frequency range, for the higher the frequency the more localized the basic wavelet will be. If a local event occurs only in the low-frequency range, one will still be forced to look for its effects in the high-frequency range, and this effect may difficult to correct physical interpretation. Besides, due to its non-adaptive nature, once the basic wavelet is chosen, one will use it to analyze the whole data and it can only give a physically meaningful interpretation for linear phenomena.

Nevertheless, most of the real data is nonlinear and nonstationary and the analysis tools are limited, and those nonlinear processes need special treatment. The development of the Hilbert-Huang transform was motivated to overcome these problems of data analysis since it is not limited by linearity or stationarity and has an adaptive base, based and derived from the data itself. Besides periodicity, is attempted to learn the detailed dynamics in processes of the data. The Hilbert-Huang transform reveals one of the typical characteristics of nonlinear processes, mentioned by Huang et al., 1998, its intra-wave frequency modulation, which indicates that the instantaneous frequency changes within one oscillation cycle.

1.1 Objectives

Based on the previous information this work objectives constitutes of:

1. Evaluate and explore the use of Hilbert-Huang transform as a tool for signal analysis, since bistable flow is a non-stationary, non-linear and chaotic phenomenon. Therefore, HHT was first tested in a turbulent flow around single cylinders due to its well-known features. When applied on single cylinders HHT was successful in identifying turbulent flow aspects like coherent structures, vortex shedding frequencies, and flow scales, proving to be a potential method of analysis.
2. Evaluate the bistable signal from a dynamic perspective, using information such as the largest Lyapunov exponent, embedding dimension, and statistical methods for strange attractors.
3. Identifying the physical parameters that influenced on the bistable dynamics and chaotic characteristics, and provide a way for reconstructing the general dynamics of bistable flows without the need of a differential equation.

2 LITERATURE REVIEW

This section discusses some of the main studies about the bistable phenomenon, some applications of the chaos theory in the studies of turbulence, and the most important developments on the Hilbert-Huang transform, main applications, and previous studies regarding turbulent systems.

2.1 Bistability

Many studies have researched multiple cylinder configurations immersed in steady cross-flow. One of the earliest experiments studies, on two circular cylinders in tandem and side-by-side configurations, was performed by Biermann and Herrnstein, 1934, who were interested in the interference effects of airplane struts.

Spivack, 1946 studied the vortex frequency and the flow pattern in the wake of two parallel cylinders for various Reynolds numbers and varying the spacing ratio G/d, where G is the gap distance between the cylinders, and d is the diameter. The author presented an analysis on the Strouhal number as a function of G/d and as a function of the Reynolds number. No dependency on the Reynolds was found for values higher than $15\text{x}10^3$. For the Strouhal number, the values were considered constant, except for $G/d < 1$. For $G/d = 0.454$ low and higher frequencies were found.

Bearman and Wadcock, 1973 identified the presence of intermittence in the random switching of the biased gap flow of two cylinders placed side-by-side. They called this phenomenon bistability.

When two circular cylinders of equal diameter D, are arranged in a side-by-side configuration in steady cross flow of velocity U, they exhibit asymmetrical flow pattern for intermediate values of pitch to diameter ratio $1.1 – 1.3 < p/D < 2.2 – 2.5$. The asymmetrical flow pattern is characterized by a narrow near wake region behind one of the cylinders, a wide near wake behind the other cylinder, and two dominant vortex shedding frequencies. The biased flow pattern switches intermittently from one cylinder to the other being called bistable. At smaller pitch to diameter ratios ($p/D < 1.1 – 1.3$), the two cylinders act similarly to a single bluff body, whereas for higher pitch ratios ($p/D > 2.2 – 2.5$) the flow field behaves as two single bodies. A complex vortex street interaction in the combined wake of the bodies can be found because of the existence of two or more simultaneous side-by-side vortex shedding processes. Usually, the vortex streets are synchronized in an anti-phase configuration, in which vortices are shed simultaneously on both sides of the gap between the cylinders. In-phase vortex shedding synchronization may also happen, according to Sumner et al., 1999.

Kim and Durbin, 1988 studied the flow for the range of spacing ratios $0.1 < G/d < 1$, where G is the gap distance. They described the bistable phenomenon as a flow that flip-flopped between two quasi-stable, asymmetric states which are separated by an unstable symmetric state. When they positioned a plate in the centreline of the cylinders, the flopping stopped and hysteresis between the asymmetric flow was observed. Studying the interval between mode changes, they verified that the mean time between mode changing decreases exponentially with increasing Reynolds, following a Poisson stochastic model, and that the time-scale of the mode change several orders of magnitude longer than the vortex shedding time scale. The presence of two independent vortex shedding frequencies for each wake mode was also observed.

Guillaume and LaRue, 1999 concluded in their study that the transition between the asymmetric states of the flow between two cylinders in the flopping regime is completely random and is not associated with a natural frequency. According to them the time between transitions is in the order of 10^3 times longer than the vortex shedding period, and the mean time interval between switches decreases with an increase in Reynolds number.

A study on the vortex pattern evolution at subcritical Reynolds regime for two parallel cylinders within the range of $1.5 < p/D < 2.0$ with emphasis on the switching process was performed by Ng et al., 1997. A discrete-vortex model was used to describe the narrow wake vortex evolution. They concluded that the occurrence of amalgamation and vortex pairing, and dipole are found for the flip-flopping regime, and they associated the transition from the symmetric state to the asymmetric state do the asymmetry of one of the gap vortices.

A review of the wake pattern for various configurations of cylinders was made by Zdravkovich, 1977 and more recently by Sumner, 2010 which reviewed studies about the flow around two circular cylinders in many configurations, for steady cross-flow, focusing on the near-wake flow patterns. Zhou and Alam, 2016 also reviewed the subject of flow around two cylinders. They provided a full picture of the flow in terms of several regimes, physical aspects, flow structures, Strouhal numbers, fluid forces, momentum transport, and the Reynolds number effect.

Alam et al., 2003 studied the aerodynamic characteristics of two side-by-side cylinders for various spacing ratios and Reynolds number of $Re = 5.5 \times 10^4$. They observed that the narrow wake has the higher drag coefficients and the large wake has the smaller drag coefficients. They also associated the narrow wake mode with the higher vortex shedding frequency and the large wake mode with the low vortex shedding frequency.

Gavilán Moreno, 2008 studied the bistable flow that occurred in a recirculation loop from the boiling vessel of a nuclear power station. In the study, the Hilbert transform was the tool of choice for signal analysis since it is suitable for non-linear and non-stationary data. The study concluded that the bistable phenomenon has a two-attractor structure and since the attractors are present in frequency and phase space analysis, the phenomenon is non-linear and non-stationary. They also created a model for this particular case, associating the bistability with a zero-mean uncorrelated Gaussian noise and treating it with the Hilbert transform, and the obtained results showed good statistical agreement with the experimental series.

De Paula, 2013 studied the main parameters that characterize the bistable phenomenon using probability density functions, finite mixture model, deterministic chaos concepts, and symbolic dynamic. The analysis provided using finite mixture models [De Paula and Möller, 2013] showed that the increase in the axial velocity component is accompanied by the increase of the transversal component, and their PDFs present two major states of energy, with two different shapes and distinct Strouhal numbers. The model was efficient to determine the numerical values and shape of PDF modes. De Paula and Möller, 2018 studied the chaotic nature of the bistable phenomenon. The studied results showed the presence of positive Lyapunov exponents evidencing that bistability has a chaotic behavior.

Keogh and Meskell, 2014 studied the bistable flow in parallel triangular tube arrays with $p/D = 1.375$. The authors used Mode-average PIV for the analysis. They concluded that for certain flow velocities, there was a high correlation between the pressure signals of each instrumented cylinder. They also observed that the pressure field distributions showed a skew Gaussian distribution, suggesting that longer time series would be necessary for a more accurate analysis.

Akar et al., 2016 investigated the bistable flow structure past a pair of cylinders side-by-side in shallow waters applying PIV techniques. They identified two distinct vortex shedding frequencies. According to them in the wide wake around the cylinder, small-scale vortices are perceptible, and a large vortex is formed by the convergence of them. Meantime small-scale vortices merging with large vortex compose a larger vortex. The amalgamation of these positive vortexes collapses quickly and finally, this vortex starts to push the jet-like flow in the direction of the other cylinder. They all form a single vortex around the cylinder with the wide wake, and the gap-flow changes its direction and switches from one side to another randomly and momentum transfer is carried by larger vortices from the core flow region into the wake region in each cycle.

Liu and Jaiman, 2018 studied the dynamics of the gap flow and vortex-induced vibration on a side-by-side arrangement using numerical simulation, for Reynolds numbers in the range of $100 \leq Re \leq 800$. The authors applied dynamic mode decomposition (DMD) to characterize the space-time evolution of the primary vortex wake. They found that a saddle point was formed along the interface between imbalanced counter-signed vorticity clusters. Also, around those saddle-point regions, the intensity of the fluid momentum and the fluid shearing were important for the near-wake instability. They concluded that the interaction dynamics between the gap-flow proximity interference and the gap-flow instability enhances the vortex-to-vortex interactions.

Neumeister et al., 2018 found a very similar result with numerical simulations of the flow of side-by-side cylinders, where it was possible to observe that the mode changing was influenced by the interaction of vortex on the two wakes behind the cylinders. They also verified that the asymmetric characteristic of the wake is not observed simultaneously for the whole high of the cylinder, presenting a time delay between occurring in one end of the cylinder and the other.

The influence of the angular position on the bistable phenomenon was studied experimentally and with flow visualizations by Habowski et al., 2020. The authors concluded that the biased gap flow was very sensitive to the position angle of the cylinders. For incidence angle 2.5° the flow attempted some switching, while for angles bigger than 5° the flow remained biased towards one of the cylinders. For angles of incidence of 60° and 75°, the large wake was dominant causing the narrow wake to be displaced downwards and increasing the amplitude of the vertical component of velocity. For this behavior, it is expected an increase in intensity for incidence angles greater than 75°. Vertical disturbances in the wakes were observed in the flow visualizations and may be related to the non-simultaneous occurrence of bistability along the cylinder.

A global analysis on the origin of the phenomenon and about the instability of two side-by-side circular cylinders was presented by Carini et al., 2014. Such studies were conducted numerically for a two-dimensional Navier-Stokes equation and at low Reynolds number, disregarding the three-dimensional features of turbulence. The authors pointed that a connection between the flip-flop behaviour at low and high Reynolds numbers was not established. At low Reynolds numbers, it was attributed to the instability of the in-phase shedding cycle.

Chatterjee and Biswas, 2015 studied numerically the dynamics of the flow around a row of square cylinders in a staggered arrangement. They varied the transversal spacing between the cylinders, *G/d* (where *G* is the transversal space and *d* is the diameter) in 1, 2, 3, and 5. They established low dimensional chaos for the flow at a relatively small transverse spacing of the cylinders. Also, they identified that the transition to chaos was through a quasi-periodic route. The quasi-periodic route was characterized by a set of different tools like power spectra, autocorrelation function, state-space reconstruction, and Poincaré section. The chaos was quantified by the Lyapunov exponent and the fractal dimension.

2.2 Chaos and strange attractors

Experiments and numerical simulations have provided supporting evidence to the mathematical analysis showing that many physical systems may exhibit chaotic behavior without random inputs. Chaos is usually used to distinguish those systems from true random systems [Holmes and Moon, 1983]

Chaotic systems can include mechanical devices with nonlinear springs, nonlinear circuits, convective flows, aeroelastic systems, hydrodynamic systems, and many others. Hydrodynamic systems can behave in many ways, some can exhibit steady-state flow patterns, others oscillate in a regular periodic way Lorenz, 1963, and some, like bistability, may oscillate in a non-periodic, irregular, and chaotic manner when observed in a long period. These chaotic motions have been called strange attractors to distinguish them from the limit cycle and periodic motion.

Chaotic motions are also related to classic bifurcation theory in dynamic systems, being one of its features the succession of bifurcations to increasingly higher subharmonics as a parameter is varied [Holmes and Moon, 1983]. Landau suggested that an infinite sequence of bifurcations could be a route to turbulence, but it was Ruelle and Takens, 1971 that first suggested that strange attractors could arise after a finite sequence of bifurcations and might provide a model for turbulent motion [Holmes and Moon, 1983].

> *"An important element in the explanation of the chaotic* behavior *of solutions of deterministic equations of motion is the sensitive dependence of solutions on initial conditions. In fact, sensitive dependence on the initial condition, in the form of the notion of ergodicity, has long played a central role in one of the standard justifications for the foundations of that subject. (...) For dissipative systems, what usually happens is that most of the points of the instantaneous state space are transient in the sense that the orbits that start there eventually go to and stay in another part of the state space. A simple instance is provided by the stable dynamic equilibrium that is usually set up when a dissipative system is driven gently. In this situation, all orbits, no matter where in the state space they start, converge eventually to a single stationary solution corresponding to laminar motion. In a certain sense, the system has no effective degrees of freedom, although the state space may have large or even infinite dimension. There are one, or possibly a few-invariant sets of relatively low dimensions in the state space to which almost all orbits converge. These sets are what are called attractors. (...) attractors, except for the very simplest ones, are typically not smooth surfaces in the state space but rather more complicated kinds of sets* [Lanford, 1982]*."*

The simplest types of behavior of a physical system are either stationary or periodic states. A stationary state corresponds, by definition, to $dx/dt = 0$ and is represented in the phase space by a fixed point of the differential system. A fixed point coincides with a singular point of the vector field X given by $X(x) = 0$. Periodic behavior is represented in the phase space by a closed orbit. In general, it is more difficult to determine periodic orbits than fixed points. The fixed points and limit circles represent asymptotic behaviors of the system: they are typical examples of attractors of dissipative systems and are represented in Figure 2.1. The ensemble of initial conditions from which the system evolves toward a given attractor is called the basin of attraction of the attractor. In two-dimensional phase space, it can be shown that the only possible attractors are fixed points and periodic orbits. In higher dimensions other attractors can exist, for example, tori representing periodic or quasi-periodic behavior with several frequencies, or strange attractors representing chaotic behavior. A strange attractor is characterized by its fractal structure and by the fact that the trajectories coming from two neighboring points diverge exponentially (while remaining on the attractor). This latter phenomenon is very important and is referred to as sensitivity to, or exponential dependence on, the initial conditions [Charru, 2011].

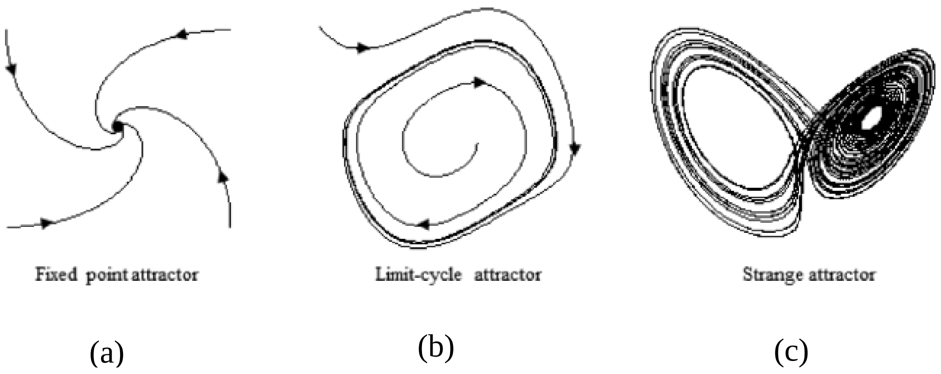

Figure 2.1 – Examples of a) a fixed point attractor, b) a limit-cycle attractor and c) a strange attractor. Adapted from Richardson et al.,2014.

Given a specific differential equation, the flow is the time evolution of the collection of solutions corresponding to all possible initial conditions for which solutions exist. If there is a limit set to which all solutions in the flow become arbitrarily close after a sufficiently long time, this set is called an attractor of the flow. Moreover, if the solutions remain arbitrarily close to the attractor for all subsequent times, the attractor is said to be stable. An important property of strange attractors is that they do not have integral dimension [McDonough et al., 1984].

According to Ruelle, 1995, a strange attractor consists of an infinity of points in the plane or in m-dimensional space. These points correspond to the states of a chaotic system. In Lorenz, 1963 study, where a flow was represented in a three-dimensional space, existed a bounded region into which every trajectory became trapped eventually. Therefore, all trajectories tend to a set of measure zero, called attractor. In some cases, the attractor is simply a point (stable equilibrium point) or a closed curve (limit cycle). But in other cases, the attractor has a much more complex structure being called a strange attractor. Attractors are highly sensitive to initial conditions, [Hénon, 2004].

For Grassberger and Procaccia, 2004 a strange attractor arises when the flow does not contract a volume element in all directions, but, stretches in some. Therefore, to remain confined into the bounded domain, the volume element gets folded at the same time, creating after some time a multi-sheeted structure.

Swinney and Gollub, 1986 suggested that certain fluid systems generate chaotic motion and can be described by introducing a state or phase space. The coordinates of the phase space can be the projections of the motion of the system onto the various modes into which it can be decomposed. For dissipative systems, the trajectories in phase space converge to a limit set known as attractor. For non-periodic states of deterministic systems, which are called chaotic, their representation is called strange attractor and has a complex topology. Typically, a strange attractor is an infinitely folded sheet of infinite extent located in a bounded region of phase space. The rates at which the trajectories diverge or converge in various locally defined orthogonal directions are called Lyapunov exponents and at least one of these must be positive for a chaotic flow.

Lorenz, 1963 defined a phase space as an M-dimension Euclidian space Γ whose coordinates are $X_1, \dots, X_M$. Each point in phase space represents a possible instantaneous state of the system. A system governed by the set of equations

$$ {}^{dX_i}/_{dt} = F_i(X_i, \dots, X_M), \;\; i = 1, \dots, M, \tag{1} $$

is represented by a moving particle in phase space, traveling along a trajectory in phase space. The phase space concept has been useful in treating finite systems and treatment of differential equations. Also, the set of phase space trajectories for all possible initial conditions forms a phase portrait of the system [Roux et al., 1983, Charru, 2011].

Lorenz, 1963 studied a simple deterministic non-periodic flow, designed to represent a forced dissipative hydrodynamical system. His interest was in the nature of the nonperiodic solutions of the system of equations

$$ \begin{cases} X = -\sigma x + \sigma y \\ Y = -xz + rx - y \\ Z = xy - bz \end{cases} \tag{2} $$

here x, y, and z are variables, and σ, r, and b are parameters of the equation. In those equations x is proportional to the intensity of the convective motion, y is proportional to the temperature difference between ascending and descending currents, and z is proportional to the distortion of the vertical temperature profile from linearity. Those equations are known as the Lorenz attractor, which occurs for the parameters $\sigma = 10$, $r = 28$, and $b = 8/3$.

Ruelle and Takens, 1971 were some of the first authors to propose a mechanism for the generation of turbulence associated with the theory of strange attractors. They studied the physical phenomenon of turbulent fluid motion for a dissipative system and suggested that strange attractors could arise after a finite sequence of bifurcations and might provide a model for turbulent motion. They hypothesized that a fluid flow in any particular experiment can be described by a typical (low) finite-dimensional, deterministic system of differential equations.

Takens, 1981 reviewed the concepts presented previously in Ruelle and Takens, 1971 and presented a procedure to decide if experimental data could be attributed to the presence of strange attractors. The procedures were applied to the Taylor-Couette experiment and compared with the theory presented by Landau and Lifshitz, 1987 concerning rotating cylinders.

Strange attractor models are based upon systems of nonlinear Ordinary Differential Equations (ODE). Those systems present two essential features: a finite number of degrees of freedom and they are deterministic. Concerned with the fact that neither bifurcation theory nor experiments observing the routs to chaos were clear of whether the fluid flow continued to be described by a system with few degrees of freedom beyond the onset of chaos, Guckenheimer, 1986 proposed a way to test the Ruelle-Takens theories and alternative models for situations where the strange attractor models were inappropriate. The study concluded that it was possible to estimate the variance in a random perturbation of a strange attractor, even though this study did not test the method in experimental data.

Zou et al., 1985 computed numerically the statistical characteristic quantities and the marginal probability distribution of the Lorenz attractor. Considering that the Lorenz system of equations is deterministic, the chaotic behavior of the attractor is due to its ergodic motion. Based on that some statistical quantities were related to the parameter ρ. For this analysis, it was assumed that the initial value X_0 was indeterministic, but obeyed a deterministic probability distribution $P(X_0, t_0)$. They computed the main statistical quantities like expected value, standard deviation, and marginal probability distribution. The results showed that even though the Lorenz system and its solutions are deterministic, the motion on the strange attractor is ergodic and random overall. They also concluded that the motion on the strange attractor is chaotic, but its statistical characteristics are stable, and it has a deterministic statistical structure that does not depend on the initial conditions.

De Paula and Möller, 2018 studied the chaotic behavior of the bistable flow for two cylinders side-by-side and tube banks. They calculated the largest Lyapunov exponents for the filtered signals and concluded that: for the two side-by-side circular cylinders the largest Lyapunov exponent was 1.6778 ± 0.1362, for the two rows tube bank the larges Lyapunov was 1.4034 ± 0.3273. They also demonstrated that the filtered signal presented a Lyapunov exponent 9.5 times greater than the original signal, showing that the dissociation of the bistable phenomenon from turbulence increases the value of the largest Lyapunov exponent.

Analysing the previous references, it is possible to identify a lack of studies concerning the bistable phenomenon dynamics and characteristics, especially with the application of actual non-linear, non-stationary tools. In De Paula and Möller, 2018 the focus was on stablishing if the bistability was chaotic or not, and the main point was to identify the better method and parameters for reconstructing the strange attractor properly. This present study uses those values as a reference, and different from the previous bistability-chaos study, the focus is on identifying the physical parameters that influenced on the bistable dynamics and chaotic characteristics, and eventually provide a way for reconstructing the general dynamics of bistable flows without the need of a differential equation.

2.3 Hilbert Huang Transform in turbulence

Attempting to overcome the problems involved in the analysis of non-stationary and non-linear data, Huang et al., 1998 developed a new method, after called the Hilbert-Huang transform (HHT). The method is constituted by two parts, being the key part, the empirical mode decomposition (EMD), and the second part a Hilbert spectral analysis (HSA). The method allowed a final representation of the results in an energy-frequency-time distribution, designated as the Hilbert spectrum. Since the method was decomposed using the data as base, it provided a meaningful instantaneous frequency. Even though it was a good method some mathematical problems still needed to be solved in order to make it more robust.

Huang et al., 1999 summarized the method on fluid mechanics examples of nonlinear waves, Stokes waves, and turbulence. They observed that the method provided a better precision on particular events in time-frequency than wavelet analysis, and those results also had a more physically meaningful interpretation of the underlying dynamic processes. Wavelet analysis gives a uniform frequency resolution, but, the time resolution is also uniformly poor. In comparison, the Hilbert spectrum gives a much sharper resolution in frequency and a more precise location in time.

Huang et al., 2003 established a confidence limit for the HHT method and a stable range of stopping criteria for the decomposition sifting phase (EMD). This approach has made the results of the final processing with HSA, and the entire EMD/HSA method more definitive.

The Hilbert-Huang transform proved to be a promising tool for non-linear and non-stationary data, being applied in many areas of research, for example, the analysis of financial time series [Huang et al., 2003], molecular dynamics [Phillips et al., 2003], structural damage detection [Yang et al., 2004; Roveri and Carcaterra, 2012], vibration signal analysis [Peng et al., 2005; Feldman, 2011], biological data analysis for cardiac and neurological problems detection [Xie and Wang, 2006; Huang, Z. et al., 2007; Lo et al., 2009; Yang et al., 2010; Duman et al., 2012; Tsai et al., 2012; Sikkandar et al., 2013; Huang et al., 2014; Tsai et al., 2016], seismic and geophysics [Battista et al., 2007; Huang and Wu, 2008; Yinfeng et al., 2008], nuclear power plants [Gavilán Moreno, 2008] and many others. This work is going to summarize those studies concerning any form of turbulence.

Veltcheva and Soares, 2004 studied the application of Hilbert Huang transform to identify the components of ocean waves. They applied the EMD method as well as a confident limit for each EMD in the sifting process. They concluded that the specific peculiarities of each wave were well captured by the EMD and reproduced by the Intrinsic Mode Functions (IMF), the energy contents of the wave were clearly traced by the Hilbert spectrum. Veltcheva and Soares, 2007 applied the method to analyze abnormal waves in the wave records from the North Sea. They concluded that the Hilbert spectrum detected the appearance of abnormal waves both in time and frequency domains. They verified that the instantaneous frequency increased considerably during a single abnormal wave occurrence, while the Hilbert spectrum of the abnormal wave group had very distinguished peaks. They also concluded that the asymmetry of abnormal waves is correlated with the magnitude of intra-wave frequency modulation.

Dätig and Schlurmann, 2004 presented a general overview of the Hilbert Huang method; first, they used simple trigonometric functions to get an idea about the performance of the EMD on linear harmonic signals in general. They also applied the HHT on computed nonlinear irregular water waves and measured irregular water waves recorded in a laboratory wave flume. They concluded that the method has an excellent correspondence between the simulated and recorded wave, also the spectral representations showed the instantaneous frequencies and amplitudes strongly correlated with the water surface elevations on both numerical and measured series.

Li et al., 2005 proposed a new filtering method for data with intermittency problems present in the empirical mode decomposition. They pre-treated the data using wavelet transform then proceed with empirical mode decomposition. As a result, mode mixing is eliminated, and the resulting IMF components bear genuine physics sense. The choice of the most appropriate wavelet is fundamental for the correct analysis of the studied signal.

Pesce et al., 2006 used Hilbert-Huang transform on the analysis of Vortex-Induced Vibration (VIV), which is a highly non-linear phenomenon. The aim was to characterize some hidden dynamics characteristics, like time-modulation, jumps of multi-branched response, and their related energy spectra. They concluded that the results for HHT have a better definition than those treated by wavelets. They pointed out the need for further investigation on the meaning of the IMF and their Hilbert spectra to construct a more complete and physical interpretation of the phenomena involved in VIV.

Flow-induced vibrations, due to their high occurrence, are a serious problem, especially when associated with cooling systems or heat exchangers in the process industry and nuclear facilities. These vibrations cause a decrease in cooling capacity leading to fatigue and damage to pipes, [Kim and Alam, 2015]. Païdoussis et al., 2010 report several studies on instabilities induced by vortices in pairs of cylinders or small groups of cylinders. They also report studies on vortex-induced vibrations in bundles of tubes submitted to cross-flow. Several different behaviors were observed, which depend on the space ratio between the cylinders of the tube bundles.

Huang et al., 2007 applied EMD and HHT in experimental homogeneous turbulence time series and concluded that the filtering characteristic of the method in the inertial range could have interesting applications in turbulence modelling. They also estimated the scaling properties and the Hilbert spectrum of the turbulent series. On their further work also in homogeneous turbulence analysis, they associated each IMF mode to dissipation, inertial range, and integral scales, and then they generalized the approach to characterize the scaling intermittency of turbulence in the inertial range in an amplitude-frequency space. They also obtained a 2D amplitude-frequency representation of the PDF of turbulent fluctuations with scaling trend, and that a log-Poisson distribution fits better the velocity amplitude PDF than a lognormal distribution, Huang et al., 2008.

Miau et al., 2007 used Hilbert and Wavelet transformations to analyze the signals of MEMS sensors situated span wisely on a circular cylinder for examining the unsteady, three-dimensional behavior of vortex shedding. The analysis allowed the identification of the strong three-dimensional vortex shedding process due to the occurrences of vortex dislocation. This was also demonstrated in further work, where hot wires and MEMS sensors were applied Miau et al., 2009.

Vincent et al., 2010 applied the Hilbert-Huang transform to describe the time-evolving variability in wind speed time series from a wind farm on the west coast of Denmark. They concluded that the two-dimensional Hilbert spectrum gave a good representation of the scales of motion present in wind speed. They could identify the presence of coherent periodicities in the time series.

Foucher and Ravier, 2010, studied stationary and non-stationary grid-generated turbulence using empirical mode decomposition and triple-decomposition. The non-stationary conditions were generated by superimposing periodic and random fluctuations on the original data. First, they applied the empirical mode decomposition to filter and separate the turbulent velocity components from those fluctuations then triple-decomposition was used to determine turbulent intensity, the integral length scales, and the power spectral density of the velocity. They compared the properties of the turbulence with and without the addition of the fluctuations and found good agreement.

Mazellier and Foucher, 2011 evaluated the performances of the HHT method on a fully developed turbulent velocity signal on which they introduced a numerical perturbation mimicking a long-period flapping. They introduced a criterion of “resemblance” for distinguishing between the polluted and non-polluted modes extracted from the perturbed velocity signal using EMD. They found a good agreement between the recovered and the reference signal. They compared turbulence characteristics using spectra and the structure functions.

Silveira and Möller, 2012 compared Fourier, Wavelets and Hilbert-Huang transform for the analysis of the shedding process in the turbulent wake of a circular cylinder. Their results were still preliminary, but they concluded that the Hilbert-Huang transform was more effective than wavelets in the identification of the vortex shedding frequency and its harmonics.

Horszczaruk and Möller, 2013 analyzed the bistable phenomenon of the turbulent flow on two circular cylinders side-by-side using Hilbert-Huang transform. Two pitch-to-diameter ratios were used in the study, *p/D* = 1.26 and 1.60. They compared the results found using HSA with those of wavelet transform. They concluded in a preliminary way that the HSA provided better visualization of the main frequencies of the phenomenon, but they could not find a relation between the Hilbert spectrum and the wavelet spectrogram.

Huang et al., 2014 proposed to use an arbitrary order Hilbert spectral analysis to estimate the two-scale correlation of a turbulent velocity database obtained from an experimental homogeneous and nearly isotropic turbulent channel flow. They used an active-grid technique to achieve a high Reynolds number. They found a logarithmic law in the inertial and dissipation ranges; moreover, the Hilbert analysis satisfies a lognormal distribution. They observed the power-law behavior of the maximum PDF of the Hilbert energy in the logarithmic frame with a scaling exponent of 0.33. They concluded that the Hilbert analysis was applicable to check the relation between two scales, in the energy sense or other statistical quantities.

Medina et al., 2015 proposed a study approach to better understand the relationship between wind output and power output in a wind turbine in Denmark using empirical mode decomposition and time-dependent intrinsic correlation methods. They also characterized the wind turbulence using scaling power spectra and tried to identify the intermittency using the Hilbert spectral analysis. They concluded that some characteristics of the power spectrum could be caused by the turbine configurations. They were able to observe a zero-correlation progression in the time-dependent intrinsic correlation.

Zhu et al., 2016 used empirical mode decomposition to study scale properties of turbulent transport and coherent structures based on velocity and temperature time series of atmosphere stably stratified turbulence. The velocity and temperature data were produced through numerical simulation using LES. They concluded that EMD was a good method to decompose turbulence signals, allowing the separation in different modes and the contribution of each scale. They found out that intermittency is intensified by the stratification in small scales, and that there are different time scales of coherent structure in different modes between the stream-wise and vertical velocities. The vertical scalar transport showed the presence of the counter-gradient transport (CGT) phenomena at certain modes, while gradient transport occurred in other modes.

3 METHODOLOGY

3.1 Experimental technique

The aerodynamic channel used in the experiments, Figure 3.1 has a rectangular test section of 0.146 m height, 0.193 m width, and 1.02 m length, made of acrylic. The air flow is driven by a centrifugal blower of 0.64 kW and passes through a diffuser, two honeycombs, and two screens, that homogenize the flow and reduce the turbulence intensity to about 0.6% in the test section. Before the test section, a Pitot tube is placed at a fixed position at 180 mm from the screens, to measure the steady reference velocity of the experiments. Placed beside the Pitot tube is a temperature sensor. Downstream the test section, outside the aerodynamic channel, a tri-dimensional positioning system is assembled; it allows the millimeter alignment of the probe support. Blower speed is controlled by a frequency inverter allowing the flow velocity in the aerodynamic channel to be varied from zero to 16 m/s.

The velocity and its fluctuations are measured using a DANTEC StreamLine constant hot-wire anemometry system, with a hot wire probe (type DANTEC 55P11), with a single wire perpendicular to the main flow. Data acquisition was performed with a 16-bit A/D board (NATIONAL INSTRUMENTS 9215-A), with a USB interface. Measurements were performed at constant velocity. The error of the determination of the velocity fluctuations with hot wire is between 1 and 4 %.

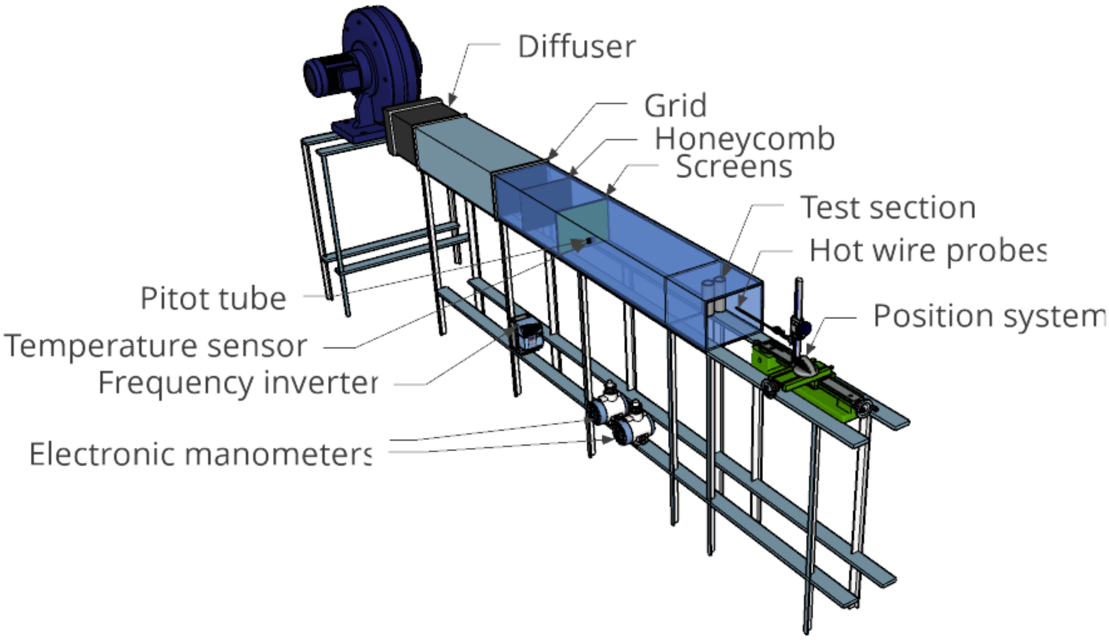

Figure 3.1 – Schematic view of the aerodynamic channel.

The cylinders diameter used in the experiment was D = 25.1 mm, and the cylinders were placed side-by-side with p/D = 1.16, 1.26, and 1.60, where p is the distance between centers of the cylinders. Reynolds numbers were calculated based on the cylinder diameter and the free stream velocity and varied from 7.22×10^3 to 2.32×10^4. Uncertainties associated with the mean velocity values are about ± 3%, and for the instantaneous velocity values, about ± 5%.

The two cylinders side-by-side were positioned at 180 mm from the end of the channel. Two hot wire probes (type DANTEC 55P11) with a single wire perpendicular to the main flow were positioned at a downstream distance "*x*" from the center of the cylinders, of 10 mm, according to the scheme in Fig. 3.2. Data were acquired at a sampling frequency of 1000 Hz, and a low pass filter at 300 Hz. For the data analyses, once the data is symmetric, only the signal corresponding to probe 1 was considered,.

Hilbert-Huang transform, Fourier, wavelets transform, statistical and the dynamic analysis were performed in a script using the Matlab® software.

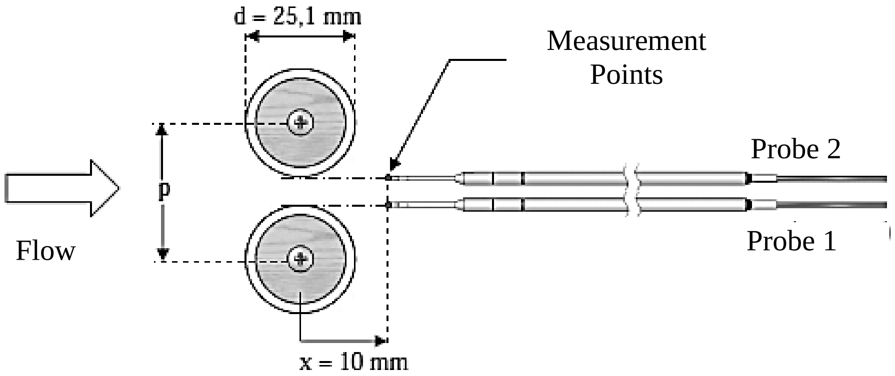

Figure 3.2 - Two cylinders side-by-side geometry and probe positioning at x = 10 mm from cylinder center.

3.2 Time-frequency domains

The time-domain analysis consists in calculating the four moments of the probability density function: mean values, standard deviation, skewness, and kurtosis. For the determination of how the fluctuations of one parameter are related over time, one can use the autocorrelation function, according to Tennekes and Lumley, 1972.

The analysis in the frequency domain, also known as spectral analysis, is essentially made using the Fourier transform through the power spectral density function (PSD). According to Bendat and Piersol, 2010 this function allows highlighting the main characteristics of the signals, consisting in the Fourier spectra of a time series, smoothed by intervals of frequency, or bandwidth and in a set of estimates, or window. Further details on spectral analysis can be found on Möller and Silvestrini, 2004; De Paula, 2013; Indrusiak, 2004; Flandrin, 1999b among others.

For a better interpretation of the Fourier spectra, the frequency domain can be converted in dimensionless wavenumber, which can be defined as

$$k^* = \frac{2\pi F}{\langle u \rangle} D \tag{3}$$

where F is the frequency vector and $\langle u \rangle$ is the mean velocity of the signal. The spectrum function can be converted in a dimensionless energy spectrum function described as

$$\Phi^*(k^*) = \Phi(k) \frac{\langle u \rangle}{2\pi U^2 D} . \tag{4}$$

The wavelet transform, as already mentioned, arises from the idea of stretching and compressing the window of the windowed Fourier transform, to better fit the frequencies to be localized, hence allowing the definition of the scales in time and frequency domains. Since the wavelet basis is localized simultaneously in time and frequency domains, this characteristic provides a uniform resolution in frequency, but also a uniformly poor resolution in time. This balance in frequency and time resolution is explained by Heisenberg's uncertainty principle. Further description of the mathematical approach of the wavelet transform can be found in Daubechies, 1992; Farge, 1992, Indrusiak, 2004; Indrusiak et al., 2016 among others.

3.3 Chaos on experimental data

3.3.1 General Dimensions

The so-called dimension of a strange attractor is actually a topological dimension and there are many methods to calculate it.

Strange attractors are typically characterized by fractal dimensionality D_F which is smaller than the number of degrees of freedom F, $D_F < F$. This fractal dimension (or Hausdorff dimension) has been the most common measure of the strangeness of the attractor [Grassberger and Procaccia, 1983].

The fractal dimension is usually understood as the classical box-counting. The box-counting dimension is more interesting for practical applications, whereas the Hausdorff dimension is more interesting for analytical properties since its definition is based on a measure [Fernández-Martínez and Sánchez-Granero, 2014, Fernández-Martínez and Sánchez-Granero, 2015].

In order to define it, first, the attractor is covered by F-dimensional hypercubes of side length L and considers the limit $L \to 0$. If the minimum number of cubes needed to cover the attractor grows like

$$M(L)_{L\to\overset{\simeq}{0}}\ L^{-D_F} \tag{5}$$

the exponent D_F is called the Hausdorff dimension of the attractor [Grassberger and Procaccia, 2004, Guckenheimer, 1982].

The definition of the capacity dimension and many attempts to calculate it are given by various authors such as Takens, 1981, Ott, 1981, and Greenside et al., 1982. The algorithm that is used to compute this dimension is also known as the box-counting algorithm.

The capacity of an attracting set M, which is assumed to be contained in an invariant manifold of some dynamical system, is defined as:

$$C = \lim_{\epsilon\to 0} \ln N_{\epsilon} / \ln \frac{1}{\epsilon} \tag{6}$$

where $N\epsilon$ is the minimum number of boxes of side ϵ in phase space needed to cover the set M. This law is verified by computing $N\epsilon$ for an appropriate scaling region and then plotting, -log($N\epsilon$) against log(ϵ). Using linear regression is possible to see that this law is satisfied, and the capacity C is then given by the slope of the fitted line.

For low-dimensional sets ($C \leq 2$) the method works, and a reasonable number of points is enough to determine de capacity of the dimensional vector. Turns out that the use of a single time series of any observable to extract this measure has been found to be impractical for dynamic systems which possess attractors whose $C > 2$. A more profound explanation of the limitations of the method can be found in Greenside et al., 1982 and Grassberger and Procaccia, 1983.

Grassberger and Procaccia, 2004 proposed an algorithm to extract the correlation exponent, v from the time series of a single variable. They also showed that v correlates with the Lyapunov exponents and with de dimension D_F.

Considering a long time series on the attractor, where N is the number of points, denoted by:

$$\{\vec{X}_i\}_{i=\frac{N}{1}} \equiv \{\vec{X}(t+i\tau)\}_{i=\frac{N}{1}} \tag{7}$$

where τ is an arbitrary but fixed increment. The correlation integral is defined by:

$$C(r) \equiv \lim_{N\to\infty} \frac{1}{N^2} \sum_{i,j=1}^{N} \theta(r - |\vec{X}_i - \vec{X}_j|) \equiv \int_0^r d^d r' c(\vec{r}') \tag{8}$$

where $\theta(x)$ is the Heaviside function and $c(\overrightarrow{r'})$ is the standard correlation function. for small r is assumed that $C(r)$ behaves as a power of r

$$C(r) \propto r^{Dc} \tag{9}$$

D_c is also called correlation dimension and it is related with the capacity dimension and with a properly defined entropy:

$$S(l) = S_0 - \sigma \ln l \tag{10}$$

where $S(l)$ the general entropy, and σ is called the information dimension, via the set of inequalities:

$$Dc \leq \sigma \leq C\ . \tag{11}$$

The correlation integral is sensitive to the distribution of points in the attractor Grassberger and Procaccia, 1983, embedding dimension, reconstruction delay and is unreliable except for long, noise-free time series [Rosenstein et al., 1993, Eckmann and Ruelle, 1992].

Kaplan and Yorke, 1979 proposed a dimension based on the Lyapunov exponents of the system. Ranking the Lyapunov exponents for larges λ_1 to the smallest λ_d. Let j be the largest integer such that $\lambda_1 + \lambda_2 + \ldots + \lambda_j > 0$, the Kaplan-Yorke dimension can be defined as

$$D_{KY} = j + \frac{\sum_{i=1}^{j} \lambda_i}{-\lambda_{j+1}}. \tag{12}$$

For the two-dimensional mapping, the box-counting dimension C equals the Kaplan-Yorke dimension D_{KY}.

3.3.2 Rosenstein Method for the Largest Lyapunov

Assuming a one-dimensional time series, and assuming that these data is originated from a dynamic system of higher dimensions, e.g. the Lorenz system, the first step in the analysis involves the reconstruction of the attractor dynamics. This reconstruction can be made using the differential equations (in case they are known), or using a time lag for the known variable, creating a vector from which the required coordinates will be provided. The method of delays presented by Packard et al., 1980 was tested by Takens, 1981, and later, improved by Sauer et al., 1991 and was the method of choice in this study.

Consider a scalar function representing the measurements denoted by:

$$s(t) = s(t_0 + n\Delta t), \tag{13}$$

the idea consists of using the lagged variables, $s(t+T) = s(t_0 + (n+T)\Delta t)$ to form a coordinate system to capture the structure in the state space, where T is a time delay or reconstruction step. The coordinates of the reconstructed state space can then be provided by using a correlation of time lags to create a vector in D dimensions in the form

$$h(t) = [s(t), s(t+T), s(t+2T), \ldots, s(t+(D-1)T)]. \tag{14}$$

Take as an example, this process applied in the Lorenz attractor which consists of a system with 3 coordinates [$x(t)$, $y(t)$, $z(t)$]. Selecting the $x(t)$ variable and using a vector of time-delayed with 3 variables in R^3, [$x(t)$, $x(t + T)$, $x(t + 2T)$]. The observed geometry of the original attractor and the reconstructed one are similar, even though distorted. This distortion does not matter for the analysis since the topological properties of the reconstructed system are preserved. The reconstructed 2D and 3D state space for the Lorenz attractor, for the parameters $\sigma = 10$, $r = 28$, and $b = 8/3$, are represented in Fig. 3.3.

To obtain sufficiently accurate results the choice of the time delay requires some care. If the chosen time delay is too large the coordinates $s(t + T)$ and $s(t + 2T)$ will be totally independent of each other statistically speaking, and the reconstructed attractor will be covering the whole state space. On the other hand, if the chosen time lag is too small, the coordinates will be hard to distinguish since their numerical values are very close ($x = y$) creating a linear dependency between the delayed values that does not happen in the original attractor. This linear dependency compresses the reconstructed attractor around the diagonal of the state space, [Takens,1981].

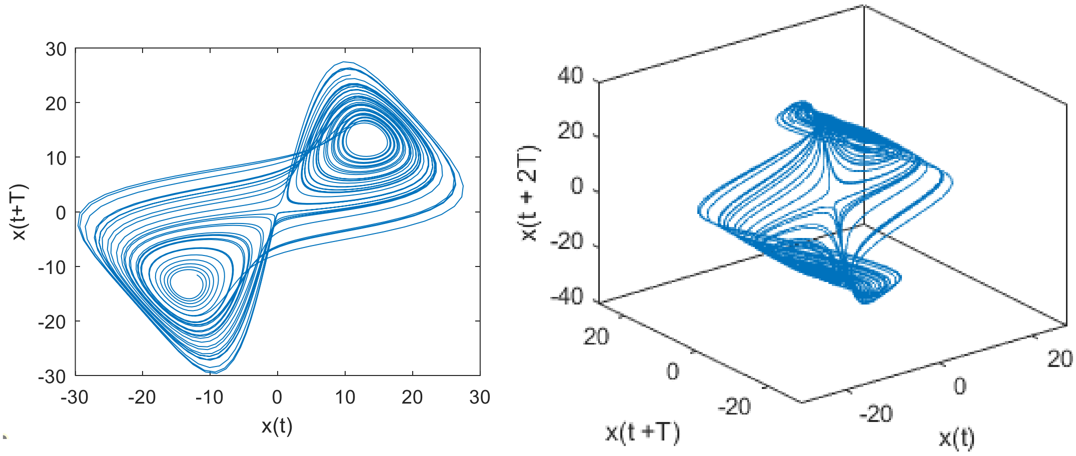

(a) (b)

Figure 3.3 – a) representation of the state space for a 2D Lorenz attractor and b) reconstructed state space for the 2D Lorenz attractor, with $T = 10$.

Wolf et al., 1985 suggested that the choice of the time delay is mostly arbitrary. Other methods to solve the issue have been applied like the use of average mutual information

(AMI) [Fraser and Swinney, 1986, Wallot and Mønster, 2018] and correlation integral [Liebert and Schuster, 1989, Franca and Savi, 2001, Bolea et al., 2014]. In this work the time lag was chosen arbitrarily as it was in De Paula and Möller, 2018, taking care that the reconstructed state space was not too compressed in the diagonal nor completely uncorrelated.

Choosing a sufficiently large dimension D for the reconstruction is called embedding, and the selected dimension, embedding dimension De. Therefore, any dimension that follows $D \geq De$ could be an embedding. In this work, the method of the false nearest neighbors is applied to determine the minimum size necessary to embed an attractor, [Kennel et al., 1992].

The method consists of counting the number of false nearest neighbors for each point of the attractor. The attractor will be considered sufficiently unfolded when the number of false nearest neighbors reduces to zero, and the smaller embedding dimension able to represent it appropriately can be identified.

To identify a false neighbor one can take k as a given point and $k(1)$ as another point in the reconstructed attractor with dimension D. Consider also $(R_D)^2(k)$ as the square distance between them. So $k(1)$ would be a false neighbor if

$$\{[R_D + 1)^2(k) - (R_D)^2(k)]/(R_D)^2(k)\}^{1/2} > R_T \tag{15}$$

where R_T is a critical distance. For $k(1)$ to be a false neighbor $(R_D)^2(k)$ will probably increase when going from dimension D to D+1. In the case of experimental data, due to the finite number of points used, for $k(1)$ to be a false neighbor, it has to satisfy the two following conditions:

1) Considering R_A a typical size of the attractor, then $R_D \sim R_A$ and $R_{D+1}(k) \sim 2R_A$ for a false neighbor.
2) Establishing a critical limit A_c, so that $[(R_{D+1})(k)/R_A > A_c$.

As mentioned by De Paula and Möller, 2018 the dimension of an attractor associated with experimental data is usually unknown a priori, and some analyses are required to evaluate and interpret the values obtained. Depending on the strange attractor features, a reconstructed space smaller than R^D may be sufficient to reveal its structure. For practical considerations, this parameter is very important, since computational cost rises exponentially with *D*, and calculations for higher dimensions can be contaminated by the noise present in small dimensional data, [Abarbanel et al., 1993].

The next step is to evaluate the Largest Lyapunov exponent (λ_1). The Lyapunov exponent can be interpreted as a rate at which the system loses predictability. Also, according to Wolf et al., 1985, Lyapunov exponents can be interpreted as the average exponential rates of divergence of the nearby orbits in state space, and the system would be defined as chaotic if at least one of the exponents is positive. This work uses an algorithm based on Rosenstein's method proposed by Rosenstein et al., 1993. The approach consists of expressing the reconstructing trajectory *X*, as a matrix where each row is a phase space vector

$$X = (X_1, X_2, \dots, X_M)' \tag{16}$$

where X_i is the state of the system at a discrete time *i*. For a time series with *N*-points $(x_1, x_2, \dots, x_N)$ each *Xi* is given by

$$X_i = (x_i, x_{i+\tau}, \dots, x_{i+(D_e-1)\tau}) \tag{17}$$

where τ is the time lag and *De* is the embedding dimension. Therefore, *X* is an *M* × *De* matrix and the constants *De*, *M*, *N*, and τ are related as

$$M = N - (D_e - 1)\tau. \tag{18}$$

A more detailed explanation of Rosenstein's algorithm can be found in Rosenstein et al., 1993 and De Paula and Möller, 2018.

The largest Lyapunov exponent is then estimated as the average separation of nearest neighbors

$$\lambda_1(i) = \frac{1}{i\Delta t(M-i)} \sum_{j=1}^{M-1} \ln \frac{d_j(i)}{d_j(0)} \tag{19}$$

where Δt is the sampling period of the time series, $d_j(i)$ is the distance between the j^{th} pair of nearest neighbors after a discrete-time step *i* or $i\Delta t$ seconds, and *M* is the number of reconstructed points.

The largest Lyapunov exponent can also be defined mathematically by

$$d(t) = C\exp(\lambda_1(t)) \tag{20}$$

where $d(t)$ is the average divergence in the time t, and C is the constant that minimizes the initial separation. It is assumed from the determination of λ_1 that, the j^{th} nearest pair of nearest neighbors diverge about the given rate

$$d_j(i) \approx C_j e^{\lambda_1(i\,\Delta t)}. \tag{21}$$

where C_j is the initial separation. The largest Lyapunov exponent is easily calculated using the least-squares fit to the average line defined by

$$y(i) = \frac{1}{\Delta \mathrm{t}}\langle \ln d_j(i) \rangle. \tag{22}$$

where $\langle\,\rangle$ denotes the average over all values of j. This process of obtaining the average value of the differences is, according to Rosenstein et al., 1993 key to obtaining an accurate value of λ_1 when using experimental data and in the presence of noise.

3.4 Hilbert-Huang transform

Hilbert-Huang transform is a viable method for non-linear and non-stationary data analysis. It consists of two parts: the empirical mode decomposition (EMD) and the Hilbert Spectral Analysis (HSA). Huang et al., 1998 proposed that one of the typical characteristics of nonlinear processes is the intra-wave frequency modulation, which indicates that the instantaneous frequency changes within one oscillation cycle. Quoting Huang et al., 1998:

> *There are actually, two types of frequency modulations: the interwave and the intrawave modulations. The first type is familiar to us; the frequency of the oscillation is gradually changing with the waves in a dispersive system. Technically, in the dispersive waves, the frequency is also changing within one wave, but that was not emphasized either for convenience or for lack of a more precise frequency definition. The second type is less familiar, but it is also a common phenomenon: if the frequency changes from time to time within a wave its profile can no longer be a simple sine or*

cosine function. Therefore, any wave-profile deformation from the simple sinusoidal form implies the intrawave frequency modulation. In the past, such phenomena were treated as harmonic distortions.

3.4.1 Hilbert transform

The instantaneous frequency of a signal can be computed through the Hilbert transform. The Hilbert transform, *Y*(t) of an arbitrary time series, *X*(t), is obtained by

$$Y(t) = \frac{1}{\pi} P \int_{-\infty}^{\infty} \frac{X(t')}{t - t'} dt' \tag{23}$$

where, *P* indicates the Cauchy principal value of the singular integral (further information in the Cauchy principal value [Legua and Sánchez-Ruiz, 2017]. Essentially Eq. 23, is a convolution of *X*(t) with 1/*t*; hence, the transform emphasizes the local properties of *X*(t). By definition *X*(t) and *Y*(t) form a complex conjugate pair, so it is possible to have an analytical signal, *Z*(t) described as

$$Z(t) = X(t) + iY(t) = a(t)e^{i\theta(t)} \tag{24}$$

in which

$$a(t) = [X^2(t) + Y^2(t)]^{1/2} \tag{25}$$

$$\theta(t) = \arctan\left(\frac{Y(t)}{X(t)}\right) \tag{26}$$

where $a(t)$ is the instantaneous amplitude, and $\theta(t)$ is the phase function. Based on the Hilbert transform, the instantaneous frequency can be defined as:

$$\omega(t) = \frac{d\theta(t)}{dt}. \tag{27}$$

At any given time, it is possible that the signal may involve more than one oscillation mode, and consequently, the signal has more than one local instantaneous frequency at a time [Huang and Shen, 2005].

3.4.2 Empirical mode decomposition

The empirical mode decomposition (EMD) is a necessary method to deal with nonstationary and nonlinear data. It is an intuitive, direct, and adaptive method, with an *a posteriori*-defined basis from the decomposition method, based on and derived from the data [Huang and Shen, 2005].

The decomposition is based on the following assumptions [Huang et al., 1998]:

4. The signal has at least two extrema, a maximum, and a minimum;
5. The characteristic time scale is defined by the time lapse between the extrema;
6. If the data were devoid of extrema but contained only inflection points, it can be differentiated once or more times to reveal the extrema.

The method identifies the intrinsic oscillatory modes by their characteristic time scales in the data empirically and then decomposes the data accordingly. Each of these oscillatory modes is represented by an Intrinsic Mode Function (IMF). The IMF is a class of functions so that the instantaneous frequency can be defined everywhere based on the local properties of the data. An IMF is defined as a function that satisfies the two following conditions:

a. The number of extrema and the number of zero crossings must either equal or differ at most by one in the whole data set,
b. The mean value of the envelope defined by the local maxima and the envelope defined by the local minima is zero everywhere.

Instead of constant amplitude and frequency, like a simple harmonic component, the IMF can have a variable amplitude and frequency as functions of time. A systematic way to extract the IMF's is described by Huang et al., 1998, designated as sifting process, starts by identifying all the extrema (maxima and minima) of the signal. Figure 3.4 represents data used as an example for a demonstration of the sifting method. These maxima and minima are connected with cubic spline lines to construct an upper envelope, and the same procedure is made for the minima. The upper and lower envelopes should cover the whole data. Their mean is designated as m_1 and the difference between the data and m_1 is the first component, h_1, Figure 3.5 and Figure 3.6 exemplify the process.

$$h_1 = X(t) - m_1. \tag{28}$$

If h_1 does not satisfy the definition of an IMF, the sifting procedure can be repeated k times, until h_{1k} is an IMF, exemplified in Figure 3.7.

$$h_{1k} = h_{1(k-1)} - m_{1k}. \tag{29}$$

Then it is designated as the first IMF component from the data, Figure 3.8 exemplifies the first IMF, c_1, of example the data

$$c_1 = h_{1k}. \tag{30}$$

The sifting process serves two purposes, which are: to eliminate riding waves and to make the wave profiles more symmetric. The first component c_1 should contain the finest scale or the shortest period component of the signal. If follows that c_1 can be separated from the rest of the data by

$$r_1 = X(t) - c_1. \tag{31}$$

Since the residue r_1 still contains information of longer period components, it is treated as the new data and the same sifting process is repeated as described above in all the subsequent r_j's resulting

$$r_1 - c_2 = r_2, \ldots, r_{n-1} - c_n = r_n. \tag{32}$$

The sifting process can be stopped either when the component c_n or the residue r_n becomes too small that it is less than the predetermined value of substantial consequence, or when the residue r_n becomes a monotonic function from which no more IMF's can be extracted. By summing Eq.31 and Eq.32, we obtain the data written in terms of IMF components plus the residue or trend

$$X(t) = \sum_{i=1}^{n} c_i + r_n. \tag{33}$$

Because of the dyadic filter bank characteristic of the EMD, for an N data length, the finite number of steps in decomposition satisfies the relation below [Flandrin et al., 2004]

$$n \le \log_2 N. \tag{34}$$

The components of the EMD are usually physically meaningful, for the characteristic scales are defined by physical data. Nevertheless, there are cases when a certain scale of a phenomenon is intermittent, in this case, the decomposed component could contain two scales on one IMF component. Therefore, the physical meaning of the decomposition comes only in the totality of the decomposed components in the Hilbert spectrum [Huang et al., 1998].

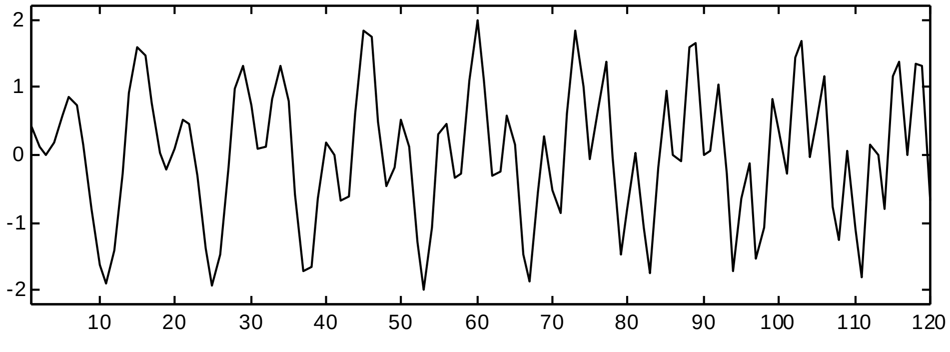

Figure 3.4 – Data used as an example of the EMD procedure. Adapted from [Flandrin, 2019].

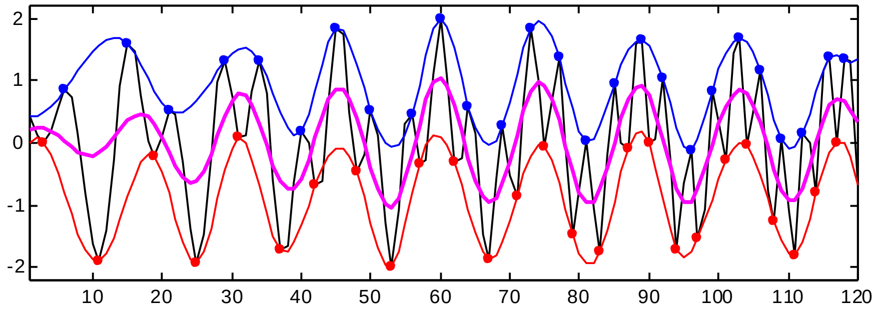

Figure 3.5 – The data and the upper and lower envelopes (blue and red, respectively), defined by the local maxima and minima, and the mean value of the upper and lower envelopes, m_1, in magenta. Adapted from [Flandrin, 2019].

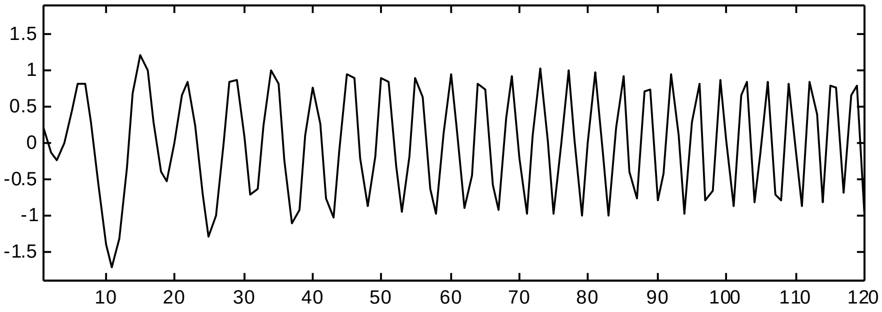

Figure 3.6 – The component h_1 after the first sifting iteration. Adapted from [Flandrin, 2019].

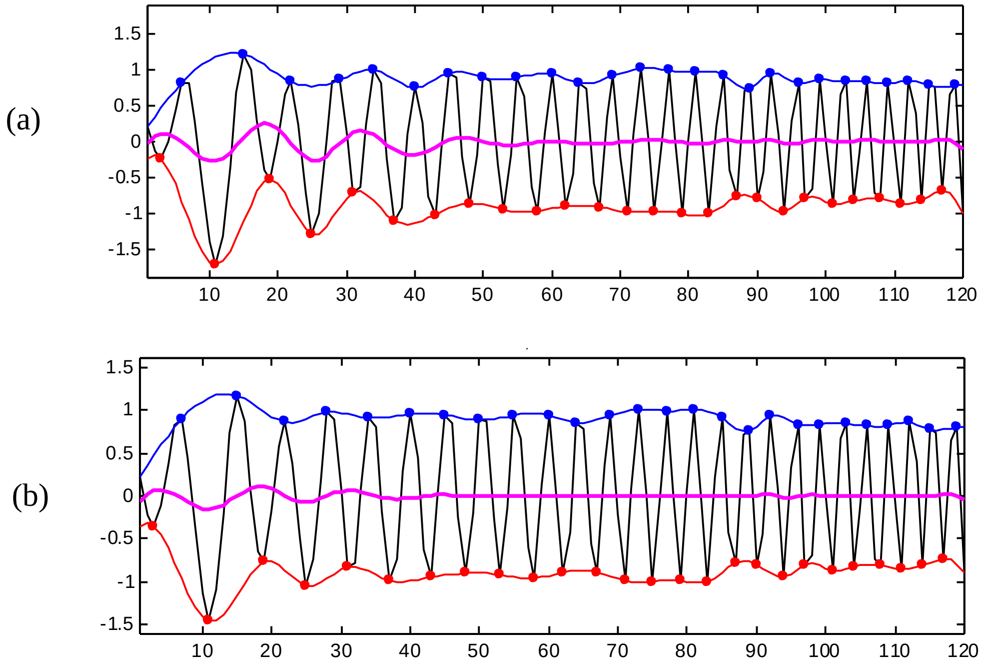

Figure 3.7 – Repeating the sifting steps (a) with h_{12} and (b) with h_{13}. Adapted from [Flandrin, 2019].

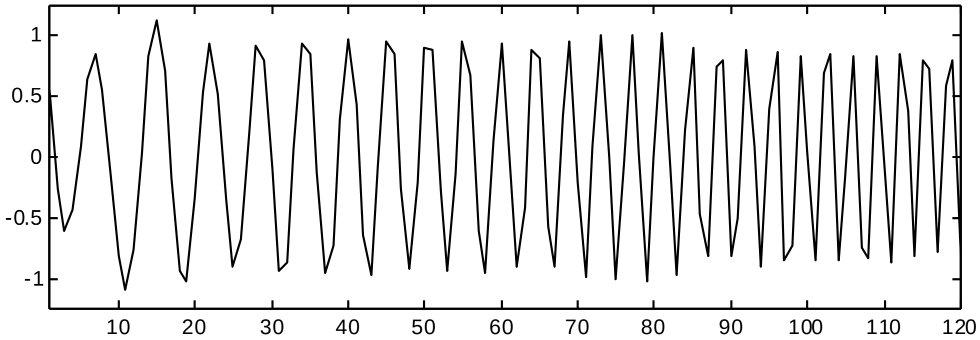

Figure 3.8 – The first IMF component c_1 after 8 steps. Adapted from [Flandrin, 2019].

3.4.3 Ensemble empirical mode decomposition

The intermittency present in some IMF components causes the appearance of the so-called mode mixing, which is when a single IMF consists of signals of widely disparate scales, or when a signal has similar scales residing in different IMF components (Wu and Huang, 2009).

To successfully deal with the scale separation problem, a noise-assisted data analysis method was proposed, called the Ensemble Empirical Mode Decomposition (EEMD). The approach is based on the studies of the statistical properties of the white noise (Wu and Huang, 2004), which showed that the EMD is effectively an adaptive dyadic filter bank when applied to white noise.

The concept of the EEMD is based on the following observations [Wu and Huang, 2009]:

1) A collection of white noise cancels each other out in time-space ensemble mean, surviving and persisting, only the final noise-added signal ensemble mean.
2) Finite amplitude white noise is necessary to force the ensemble to exhaust all possible solutions; the finite magnitude noise makes the different scale signals reside in the corresponding IMF, dictated by the dyadic filter banks.
3) The true physically meaningful answer to the EMD is not the one without noise, it is designated to be the ensemble mean of a large number of trials consisting of the noise-added signal.

The EEMD algorithm is developed as follows:

a) Add a white noise series to the data;
b) Decompose the noise-added data into IMFs
c) Repeat steps 1 and 2 N number of trials, with different white noise series each time;
d) Obtain the ensemble mean of corresponding IMFs of the decompositions.

The noise-added signal is treated as the possible random noise that would be encountered in the measured data. In those conditions, the observed data with the added noise is

$$X_i(t) = X(t) + w_i(t) \tag{35}$$

where $X_i(t)$ is the i^{th} observation of noise added data, $X(t)$ is the observed data set, $w_i(t)$ is the i^{th} realization of the white noise series. As the ensemble number approaches infinity, the final IMF, c_j can be defined as

$$c_j = \lim_{N\to\infty} \frac{1}{N} \sum_{i=1}^{N} \left[c_{ji}(t) + r_{ki}(t) \right] \tag{36}$$

in which $c_{ji}(t)$ is the j^{th} IMF component of the i^{th} realization of noise-added data, and $r_{ki}(t)$ is the residue after k number of IMFs are extracted in each sifting process. The ensemble number of trials, N, has to be large, for the ensemble mean to cancel out the added noise. A flowchart of the EEMD steps is presented in Figure 3.9.

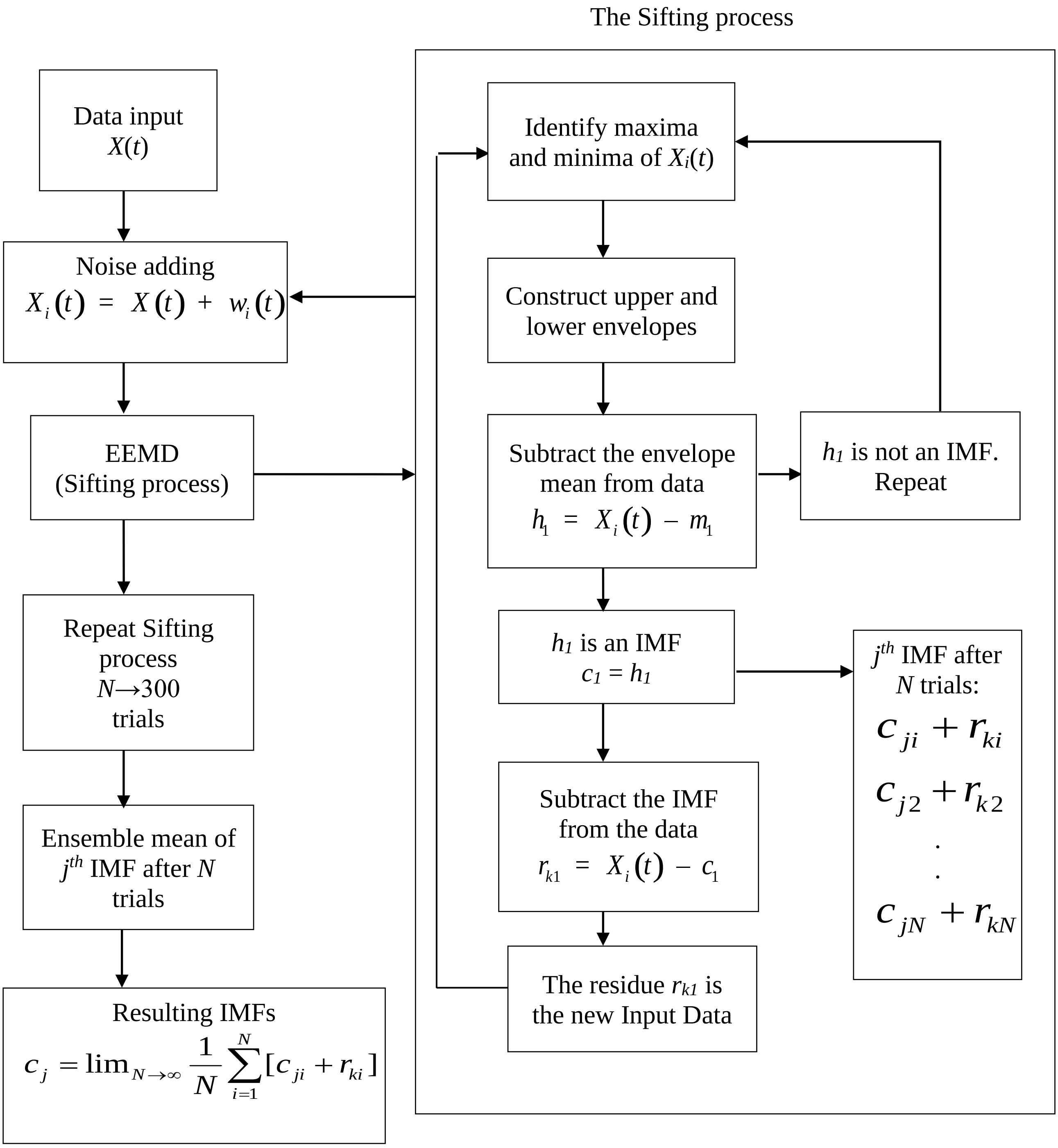

Figure 3.9 – Flowchart of EEMD steps.

3.4.4 Hilbert spectral analysis

After obtaining the intrinsic mode functions, one can apply the Hilbert transform to each IMF component and compute the instantaneous frequency using Eq. 23 to 27. The original data, after the Hilbert transform, can be expressed as the IMF real part $\Re$.

$$X_H(t) = \Re\left\{\sum_{j=1}^{n} a_j(t)\exp[i\int \omega_j(t)dt]\right\}. \tag{37}$$

With the IMF expansion, the amplitude and the frequency modulations are also clearly separated. This frequency-time distribution of the amplitude is designated as the Hilbert spectrum $H\ (\omega,t)$. Although the Hilbert transform can treat the monotonic trend as part of a longer oscillation, the energy involved in the residual trend representing a mean offset could be overpowering [Huang, 2014].

With the Hilbert Spectrum $H(\omega,t)$ defined, we can also define the marginal spectrum, $h(\omega)$

$$h(\omega) = \int_0^T H(\omega,t)dt. \tag{38}$$

The marginal spectrum offers a measure of the total energy contribution of each frequency value. It represents the accumulated amplitude over the entire data span in a probabilistic sense.

3.4.5 Normalized Hilbert transform

Although the Hilbert transform exists for any function of L^p class (see Titchmarsh, 1948), the phase function of the transformed function will not always yield meaningful instantaneous frequency results. The decomposition of the data into IMFs satisfies only the necessary condition to obtain meaningful instantaneous frequencies, two more theorems add some limitations to the Hilbert transform.

The Bedrosian theorem [Hahn, 1996; Bedrosian, 1963] says that: the Hilbert transform of the product of two signals with no overlapping spectra equals the product of the low-pass term by the Hilbert transform of the high-pass term. Meaning that only the high-frequency term is transformed.

Considering two functions $f(t)$ and $g(t)$, where $f(t)$ is the low-pass term and $g(t)$ is the high-pass term, by the Bedrosian theorem, the Hilbert transform of the product $f(t)g(t)$, can be written as:

$$H[f(t)g(t)] = f(t)H[g(t)]. \tag{39}$$

If the instantaneous frequency, defined in Eq. 27, is to be computed from the phase function, the data can be expressed in the IMF form as

$$x(t) = a(t)\cos[\theta(t)]; \tag{40}$$

then the Hilbert transform gives the conjugated part as

$$H\{a(t)\cos[\theta(t)]\} = a(t)H\{\cos[\theta(t)]\}. \tag{41}$$

This relation can only be true if the amplitude is varying so slowly that the frequency spectra of the envelope and the carrier waves are disjoint. To satisfy this requirement a normalization of the IMFs was proposed, in Huang, 2005; and Huang et al., 2009. The steps for the normalization are:

1) Find all the maxima of the IMFs
2) Define the envelope by a spline through all the maxima, the envelope is designated as $E(t)$.
3) Normalize the IMF by dividing it by $E(t)$ as

$$C_f(t) = \frac{x(t)}{E(t)} \tag{42}$$

where $C_f(t)$ should be the carrier function with all the local maxima equal to unit.

This construction was supposed to yield always unitary amplitudes, however at points where the amplitude fluctuation is large or at locations of fast changing amplitudes, the envelope spline line, passing through the maxima can go below some data points, and this causes the normalized data to have amplitudes higher than unity occasionally.

Another limitation comes from the Nuttall theorem [Nuttall and Bedrosian, 1966]. This theorem questions the condition under which one can write

$$H\{\cos\theta(t)\} = \sin\theta(t) \tag{43}$$

for an arbitrary function of $\theta(t)$. It states that the Hilbert transform of a cosine is not necessarily a simple 90° phase shift, resulting in a sine function with the same arbitrary phase function.

Nuttall first established that for any given function of the form of Eq. 40, for arbitrary $a(t)$ and $\theta(t)$, and if the Hilbert transform of $x(t)$ is given by $xh(t)$, and the quadrature of $x(t)$ is $xq(t)$, defines as

$$xq(t) = a(t)\sin\theta(t) \tag{44}$$

then, the error-index, ΔE, is

$$\Delta E = \int_0^T [xh(t) - xq(t)]^2\, dt = \int_{-\infty}^{\omega_0} F_q(\omega)\, d\omega \tag{45}$$

where

$$F_q(\omega) = F(\omega) + i\int_{-\infty}^{\infty} a(t)\sin\theta(t) e^{-i\omega t}\, dt \tag{46}$$

in which $F(\omega)$ is the Fourier spectrum of the signal, and $F_q(\omega)$ is the spectrum of the quadrature function. This is, however, not a practical result: first, it is expressed in terms of the Fourier spectrum of the quadrature, of a still unknown quadrature; second, the result is given as an overall integral, which provides a constant global measure of the error. For non-stationary time series, this error will not reveal the location of the error on time. And finally, the error index is energy-based, it only states that the $xh(t)$ and $xq(t)$ are different, but do not offer an error index on the frequency, [Huang et al., 2009].

With the normalization Huang, 2005 proposed a variable error. It is based on the principle that if the Hilbert transform indeed produces the quadrature, then the modulus of the analytical signal, defined in Eq. 24, from the empirical envelope should be unity. Any deviation of the modulus of *Z*(*t*) from unity is the error; thus, it is an energy-based indicator of the difference between the quadrature and the Hilbert transform, which can be defined simply as

$$\Delta E(t) = [abs(Z(t)) - 1]^2. \tag{47}$$

This error indicator is a function of time and it gives a local measure of the error incurred in the amplitude. Two factors can contribute to the errors, the first is that the normalization process is not clean, so the normalized amplitude could exceed the unitary value, and the error would not be zero. The second factor arises from the phase function, where the phase plan will not be a perfect circle, resulting in amplitudes different from unity. Huang, 2005 and Huang et al., 2009 conducted detailed comparisons and found the result for the normalization satisfactory.

3.5 Statistical Analysis

The statistical analysis is based on calculating the statistical moments which consist of, mean value, variance, skewness, and kurtosis. Skewness and kurtosis were normalized by the variance, and the variance was normalized by the local mean. The analyzed data consists of eight seconds time series extracted from the original (65,536 points) longer data set, for *p/D* = 1.16, 1.26 and 1.60 and various Reynolds numbers. Each data set of 8.192 seconds was selected in a way that the bistable characteristics of the signal were clearly identified.

For better performance of the algorithm, a time vector was created, corresponding to 0.000 to 8.192 seconds. So, for example, for *p/D* = 1.16, the chosen data fragment was extracted in the time interval of 25.000 to 33.192 seconds of the original velocity signal, but in the graphics, the time vector of the fragment is represented as 0.000 to 8.192 seconds. This procedure is schematically represented in Figure 3.10.

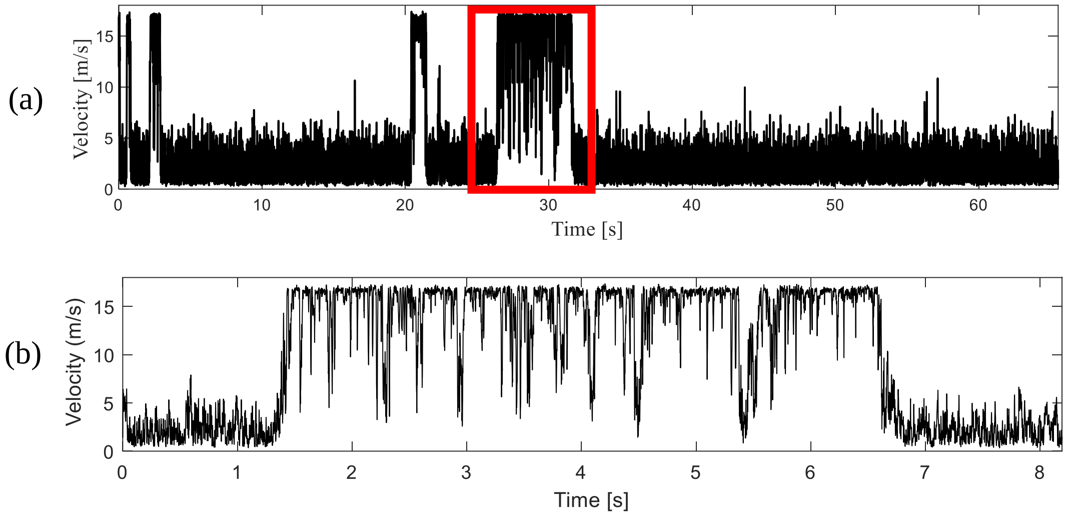

Figure 3.10 – a) Original velocity time series with a fragment of 8.192 seconds indicated by the red box, and b) Fragment extracted from the marked area, with time vector from 0.000 to 8.192 seconds. p/D = 1.16 and Re = 1.44x10^4.

The fragments of the signal were processed for the statistical analysis as follows. First, the signal was scanned by a window of 256 points, with an overlapping of 64 points, creating blocks of signal, in total there were 125 dyadic blocks. This window can be adjusted according to need, size of the signal, and other specific characteristics.

Each block was then converted into a probability density function (PDF), generating 125 PDFs, each PDF with 100 bins. Those PDFs can be associated with a probability function, like a *t*-Student or a skew-normal distribution for example. The first four statistical moments of each PDF block were then calculated. The variations between the maximum, minimum and mean value of each statistical moment with Reynolds number and p/D were presented. Through this analysis, it is possible to associate each wake mode to its statistical characteristics and find patterns of behavior that may repeat for different bistable data sets.

Figure 3.11 illustrates this process for three different situations, first with the window of 256 points in the large wake (Figure 3.11.a), the corresponding PDF is presented in Figure 3.11.d). In the second situation, the window comprehends part of the large wake and part of the narrow wake (Figure 3.11.b), the corresponding PDF is shown in Figure 3.11.e). And at last, with the window in the narrow wake (Figure 3.11.c) and its corresponding PDF in Figure 3.11.f).

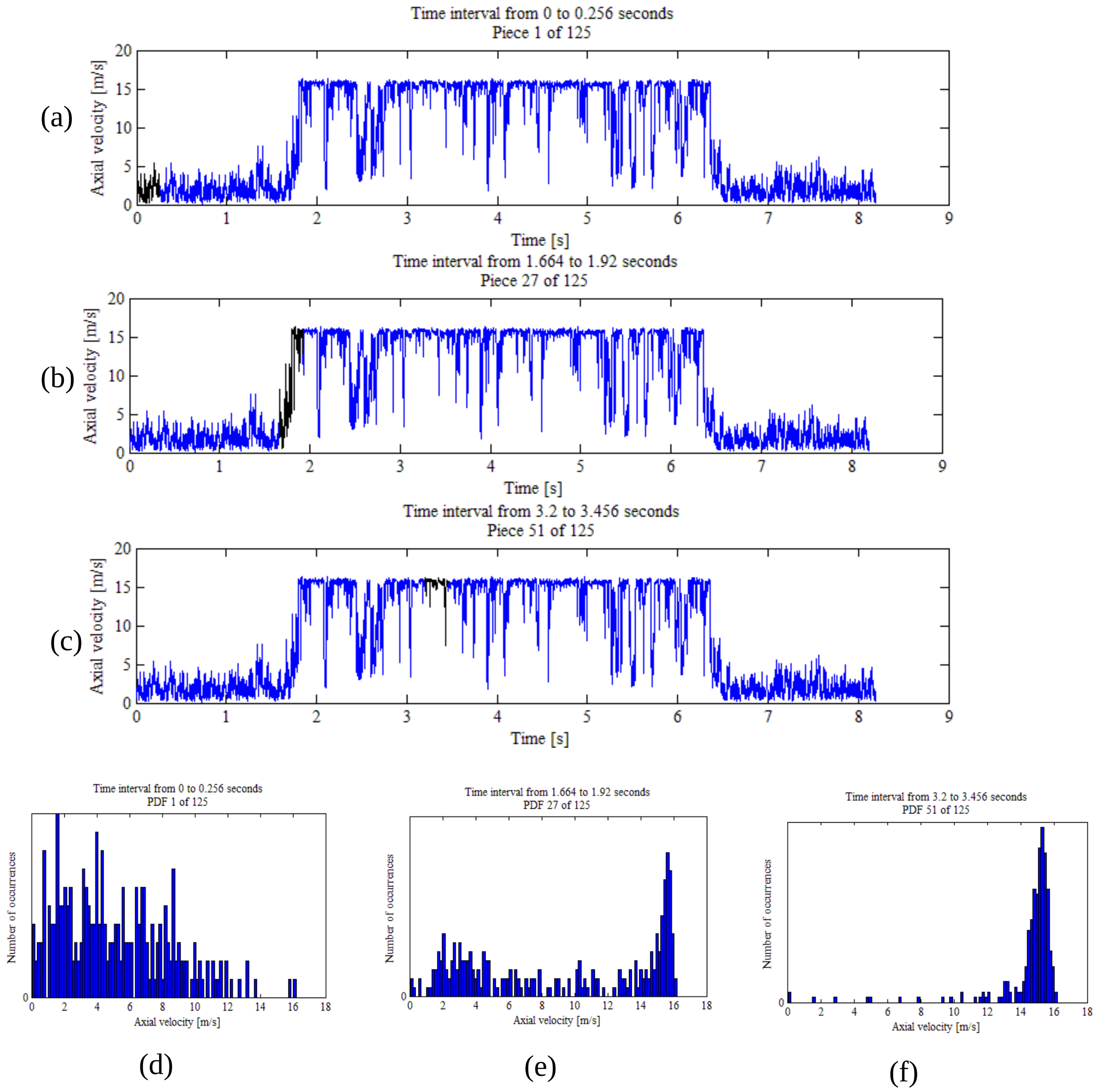

Figure 3.11 - Schematic representation of the velocity time series (in blue) and the blocks of 256 points (in black), and the corresponding PDFs for those blocks. a) large wake, b) the two modes simultaneously, c) narrow wake, d) PDF corresponding to the large wake, e) PDF corresponding to the two wakes simultaneously and f) PDF corresponding to the narrow wake.

4 RESULTS

In this chapter, the results of velocity measurements using hot-wire anemometry, for two cylinders side-by-side, in turbulent flow in aerodynamic channel will be presented. The study was realized for cylinders with D = 25.1 mm with Reynolds numbers, from $Re = 7.22\text{x}10^3$ to $2.32\text{x}10^4$, the pitch-to-diameter ratios of choice were p/D = 1.16, 1.26, and 1.60.

The results are separated into three subchapters, according to the different methods and analysis applied. Subchapter 4.1 brings the results about the Hilbert-Huang transform applied to the bistable phenomenon. Subchapter 4.2 shows the results of the statistical analysis of bistable time series. And subchapter 4.3 shows the results from the dynamic analysis using chaos theory.

4.1 Hilbert Spectral Analysis

The results on the application of the Hilbert-Huang transform methodology are presented in this section. The method was applied to velocity time series for two cylinders side-by-side with D = 25.1 mm, with p/D = 1.16. 1.26, and 1.60, submitted to a turbulent flow, $Re = 1.44\times10^4$. The bistable phenomenon is identified by the two levels of velocity, small values for a large wake, high-velocity values for the narrow wake.

The EEMD method was performed in the bistable time series as described in Figure 3.9 generating a set of 16 IMF components and a residue; the velocity signal and the IMFs are shown in Fig. 4.1. for p/D = 1.16 and Figure 4.2 for p/D = 1.26. It is possible to observe that the first three IMF components present characteristics that resemble noise, also their content can be associated with the turbulent part of the signals. From components C4 to C8 it is possible to observe an increase in the amplitude of fluctuations in the regions where the mode changes from the large wake to the narrow wake. The bistable oscillatory behavior becomes more evident in the following IMF components; as the fluctuations around zero, corresponding to the large wake, reduce in amplitude; the fluctuations corresponding to the narrow wake increase in amplitude. The observations of the IMFs indicate that the bistable phenomenon is predominantly a low frequency phenomenon.

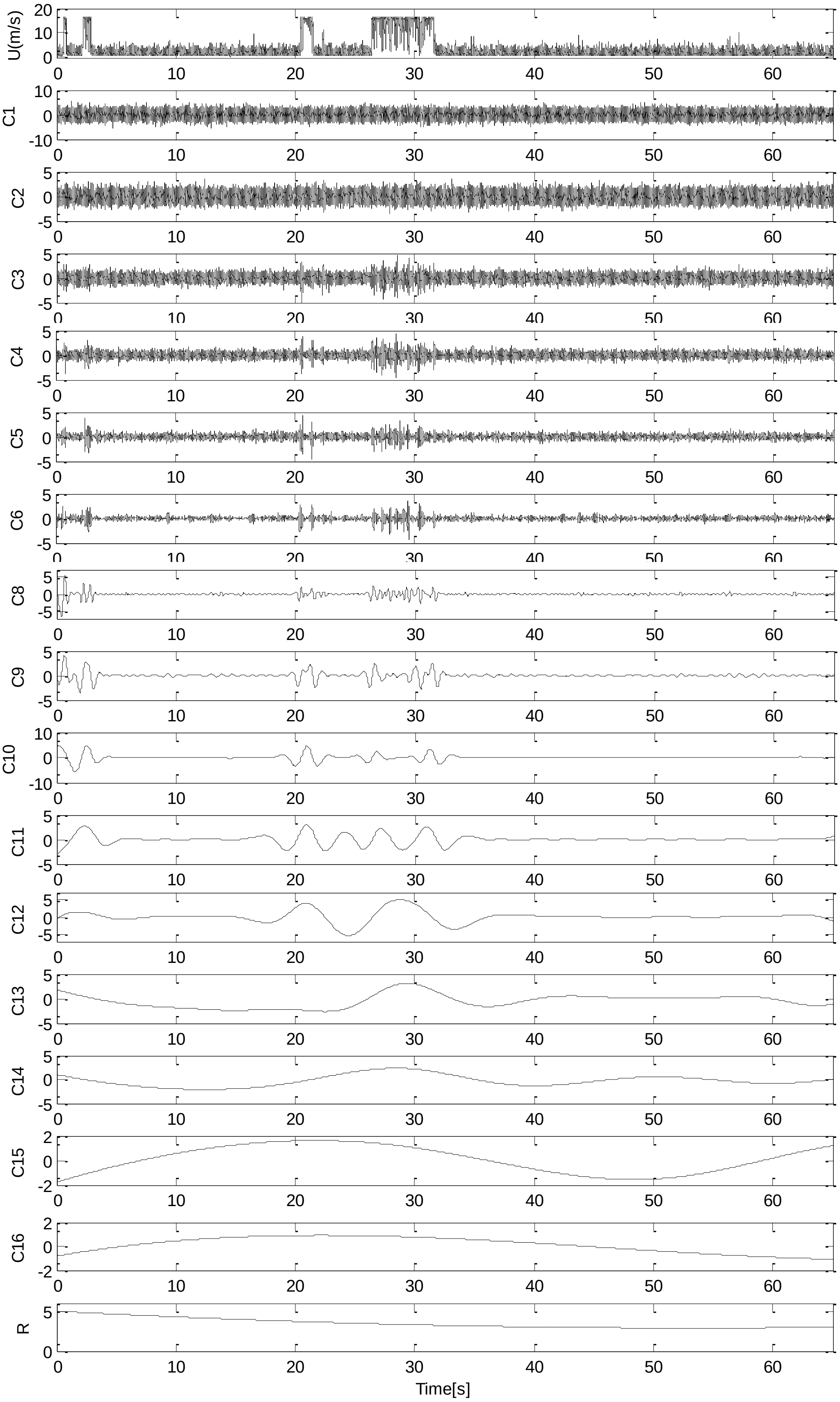

Figure 4.1 – Intrinsic Mode Functions and residue for *D* = 25.1 mm, *p/D* = 1.16, *Re* = 1.44×10^4.

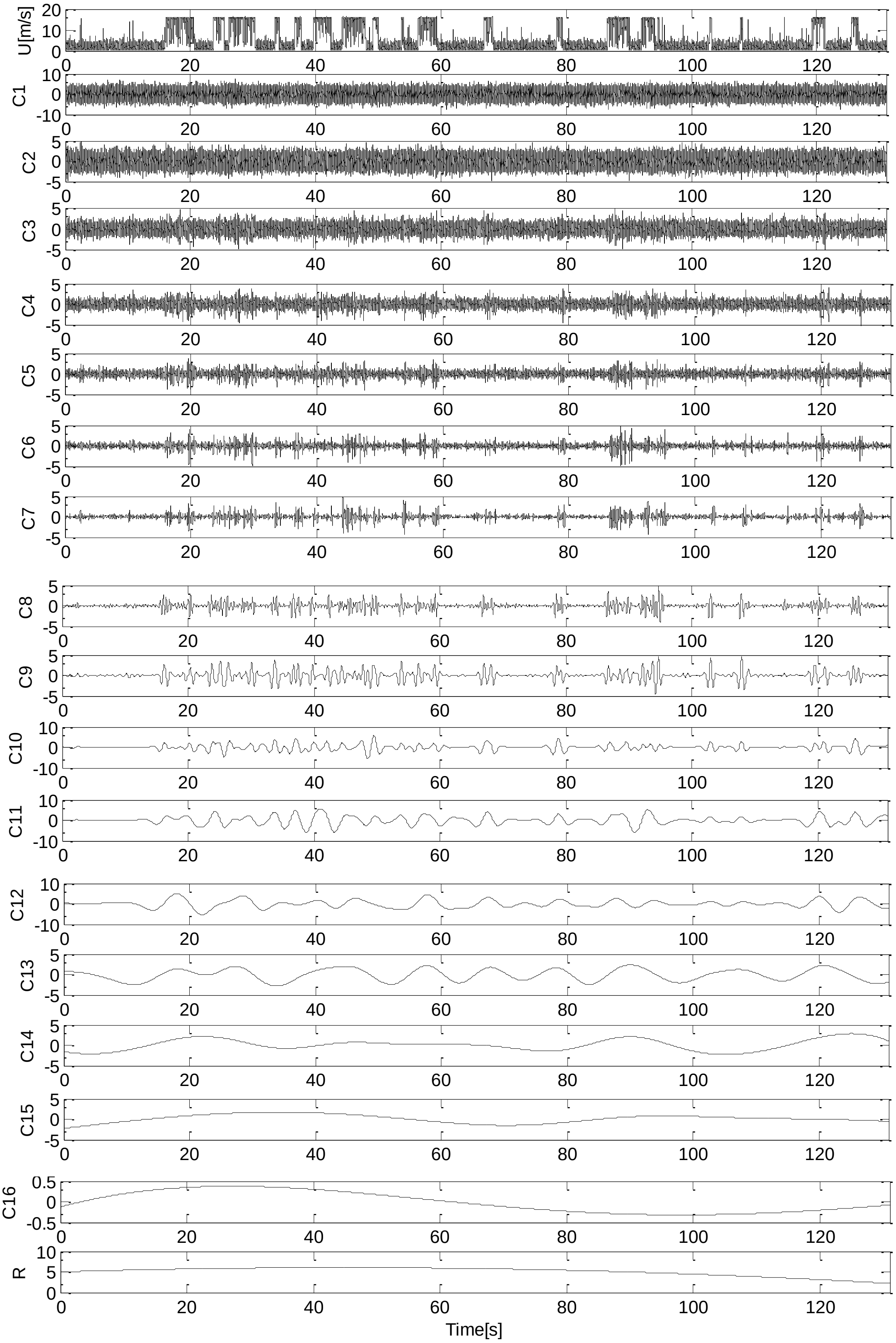

Figure 4.2 – Intrinsic Mode Functions and residue for *D* = 25.1 mm, *p/D* = 1.26, *Re* = 1.44×10^4.

Looking at the power spectra of the IMF components, in Figure 4.3 it is possible to observe that component C1, which corresponds to the highest frequencies, does not fit properly with the spectrum of the velocity signal, C2 and C3 present the same behavior. This is probably a consequence of the presence of noise in those components, the turbulent part of the signal, and can be associated with the fact that the bistable phenomenon happens in two different frequencies simultaneously, wide wake and narrow wake, causing the EEMD to compensate the energy in the small-scale components.

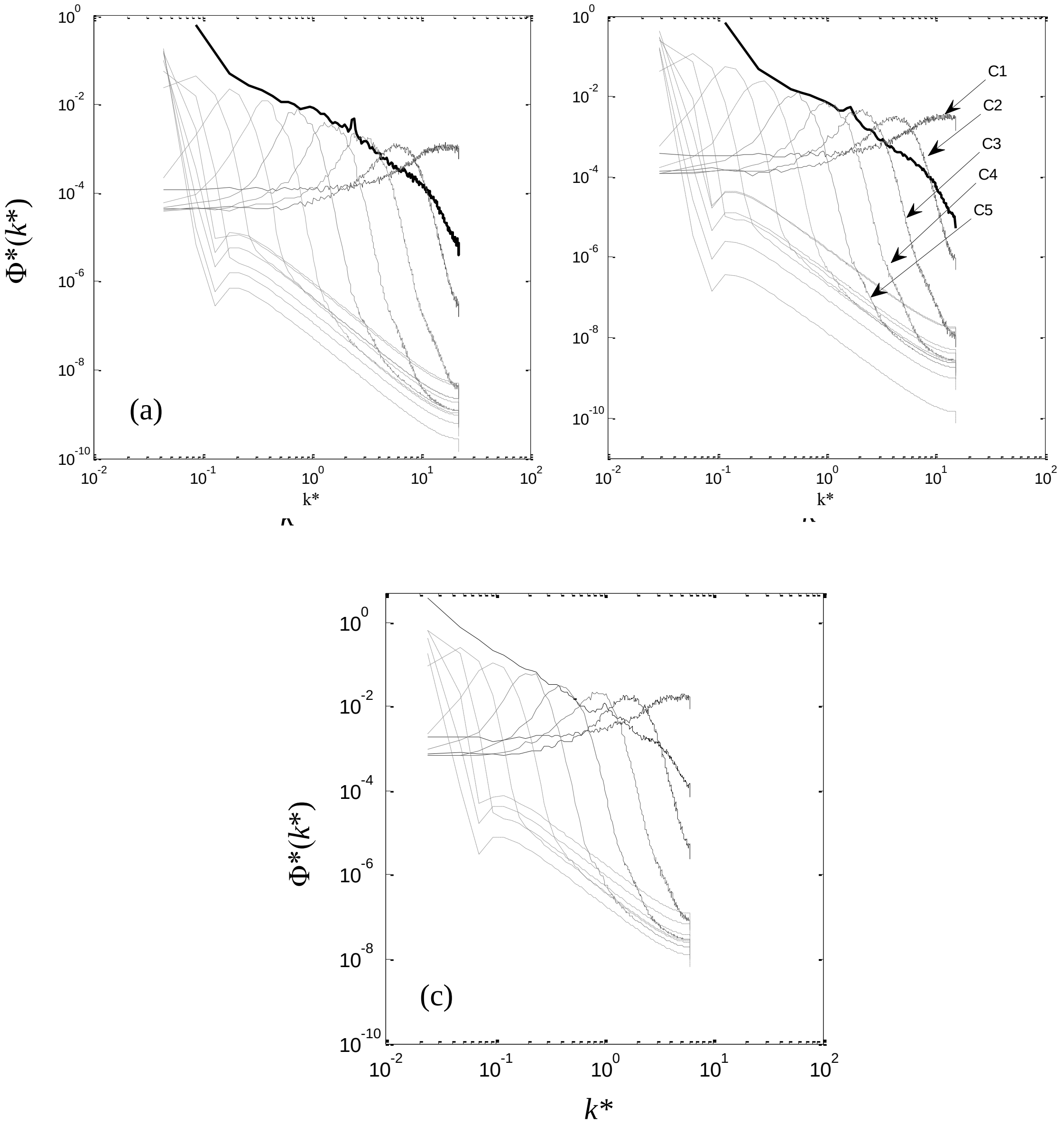

Figure 4.3 - Power Spectral density for D = 25.1 mm, for a) p/D = 1.16, b) p/D = 1.26, c) p/D = 1.60. $Re = 1.44\times10^4$.

Performing a correlation coefficient analysis between the IMF components and the velocity signal, it is possible to identify which IMF component is more related to the original signal, and therefore may contain more information about it. Figure 4.4 presents the results for the correlation between each IMF and the signal, for the various *p/D*, and *Re* = $1.44\text{x}10^4$. The correlation coefficient for a single cylinder with *D* = 25.1 mm at the same Reynolds number was used as a reference. It is possible to observe that for the same Reynolds number, the aspect ratio plays an import role on which IMF presents the highest correlation coefficient. For *p/D* = 1.16 the most correlated is component C12, for *p/D* = 1.26 is component C11 and for *p/D* = 1.60 is component C9. The IMFs, one previous and one after those mentioned, also present a significant correlation coefficient, indicating that the most relevant information about the bistable flow is in the IMFs of lower frequency. The correlation coefficient for C16 is very similar for all the *p/D* cases, varying from 0.1781 to 0.2611, but since IMF C16 is very close to the residue, it may be an artifice of the method.

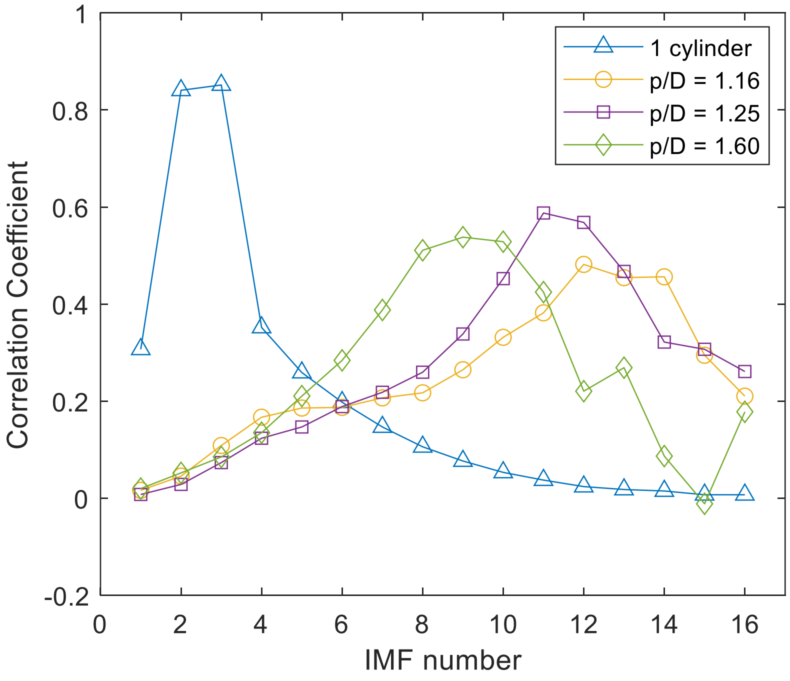

Figure 4.4 – Correlation coefficient between IMF components and the velocity time series, for *D* = 25.1 mm, for a single cylinder and *p/D* = 1.16, 1.26, and 1.60 for two cylinders side-by-side. *Re* = 1.44×10^4.

The signal can be reconstructed by summing all the IMF components. To verify the previous results about the correlation between IMFs and data, only IMFs from 16 to 11 were added. Figure 4.5 shows the results for IMF reconstruction and compares with the DWT reconstruction of level 9, using a db20 wavelet. The reconstruction using only the low frequency IMFs made it possible to observe the bistable characteristics without the turbulent part and therefore was considered a good representation of the signal and the method very effective as a filter. The results are very similar to those found using the DWT, but not equal, due to the characteristics of the EEMD the reconstructed signal may present negative values, the exception in the studied cases, being the one for $p/D = 1.60$, which is almost an exact match to the DWT reconstruction.

The NHES originated from the NHT of the IMFs is shown in Fig. 4.6. Different from the single cylinder case, where the vortex shedding frequency and its harmonics are clearly identified (see Appendix A, Fig. A.8), the NHES of the two cylinders case in a bistable flow does not highlight any specific range of frequency related to vortex shedding. In the low frequencies, it is possible to visualize a concentration of energy resembling the bistable behavior, but the frequencies related to each wake mode are not identified.

Taking into account that bistability is a low frequency phenomenon, which is corroborated with the previous results, an NHES of only the 6 lower IMF components is presented in Figure 4.7. The results are shown for 65 seconds of data.

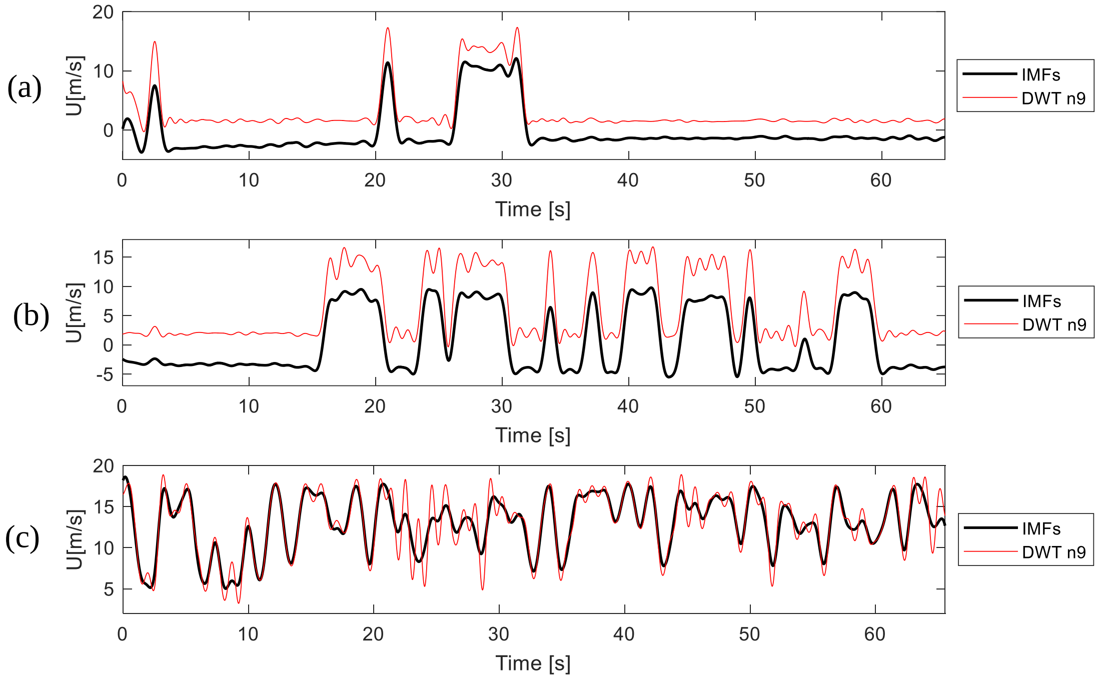

Figure 4.5 – Reconstruction using IMF components from C11 to C17 (black line) compared with DWT reconstruction of level 9 (red line), *D* = 25.1 mm, for a) *p/D* = 1.16, b) *p/D* = 1.26, c) *p/D* = 1.60. *Re* = 1.44×10^4.

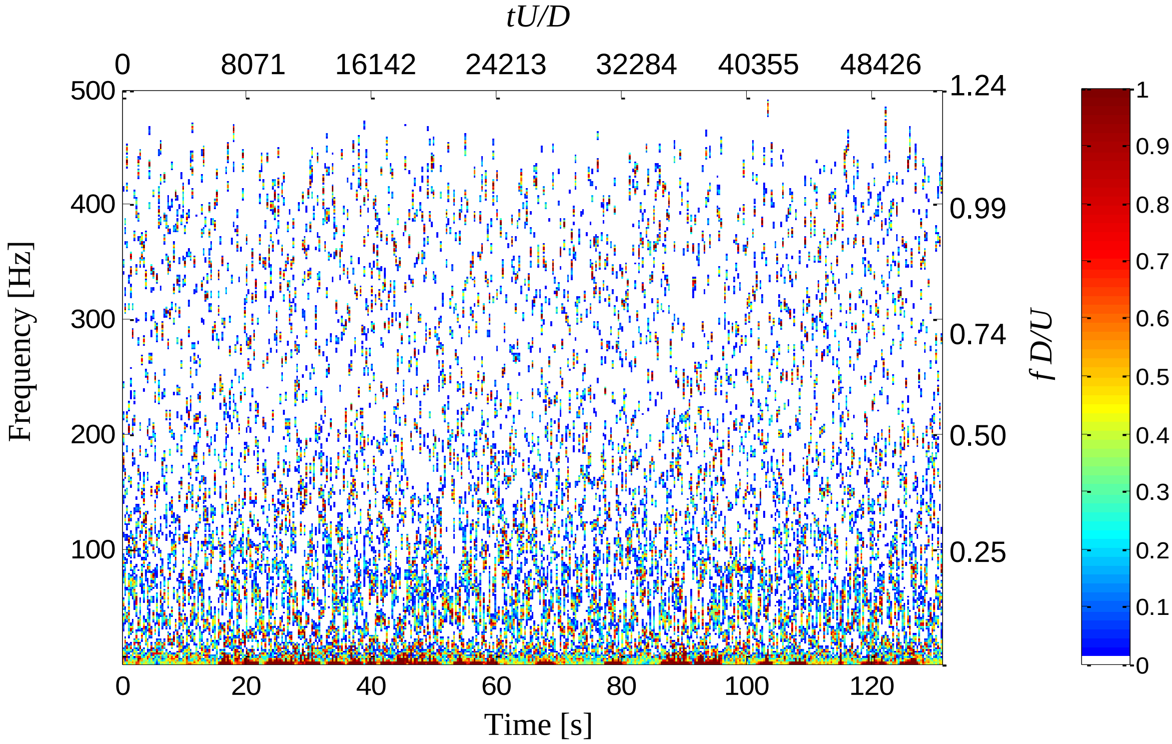

Figure 4.6 – Normalized Hilbert spectrum for *D* = 25.1 mm. *p/D* = 1.26, *Re* = 1.44×10^4.

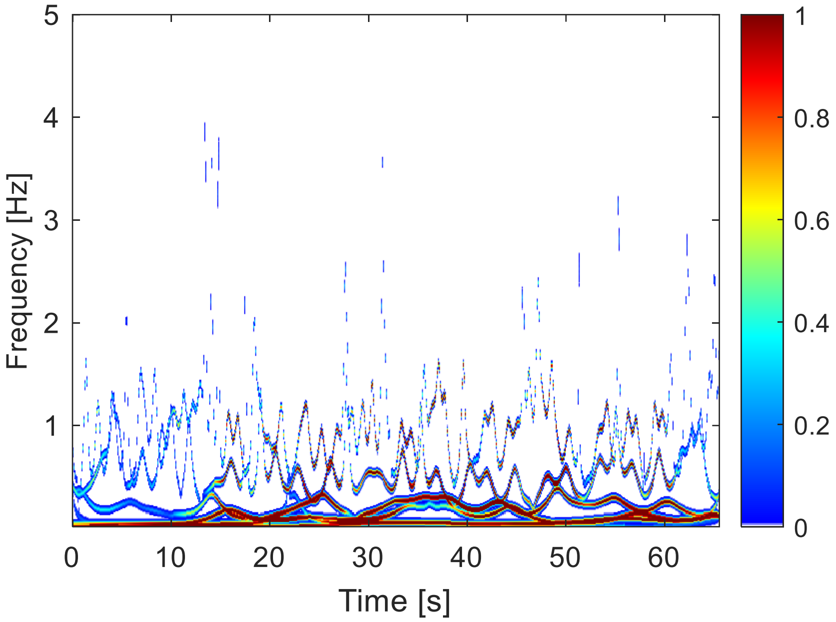

Figure 4.7 – Normalized Hilbert spectrum of IMFs C11 to C16, for D = 25.1 mm. p/D = 1.26, $Re = 1.44\times10^4$.

For quantitative analysis of the energy of each IMF, the dimensionless Mean Square Energy (MSE), as an estimation measure, was defined as follows [Meng et al., 2012]

$$MSE_j = \frac{1}{N}\sum_{t=0}^{T}\left[c_j\right]^2 / U^2 \qquad (48)$$

where N represents the length of the velocity series, T represents the sampling time, j represents the IMF order and U is the reference velocity.

The results for MSE for the various p/D at the same Reynolds number, are represented in Figure 4.8. While for the single cylinder, the energy peak was concentrated in one IMF (usually a high frequency component) followed by a gradual decrease of energy (see Apendix A, Fig. A.10), in the bistable flow, a peak of energy can be found in the first IMF, C1. The energy then decreases from IMFs C2 to C7 for all the aspect ratios, and then increase until reaching the maximum values. Energy peaks are located in C14, C11, and C10 for p/D = 1.16, 1.26, and 1.60 respectively, followed by an energy decline in the subsequent IMF components. This behavior is very likely connected to the bistable phenomenon and the two frequencies related to the wide and narrow wakes. Another possible cause is that the changes in the wake flow are caused by an interaction in the vortices after the cylinder, causing an energy concentration in the fine scales of the flow, causing the energy peak in C1. The vortices interaction results in a larger vortex, culminating in the energy peak in the higher IMF components.

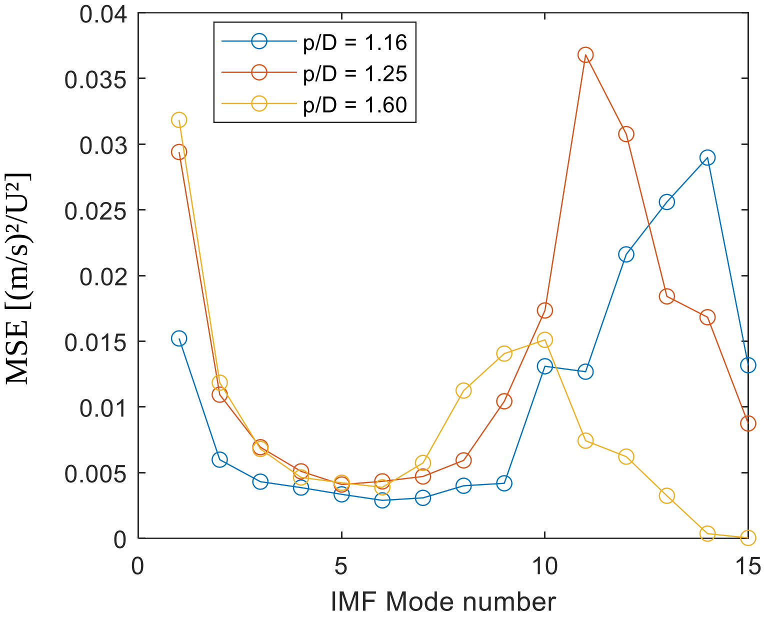

Figure 4.8 – Dimensionless mean square energy for *D* =25.1 mm. *p/D* = 1.16, 1.26, and 1.60. *Re* = 1.44×10^4.

The joint PDF of the first five IMFs of the bistable signal is shown in Figure 4.9 for *p/D* = 1.26 and *Re* = $1.44\text{x}10^4$. One can see that the first component C1 presents higher amplitude when compared to the other IMFs distribution. Subsequent IMFs superimposed themselves in frequency, but present a regular amplitude. The IMFs also tend to present a higher concentration of amplitude in frequencies lower than 50 Hz, since bistability is a low frequency phenomenon.

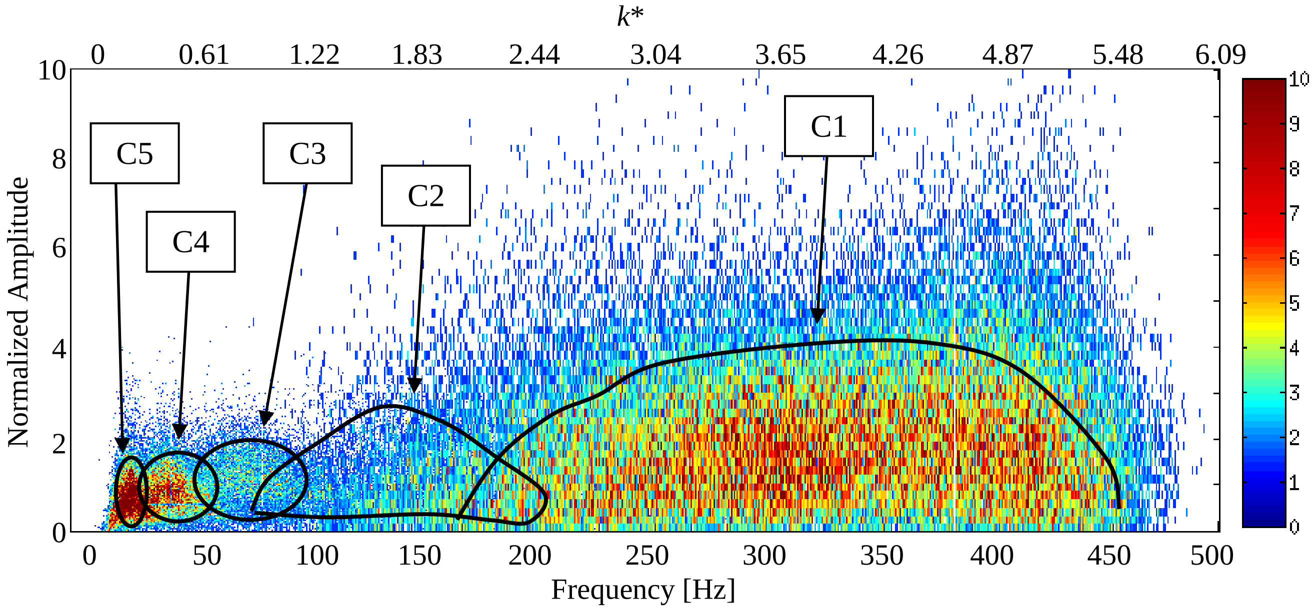

Figure 4.9 – Joint PDF of amplitude and frequency for D =25.1 mm. p/D = 1.26, $Re = 1.44\times10^4$.

The influence of the Reynolds number was analyzed for p/D = 1.26. Results for the correlation coefficient between IMFs and the velocity signals are presented in Figure 4.10. Observing the results there seems to be no direct influence of the Reynolds variation on the correlation coefficient for p/D = 1.26. For most of the Reynolds numbers, the IMF with a higher correlation is IMF C11, exceptions are for $Re = 1.14\text{x}10^4$ for which is IMF C9, and $Re = 2.32\text{x}10^4$ with IMF C13, but even for those cases, IMF C11 presents a significant correlation value.

The dimensionless mean square energy was calculated for the various Reynolds and presented in Figure 4.11. As it is possible to see, the value of the mean square energy of the first IMF component is influenced by the Reynolds number. The first IMF component, for the higher Reynolds, present higher values of MSE. The values decrease until IMF C6 for all Reynolds numbers evaluated, and then increase from IMF C7 reaching the maximum value in IMF C11.

Those results may represent the fact that the frequency at which the bistability phenomenon mainly occurs, which is, at lower frequencies, does not suffer any influence of the Reynolds number, still the aspect ratio, p/D could be considered a parameter that influences significantly the energy distribution. Nevertheless, as will be seen in the last section of results, the pseudo frequency at which the mode changes is influenced by both parameters, Reynolds number variation, and *p/D*.

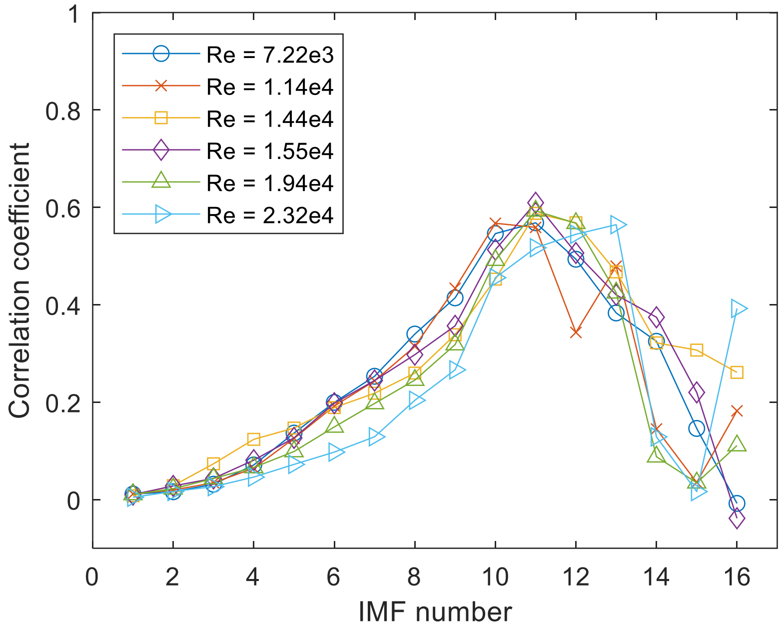

Figure 4.10 – Correlation coefficient for various Reynolds numbers, with *p/D* = 1.26.

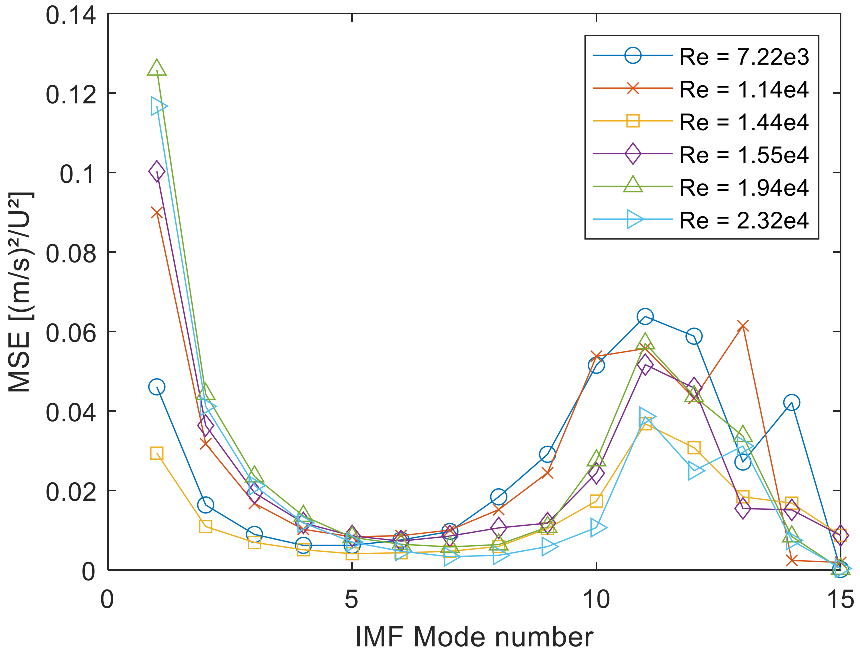

Figure 4.11 – Dimensionless mean square energy for various Reynolds numbers, and *p/D* = 1.26.

4.2 Statistical analysis of bistable flow

The statistical analysis described in Section 3.5 was performed in a fragment of the velocity time series. For each *p/D* and Reynolds number, a piece of 8 seconds of the signal was chosen, taking into account that it should capture the bistable phenomenon properly. Those fragments of data were then separated into dyadic blocks that overlapped each other. Each block created a PDF. A representation of the process is represented in Figure 4.12. It is possible to identify the fragment of eight seconds of data and the 125 points used in the PDFs were marked in black in different parts of the data set, representing pieces of the large and narrow wake, and between both wakes.

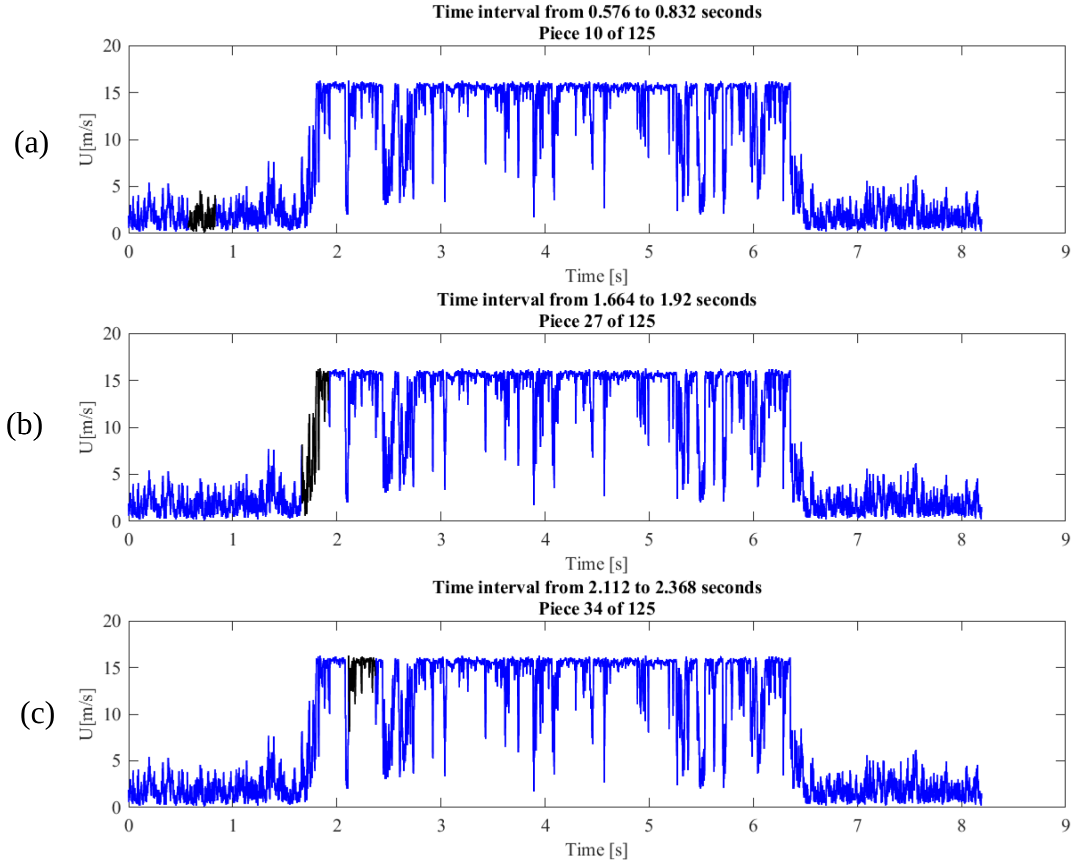

Figure 4.12 – Fragment of eight seconds for *p/D* = 1.26. *Re* = 1.44x10^4. The window of 125 points, in black at a) Large Wake, b) Large and Narrow wake simultaneously and c) Narrow Wake.

The PDFs created by the method can be approximated by a distribution function (de Paula, 2013 used an asymmetric *t*-Student). Figure 4.13 shows the PDFs representing each wake mode, and the place corresponding to the three 125 blocks of data points shown in Fig. 4.12. When the signal is at the large wake the PDF histogram concentrates in the lower values of velocity, the distribution has positive asymmetry and presents a tail in the high values, consequently higher values of variance. When the signal comprehends a mode change, meaning, part of it is in the large wake, and part in the narrow wake, the PDF presents two curves, being the combination of two probability distributions. And when the signal is in the narrow wake, the distribution is narrowed and concentrates in the higher values, with a negative asymmetry.

Table 2 summarizes the statistical values of some of the Reynolds numbers analysed by the method for p/D = 1.16, 1.26 and 1.60.

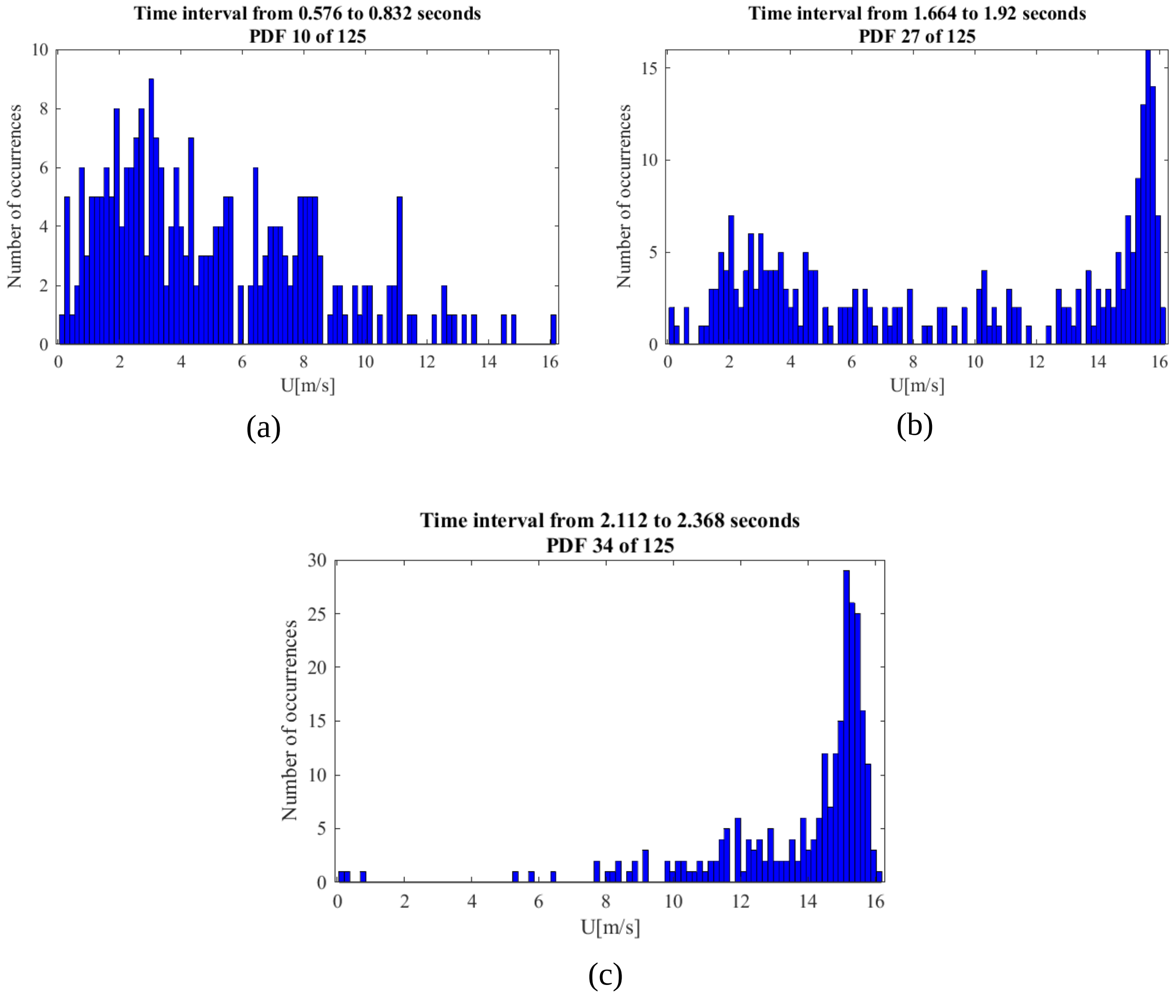

(a)

(b)

(c)

Figure 4.13 – PDFs representing the blocks of 125 points of data. a) Large wake, b) transition from large to narrow wake and c) Narrow wake. *D* =25.1 mm. *p/D* = 1.26. Re = 1.44×10^4.

Table 2 – Time series statistical characteristics for various Reynolds numbers.

Time series	*Re* = 7.22x10^3		*Re* = 1.44x10^4		*Re* = 2.32x10^4	
p/D = 1.16						
	N.W*	W.W**	N.W	W.W	N.W	W.W
Mean (m/s)	5.01	1.99	13.49	2.22	16.75	4.18
Std. deviation	2.51	2.14	5.04	1.22	6.11	2.79
Kurtosis	1.60	4.44	3.46	3.86	1.56	12.90
Skewness	-0.41	1.63	-1.38	0.91	0.257	2.65
p/D = 1.26						
	N.W	W.W	N.W	W.W	N.W	W.W
Mean (m/s)	7.86	1.88	13.17	1.91	20.44	6.17
Std. deviation	0.72	1.86	3.59	1.16	0.77	3.79
Kurtosis	45.72	6.79	5.97	9.55	79.49	7.95
Skewness	-6.04	2.06	-2.02	1.59	-6.69	2.05
p/D = 1.60						
	N.W	W.W	N.W	W.W	N.W	W.W
Mean (m/s)	5.03	3.11	16.42	8.15	15.23	9.59
Std. deviation	2.81	2.35	1.97	4.66	6.24	6.48
Kurtosis	1.46	3.00	22.84	2.37	1.93	2.09
Skewness	-0.06	1.08	-4.27	0.72	-0.57	0.73

*N.W – Narrow Wake
**W.W – Wide Wake

Figure 4.14.a) shows the velocity time series of a bistable signal, for *p/D* = 1.26, for *D* = 25.1 mm. The bistable characteristics of the signal are identified by the alternation between the two velocity levels, the small velocity values corresponding to the large near wake, and the higher velocity values to the narrow near wake. The mean value of each PDF is showed in Fig. 4.14. b).

Figure 4.14.c) shows the variation of normalized standard deviation for each of the 125 blocks of the signal. It is possible to associate the behavior of the standard deviation with each wake mode. When the signal is in the large wake, from block 1 to 26 and 100 to 125, corresponding to the small velocity, the standard deviation has values in the range of 0.45 to 0.85. Those values reduce when the signal changes mode into the narrow wake, corresponding to PDF blocks from 27 to 99, or the higher velocity values. Then the standard deviation values became lower, in the range from 0.46 to 0.02. The moment the wake changes mode is preceded by an increase in the standard deviation values, corresponding to the peaks found in blocks 26 and 100. The signal also has some mode changes attempts that caused the smaller peaks in blocks 39, 61, and 84.

Figure 4.14.d) shows the variation of the skewness for each PDF block. It is possible to associate the skewness behavior to the standard deviation behavior and the signal mode

changes. When the signal is in the large wake skewness values are positive, (blocks 1 to 26) coinciding with the higher values of standard deviation. When the mode changes to the narrow wake, the skewness values became negative, (block 27 to 98) coinciding with the lower values of standard deviation. The instant the signal changes from one wake to the other is marked by a peak in the skewness values, in blocks 24 and 100. The skewness peaks are also found in blocks 39, 61, and 84, which would correspond to the instant when the signal tries to change mode but fails.

Figure 4.14.e) shows the variation in kurtosis for each PDF block. Kurtosis presents almost constant values, around 2 and 3.2, when the flow is in the large wake. Around the PDF blocks that include the mode change, some peaks on the values start to appear. When the mode changes to the narrow wake, from block 29 to 100, kurtosis presents high peaks, reaching values like 28 in block 52, intercalating with lower values, which may be related to the flow trying to change mode again. This inconstant behavior can also be related to the fact that kurtosis is associated with the tails of the distribution, and when in the narrow wake, the fluctuation values present a large range, producing a longer tail (more outlier values than a Gaussian distribution for example) in the distribution. One could also say that the narrow wake distribution approaches zero more slowly. Around block 100 the values of kurtosis tend to reduce back to the range of values of 5 to 2.

A very similar behavior, and very similar range of values were found for the four statistical moments for p/D = 1.16 (Fig. 4.15) and 1.60 (Fig. 4.16), at the same Reynolds number. This concludes that at the same Reynolds number, the aspect ratio p/D does not directly influence the variation of the statistical moments of the bistable large and narrow wakes.

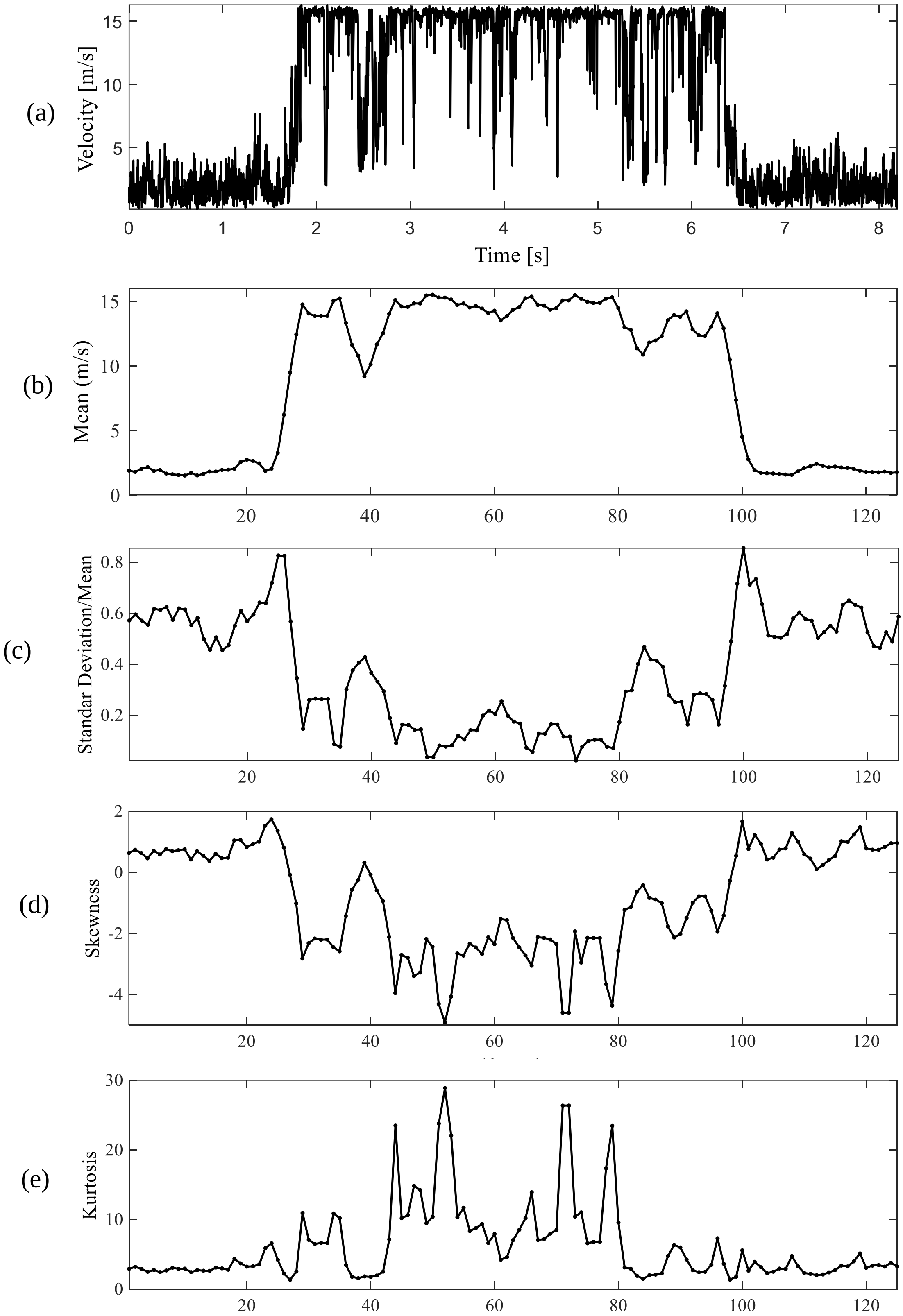

Figure 4.14 – Velocity signal and the variation of statistic moments for each PDF block for *p/D* = 1.26, *Re* = $1.44\text{x}10^4$. a) Velocity signal, b) mean values, c) standard deviation normalized by the local mean, d) Skewness and e) Kurtosis.

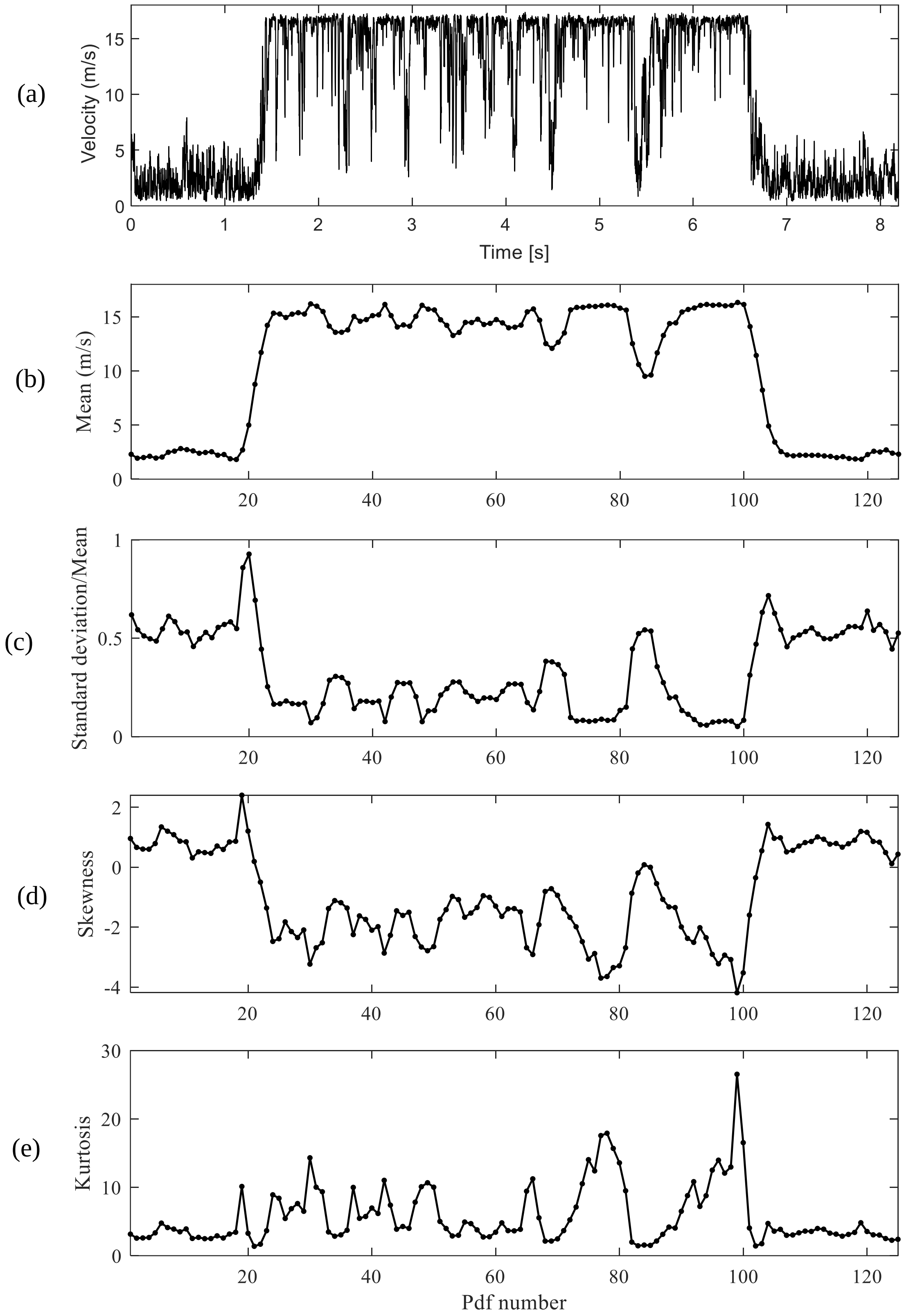

Figure 4.15 – Velocity signal and the variation of statistic moments for each PDF block for *p/D* = 1.16, *Re* = 1.44x10^4. a) Velocity signal, b) mean values, c) standard deviation normalized by the local mean, d) Skewness and e) Kurtosis.

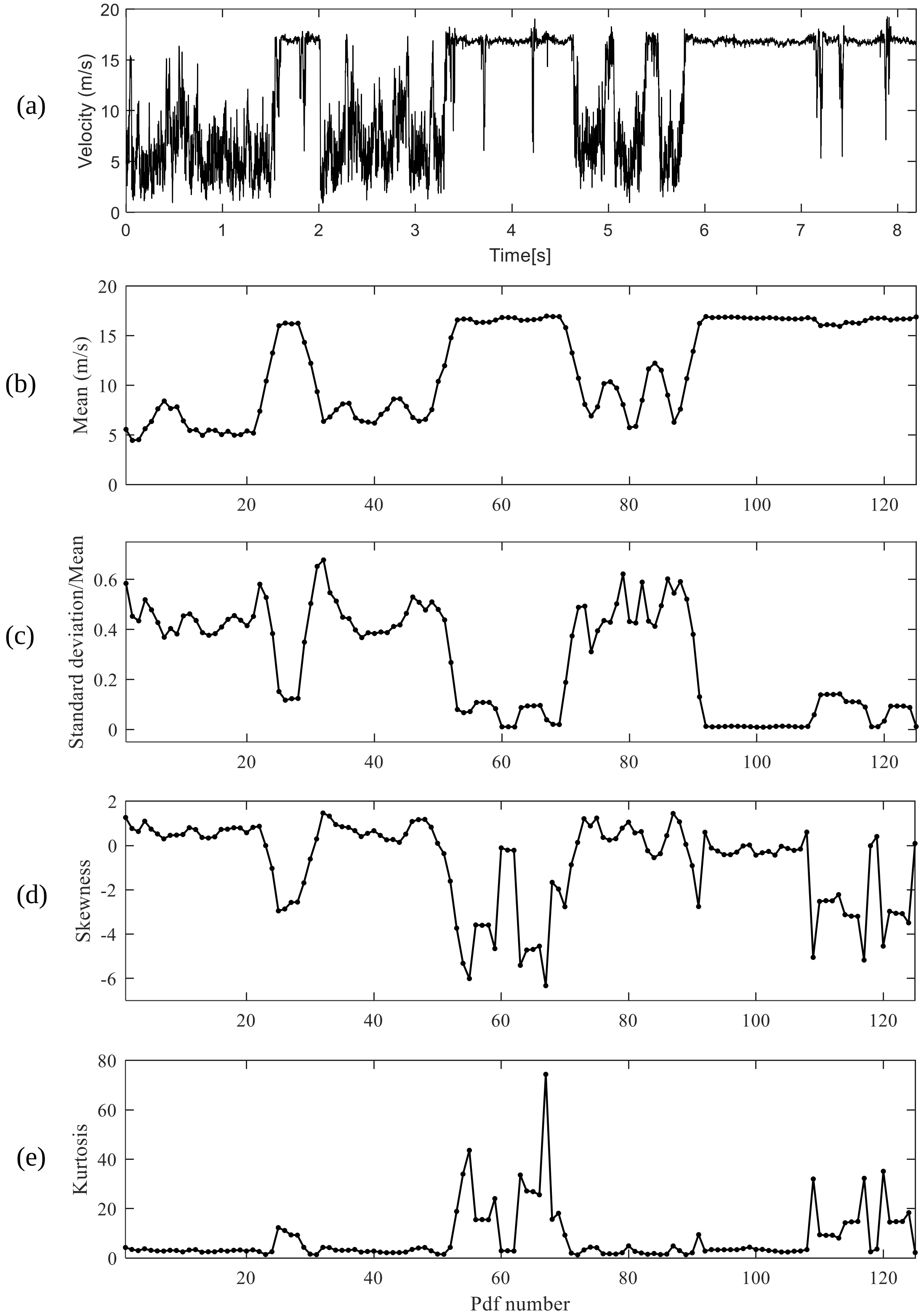

Figure 4.16 – Velocity signal and the variation of statistic moments for each PDF block for *p/D* = 1.60, *Re* = 1.44x10^4. a) Velocity signal, b) mean values, c) standard deviation normalized by the local mean, d) Skewness and e) Kurtosis.

After analyzing each set of eight seconds of data set, the influence of the Reynolds number on the behavior of the statistical moments of the bistable signals was considered. The analysis was made for *p/D* = 1.26, for multiple Reynolds numbers. The maxima, minima, and mean values were collected from the 125 PDF blocks.

Figure 4.17 shows the results for maxima, minima, and mean values for the normalized standard deviation. The mean and the minimum value have very little variation and can be considered constant for the range of Reynolds numbers considered. The maximum value presents a decrease between the smaller Reynolds number (Re = 7.22x10^3) and the higher Reynolds number (Re = 2.32x10^4). This variation is ± 0,2948 and can be a function of the fragments of data analyzed.

Figure 4.18 shows the results of maxima, minima, and mean values of skewness for *p/D* = 1.26, for various Reynolds. It is possible to see that the values are not significantly influenced by the variation on the Reynolds number. The mean values are concentrated around zero as expected. Maxima and minimum values present some oscillations, but in general, they can be considered constant.

Figure 4.19 presents the variation of maxima, minima, and mean values kurtosis for *p/D* = 1.26, with various Reynolds numbers. Minimum and mean values are constant for all Reynolds numbers analyzed. The maximum values on the other hand are around the same value for three of the studied Reynolds numbers but present much lower values for Re = 7.22x10^3 and 1.55x10^4. Those lower values may be associated with the presence of more or fewer fluctuations in the analyzed data fragment.

Those results demonstrate that it is possible to establish patterns for the statistical behavior of the large and narrow wake in bistable flows, and for the subcritical range those values do not depend on the Reynolds number nor on the *p/D* ratio. Finding patterns in the behavior of the large and narrow wakes provides a first step in developing a potential method to describe and recreate bistability dynamics.

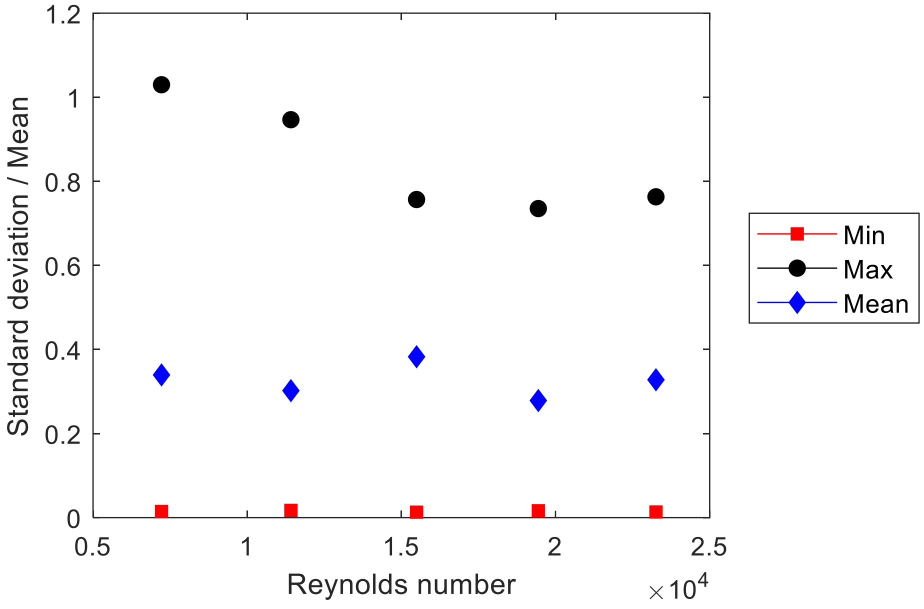

Figure 4.17 – Normalized Standard Deviation variation for various Reynolds numbers. *p/D* = 1.26.

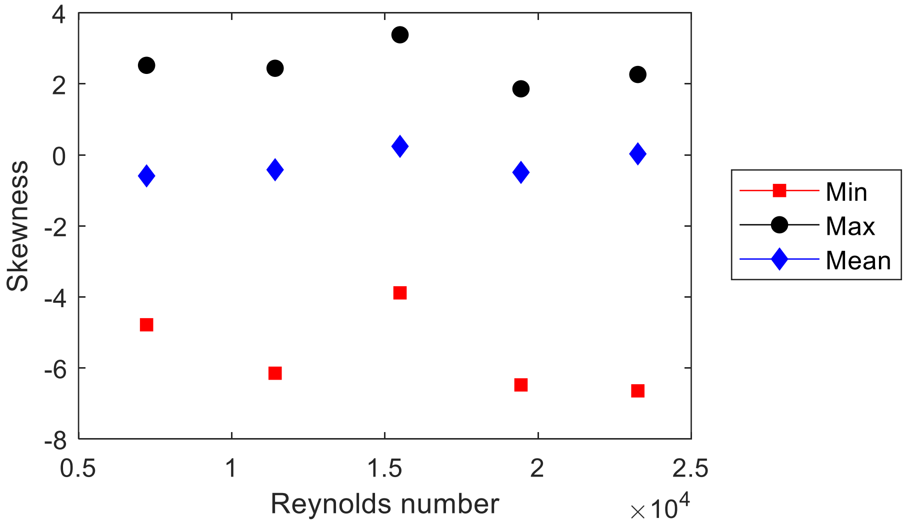

Figure 4.18 - Skewness variation with the Reynolds number. *p/D* = 1.26.

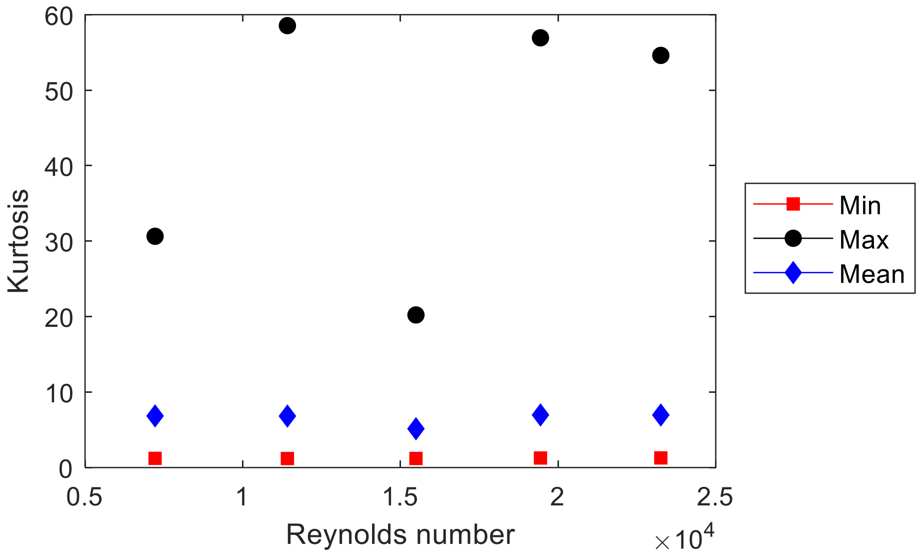

Figure 4.19 - Kurtosis variation for various Reynolds numbers. *p/D* = 1.26

4.3 Chaos and stability

The velocity time series acquired experimentally for two cylinders side-by-side for *p/D* = 1.16, 1.26, and 1.60, and *Re* = $1.44\text{x}10^4$ are shown in Figure 4.20. Those time series were filtered using discrete wavelet transform (DWT), with a db20 wavelet and a reconstruction detail of level 9, which corresponds to 0.956 Hz of bandwidth, and the results are represented in black, superposed on the velocity time series. Reconstructing the signal with a DWT serves the purpose of eliminating the turbulent part of the data set, reducing noise, and resulting in a signal with fewer fluctuations.

The strange attractors created using the filtered time series, are represented in 3D in Figure 4.21 a). The attractors were created by calculating the first and second derivatives of the filtered velocity signals in time. For better visualization of the behavior each plane is separately plotted in Figure 4.21 b), c), and d). In Figure 4.21.b) the plane containing velocity and its first derivative (acceleration) is represented and is possible to identify two basins of attraction where the points orbit around. These basins of attraction can be associated with the large and narrow wake of the system in the velocity axis. In the derivative axis, the basins of attraction are aligned around zero and it is observed that the acceleration increases (in positive and negative values) in the path between the two basins of attraction.

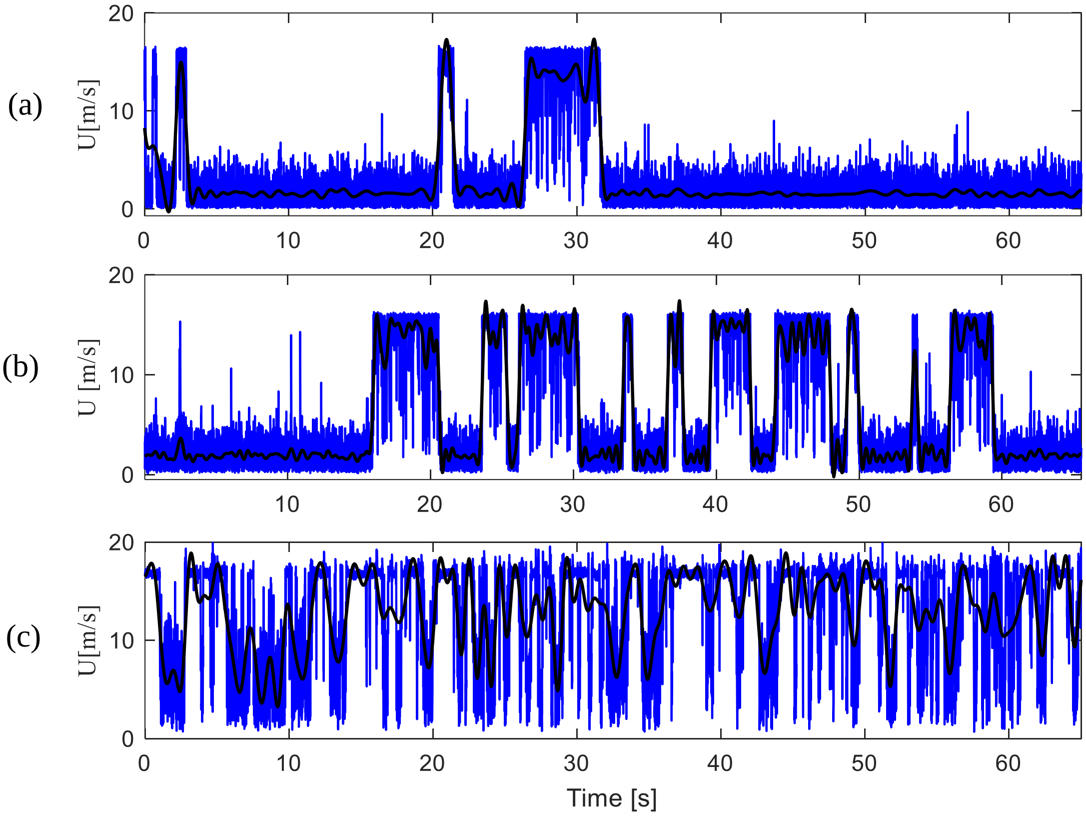

Figure 4.20 – Velocity time series and DWT reconstruction of level 9 (0.976 Hz). a) *p/D* = 1.16, b) *p/D* = 1.26 and c) *p/D* = 1.60. *Re* = 1.44×10^4.

Figure 4.21.c) represents the velocity and its second derivative (called jerk). Jerk represents the rate at which acceleration changes with respect to time. In an ordinary system of differential equations, jerk equations are the minimal setting for solutions showing chaotic behavior. It is possible to observe that when the particles are around the basins corresponding to the large wake, identified by the small velocity values, jerk increases before the particle is pulled towards the narrow wake basins of attraction (higher velocity values). In the trajectory between large wake and narrow wake basins, jerk reduces its values, reaching its minimum before the particle is pulled around the narrow wake basins. The inverse process happens when the particle leaves the narrow wake towards the large wake.

Thinking about the physical meaning of this process for the dynamic system, one could say that, when the system found itself in one of the lower energy states (meaning: deviated towards one of the cylinders) the acceleration rate is small and almost constant. Also, for the system to alternate to the other state of lower energy, the acceleration rate must increase, but in the path between the two states, the acceleration rate decreases again. One can also think of this effect as a slingshot effect, accumulating energy for propelling the flow and causing the wake mode to change.

In Figure 4.21.d) the combination of first and second derivatives is represented. It is possible to see the relationship between jerk and acceleration. When jerk starts to increase, acceleration also increases, when jerk reaches its maximum values and starts to decrease, acceleration keeps increasing. When jerk is zero, the increment of acceleration is also zero. This is observed in the left and right sides of the graphic since it is an almost symmetric phenomenon.

The strange attractors generated for *p/D* = 1.16 and 1.60 are represented in the isometric view in Figure 4.22. a) and b). the effect of the mode changing is visible in the attractors, *p/D* = 1.16 presents very little switching and therefore one of the basins of attraction is more evident than the other. Since *p/D* = 1.60 is almost a flip-flop, with very intense mode changing, the strange attractor does not divide itself into two basins of attraction, becoming tangled trajectory in the central region of the phase space.

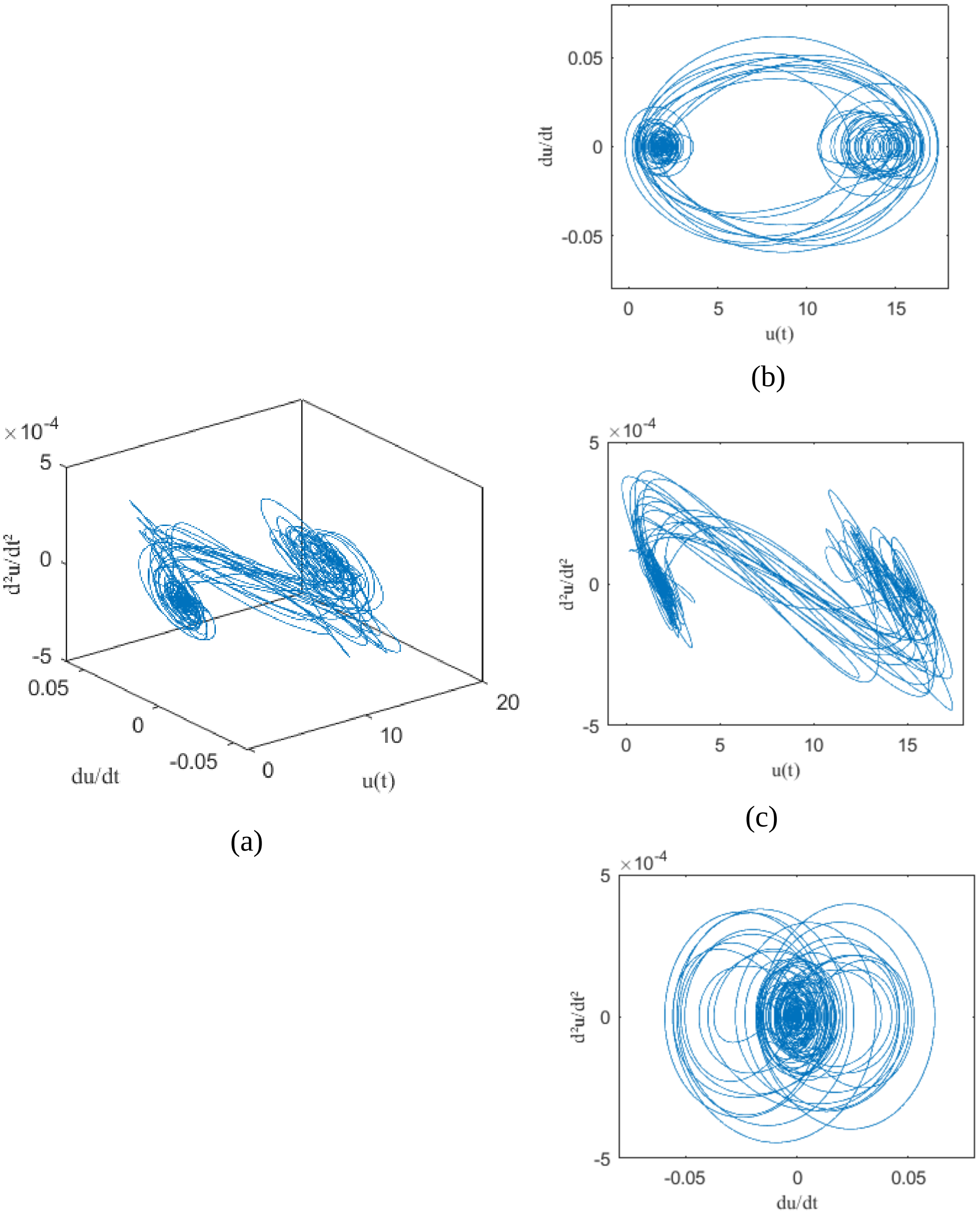

(b)

(a)

(c)

(d)

Figure 4.21– a) 3D strange attractor for the bistable signal with *Re* = 1.44x10^4 and *p/D* = 1.26. b) velocity × first derivative plane, c) velocity × second derivative plane, and d) first derivative × second derivative plane.

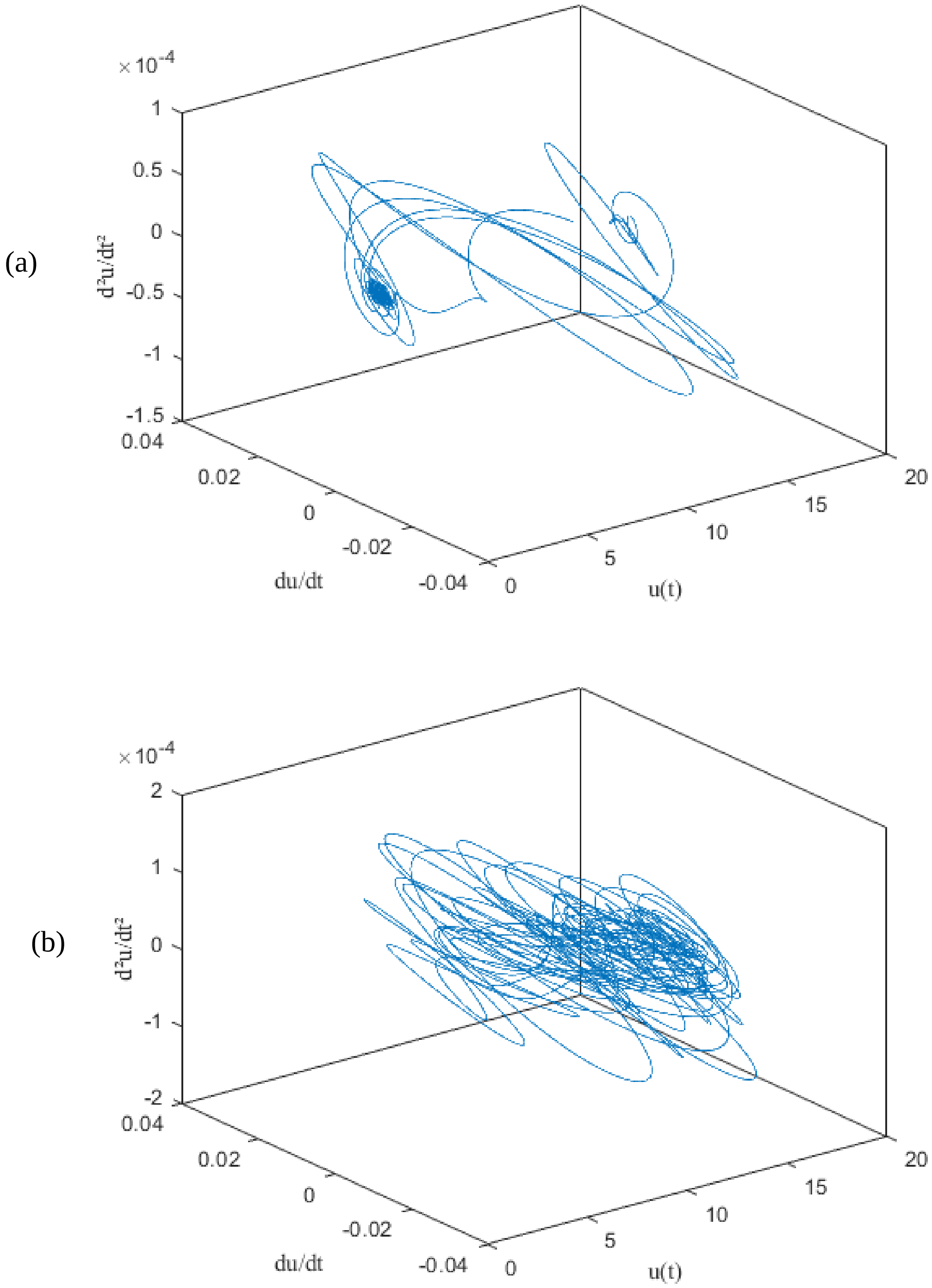

Figure 4.22 – a) 3D strange attractor for *p/D* = 1.16 and b) 3D strange attractor for *p/D* = 1.60. *Re* = $1.44\text{x}10^4$.

The Lyapunov exponent can be interpreted as a rate at which the system loses predictability. For the Lyapunov exponent, the phase space was reconstructed using a time delay (or time lag). In de Paula and Möller (2018), a wide range of embedded dimensions and time lags used for this purpose were analyzed, and the values chosen in this paper were based on the same method of choice. A too small time lag will linearly compress the data in the diagonal of the phase space, and a too large time lag will disperse it in the whole phase space. The best result for the time lag (*T*) for the time series presented in this study was for the values of, $T = 50$, 100, and 200, for p/D = 1.16, 1.26, and 1.60 respectively. All the parameters used to evaluate the bistable data sets are in Table 3.

Table 3 – Parameters used to evaluate the filtered bistable time series.

Time series	$Re = 7.22\text{x}10^3$	$Re = 1.44\text{x}10^4$	$Re = 1.94\text{x}10^4$	$Re = 2.32\text{x}10^4$
Frequency sampling (f_s)	1000 Hz			
Sampling period (Δt)	0.001 s			
Critical distance (R_t)	20, 50, 100 and 200			
Critical limit (A_c)	2			
Number of data points (N)	65,536			
Time lag (T)	50, 100 and 200			
Embedding dimension (De)	1 to 10			

Figure 4.23, shows the phase space reconstruction of the strange attractor using the velocity time series $u(t)$ as the variable, for a time lag of $T = 100$, and can be observed that the data is well distributed in the phase space and not too compressed in the diagonal nor too dispersed. When comparing with Figure 4.21 it is possible to see some distortion and the shape of the 3D reconstruction does not match exactly this of the original attractor, this distortion does not matter for the analysis since the topological properties are preserved.

The percentage of false nearest neighbors (FNN) is estimated using a critical distance R_t (20, 50, 100, and 200), a minimal distance $A_c = 2$, and 10 embedded dimensions, the results for $Re = 1.44\text{x}10^4$ and $2.32\text{x}10^4$ are presented in Figure 4.24. The percentage of FNN in all cases converges to zero after $De = 4$. For $R_t = 20$ the FNN is about 0.393 % and reduces to 0.045 % for $R_t = 200$, for $Re = 1.44\text{x}10^4$. The same behavior is found for $Re = 2.32\text{x}10^4$ (R_t = 20, 0.4223%, R_t = 200, 0.0279%). Very similar behavior was also found for the other Reynolds numbers and p/D analyzed. Therefore, the chosen embedded dimensions for this analysis were 4, 5, 6, and 7.

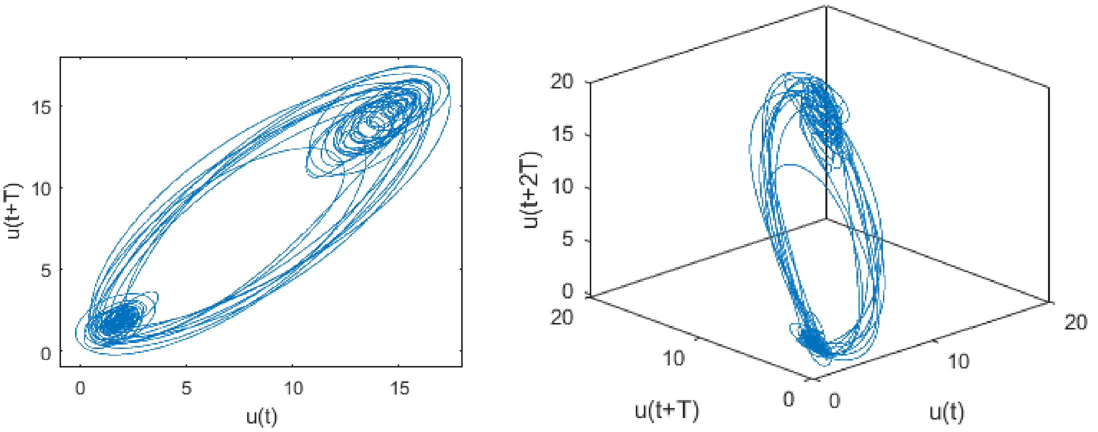

Figure 4.23 – a) 2D phase space reconstruction of the strange attractor and b) 3D phase space reconstruction of the strange attractor, for time lag $T = 100$.

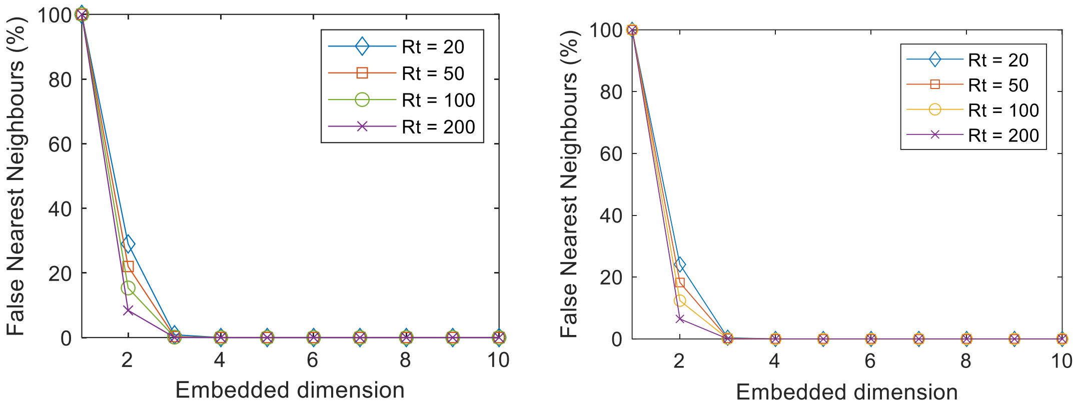

Figure 4.24 – False Nearest Neighbours percentage for various critical distances R_t.
a) $Re = 1.44\text{x}10^4$ b) $Re = 2.32\text{x}10^4$.

The choice of the period for calculating the largest Lyapunov was based on the number of mode changes that occurred in the data, for $p/D = 1.26$ and $Re = 1.44\text{x}10^4$ the wake changed sides 21 times. Therefore, the period of choice was $P = 65{,}536/21 = 3{,}120.7$ data points or 3.1207 seconds. For better visualization, a larger period of 6.000 seconds was shown in the graphics. Thus, the estimated largest Lyapunov exponent is calculated by the mean value of the various slopes in an interval range. For $p/D = 1.26$ at $Re = 1.44\text{x}10^4$ this range is from 0.508 s to 1.050 s and the largest Lyapunov found was $\lambda_1 = 1.5180 \pm\ 0.0734$. The variation of the average ln(divergence) for the Lyapunov exponent is presented in Figure 4.25 for various embedded dimensions. Table 4 presents the largest Lyapunov exponents found for $p/D = 1.16$ at various Reynolds numbers.

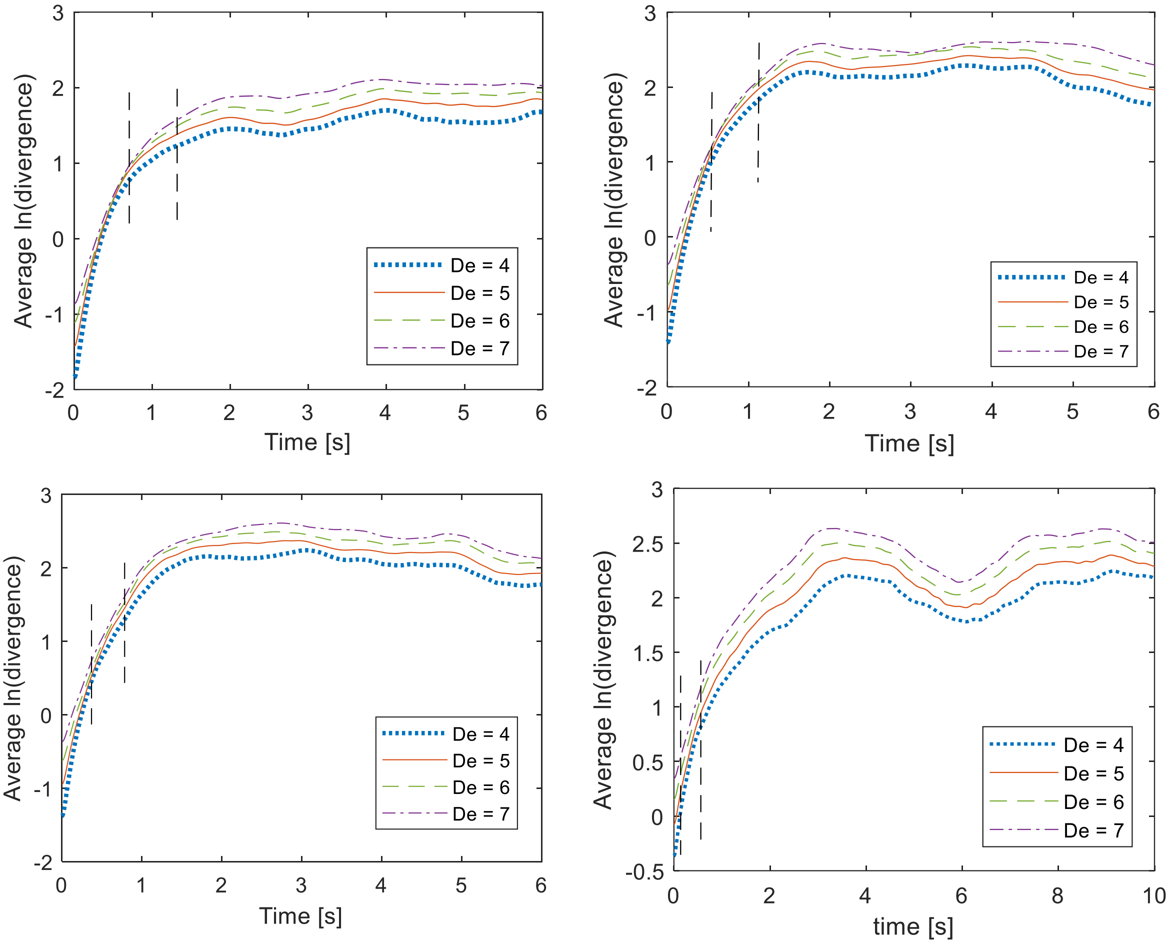

Figure 4.25 – Average ln(divergence) versus time for various embedded dimensions (*De*). a) *Re* = 7.22×10^3, b) *Re* = 1.44×10^4, c) *Re* = 1.94×10^4 e d) *Re* = 2.32×10^4. *p/D* = 1.26.

Table 4 – Largest Lyapunov exponent for various Reynolds numbers for *p/D* = 1.26

Time series	λ_1	Std deviation
Re = 7.22×10^3	0.8375	± 0.1064
Re = 1.14×10^4	1.7826	± 0.1790
Re = 1.44×10^4	1.5180	± 0.0734
Re = 1.55×10^4	1.6859	± 0.0749
Re = 1.94×10^4	2.2773	± 0.1191
Re = 2.32×10^4	1.7644	± 0.2264

Results for the average ln(divergence) for *p/D* = 1.16 behaved similarly as those for *p/D* = 1.26. For *p/D* = 1.60, Reynolds number *Re* = 7.22×10^3 the ln(divergence) was found to behave differently. Instead of the divergence starting negative or at smaller values, increasing and then stabilizing as happened with the other cases, the ln(divergence) started with a higher value, then decreased, and the values did not stabilize but oscillated between higher and lower values. Even though the data is still chaotic and unpredictable, it can be considered unstable, and the largest Lyapunov cannot be found, since a linear region is difficult to establish. Results for various Reynolds numbers and embedded dimensions are pictured in Figure 4.26. For better visualization of the particular case, 10 seconds of data were shown in Fig. 4.26.a).

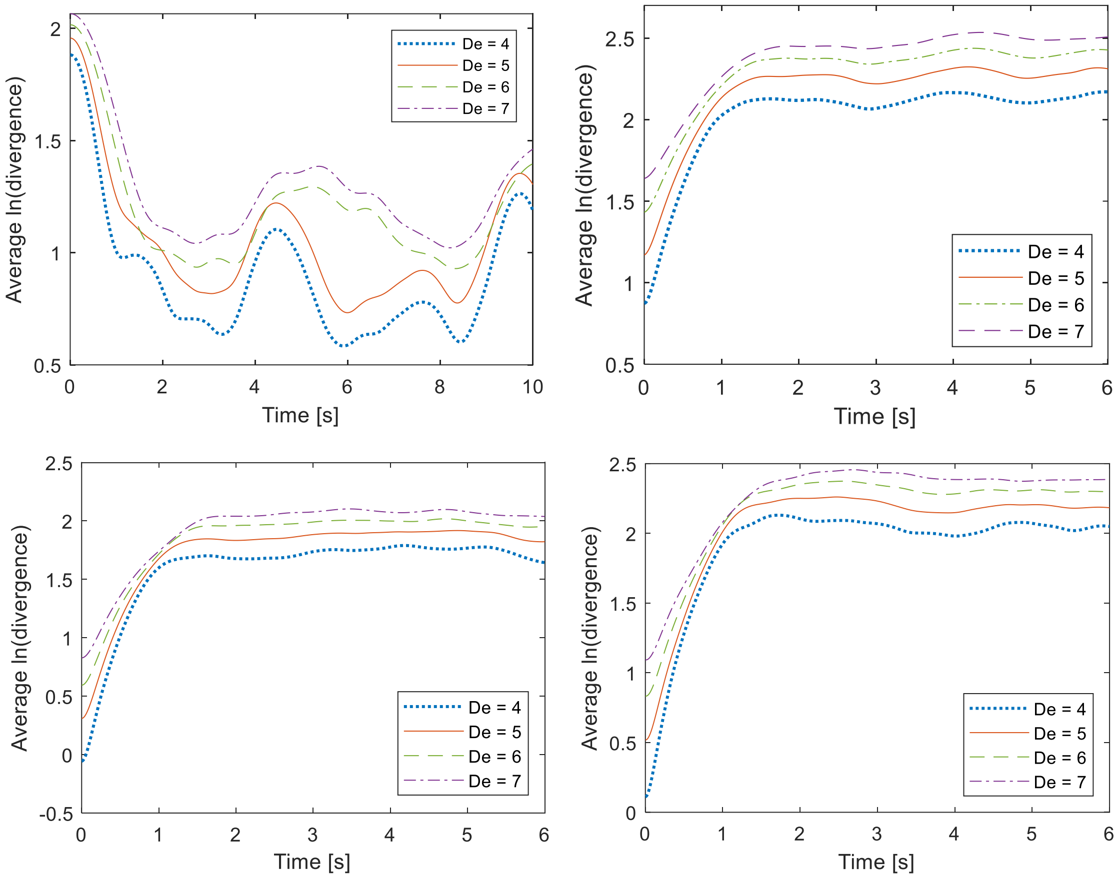

Figure 4.26 – Average ln(divergence) versus time for various embedded dimensions (*De*). a) $Re = 7.22\text{x}10^3$, b) $Re = 1.44\text{x}10^4$, c) $Re = 1.94\text{x}10^4$ e d) $Re = 2.32\text{x}10^4$. $p/D = 1.60$.

The relationship of the largest Lyapunov exponent with various Reynolds numbers for the chosen embedded dimensions is shown in Figure 4.27, Figure 4.28, and Figure 4.29, for $p/D = 1.16$, 1.26, and 1.60 respectively. It is possible to observe that, although the data does not behave in a linear relationship, there is a tendency of the Lyapunov exponent to increase as the Reynolds number increases. Therefore, for higher Reynolds, the tendency is that the system became more unpredictable.

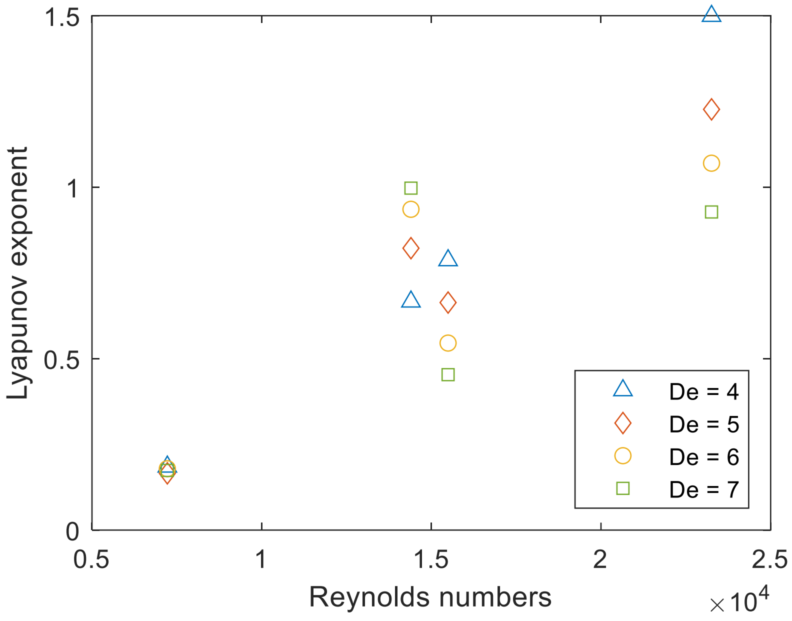

Figure 4.27 – Variation of the Lyapunov exponent with Reynolds number, for various embedding dimensions for *p/D* = 1.16.

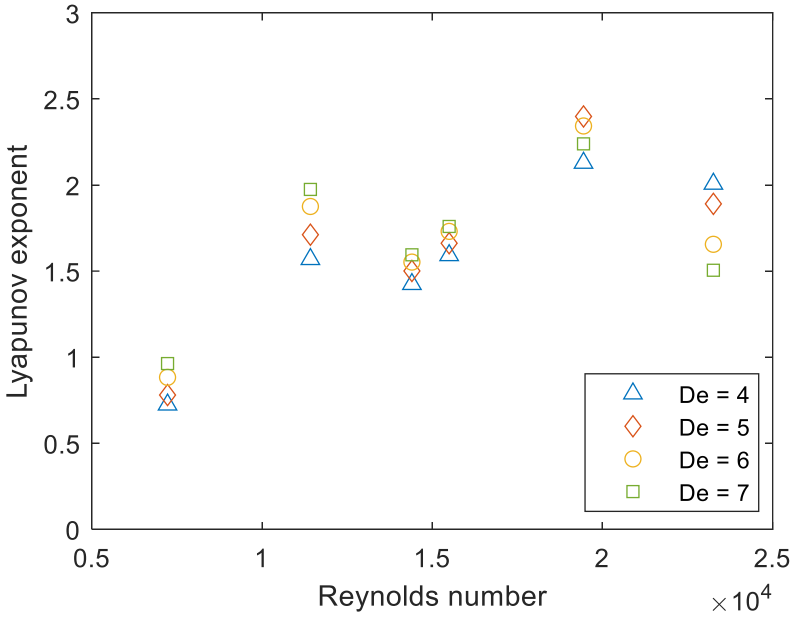

Figure 4.28 – Variation of the Lyapunov exponent with Reynolds number, for various embedding dimensions for *p/D* = 1.26.

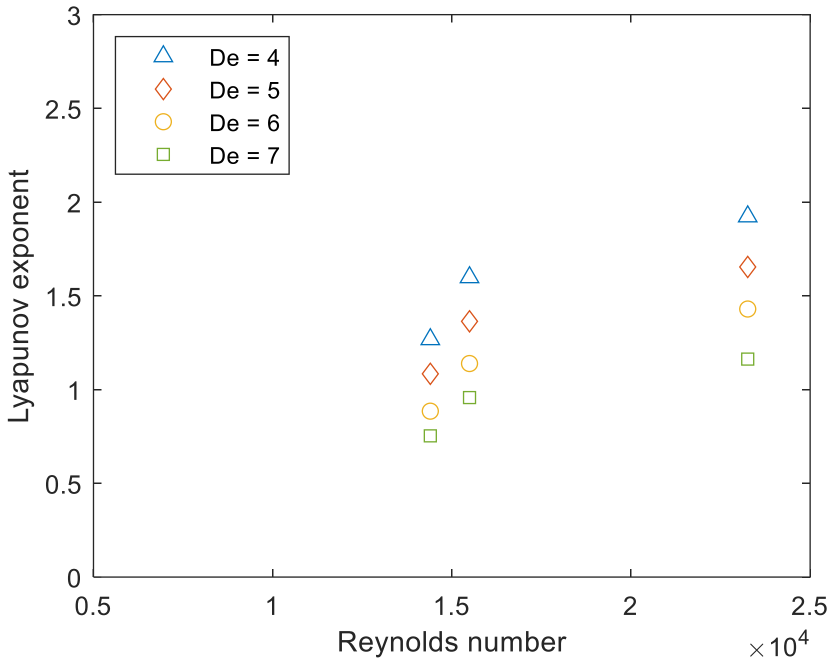

Figure 4.29 – Variation of the Lyapunov exponent with Reynolds number, for various embedding dimensions for *p/D* = 1.60.

This hypothesis can be exemplified by an analogy with a potential function or a double-well energy model. See Appendix B, Fig. B.1 for an schematic example of the following analogy. For a simple mechanical system, considering the potential V(t) to be kinetic energy. For lower values of Reynolds for example, there will be a minimum admissible velocity for the system. Since the system is non-linear, there would be some time instant and some modes where the system would accumulate energy in one of the modes and jump into the other mode. As the Reynolds increases, the contribution of energy became more elevated, meaning that the switch between the two bistable modes became easier since the value of energy that needs to accumulate to jump from one mode to the other is smaller. Therefore, the system became more chaotic and more unpredictable, and eventually, the bistable characteristics would be lost, and the flow would assume a flip-flopping configuration.

This process can be interpreted as a spontaneous symmetry breaking, meaning the system is symmetric, but its behavior is asymmetrical. This idea corroborates with the bistable phenomenon, since the system always looks for minimizing potential energy, and in the bistable sense, it would mean, that the system accumulates energy in one of the modes until a limit is reached and minimizes this energy by switching to the other wake mode.

The double well model can be used to represent this system and, in this case, can be based on the probability distribution of the signal, being defined as [De Paula, 2013]:

$$DWEM = -\ln\{P[u(t)]\}\,. \tag{49}$$

The PDFs for the whole signal and the wake modes are represented in Fig. 4.30. The double-well energy models for *Re* = 1.44x10^4 and 2.32x10^4 are represented in Fig. 4.31, Fig. 4.32, and Fig. 4.33, for *p/D* = 1.26, 1.16, and 1.60 respectively. It can be verified that the wells are not symmetric, neither in large nor in deepness, and it is directly related to the probability of the flow falling in one or the other wake mode.

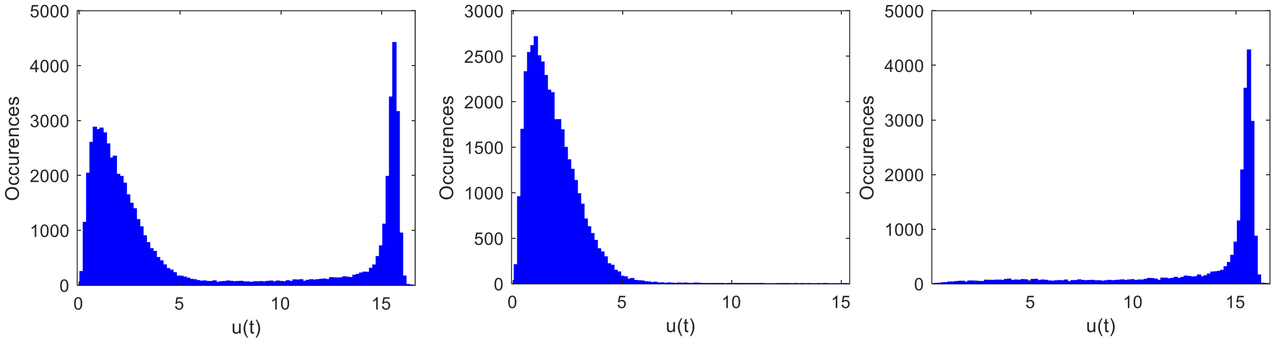

(a) (b) (c)

Figure 4.30 – Probability Density Functions for a) complete bistable time series, b) large wake, c) narrow wake. For *Re* = 1.44x10^4, *p/D* = 1.26.

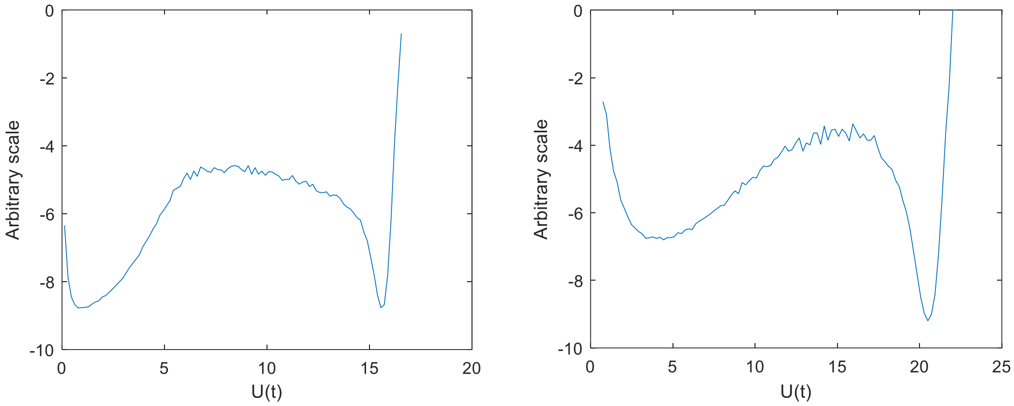

(a) (b)

Figure 4.31– Double well model for a) *Re* = 1.44x10^4 and b) Re = 2.32x10^4. *p/D* = 1.26.

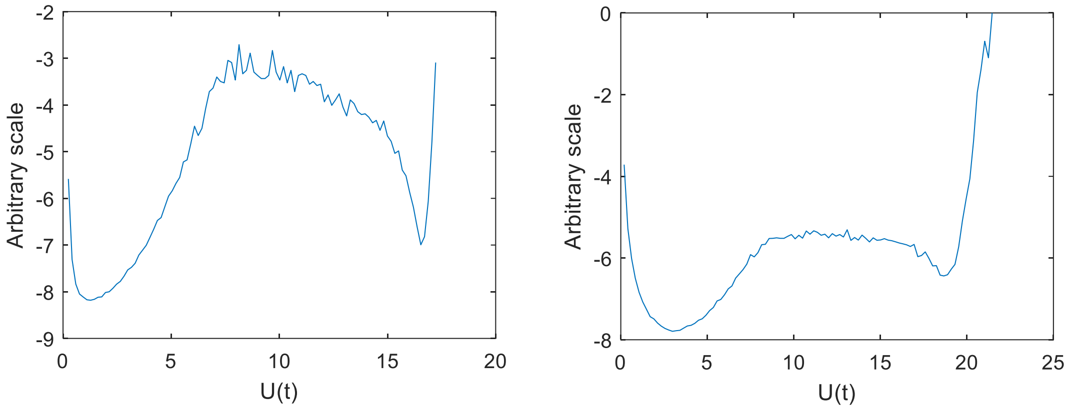

(a) (b)

Figure 4.32 – Double well model for a) *Re* = 1.44x10^4 and b) *Re* = 2.32x10^4. *p/D* = 1.16.

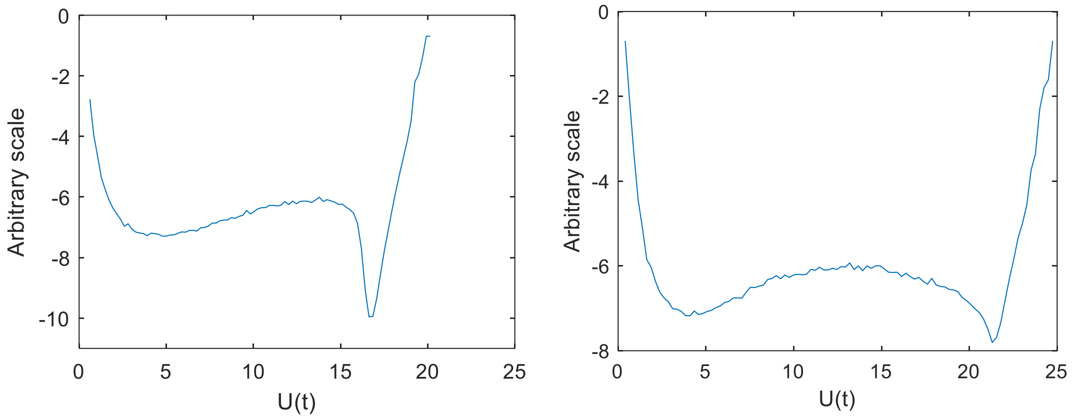

(a) (b)

Figure 4.33 – Double well model for a) *Re* = 1.44x10^4 and b) *Re* = 2.32x10^4. *p/D* = 1.60.

A probability estimation is made, based on the PDFs of the signals, and the cumulative probability for the various Reynolds numbers is plotted in Figure 4.34, Figure 4.35 and Figure 4.36, for *p/D* = 1.26, 1.16, and 1.60 respectively. Despite the chaotic characteristics, the probabilities follow some tendency, and for *p/D* = 1.26, the flow has around 45% of probability of falling in one or the other wake mode. It was not observed for this case, a preferential mode. The transition between two modes corresponds to about 2% to 5 % of the probability.

For *p/D* = 1.16, the probability curves, represented in Figure 4.35 may suffer some direct influence from the time series length. Since the number of mode changes is smaller for this *p/D* ratio, the time series during observation tend to remain longer in one of the wake modes. For the acquired velocity time series, the large wake seems to be the preferred wake mode, even though this assumption cannot be generalized based only on the data sets analyzed.

At *p/D* = 1.60, represented in Figure 4.36, the majority of the cumulative probability curves behave in a very similar tendency. Since the velocity time series behave closer to a flip-flop at this aspect ratio, the curves are more subtle, being almost linear.

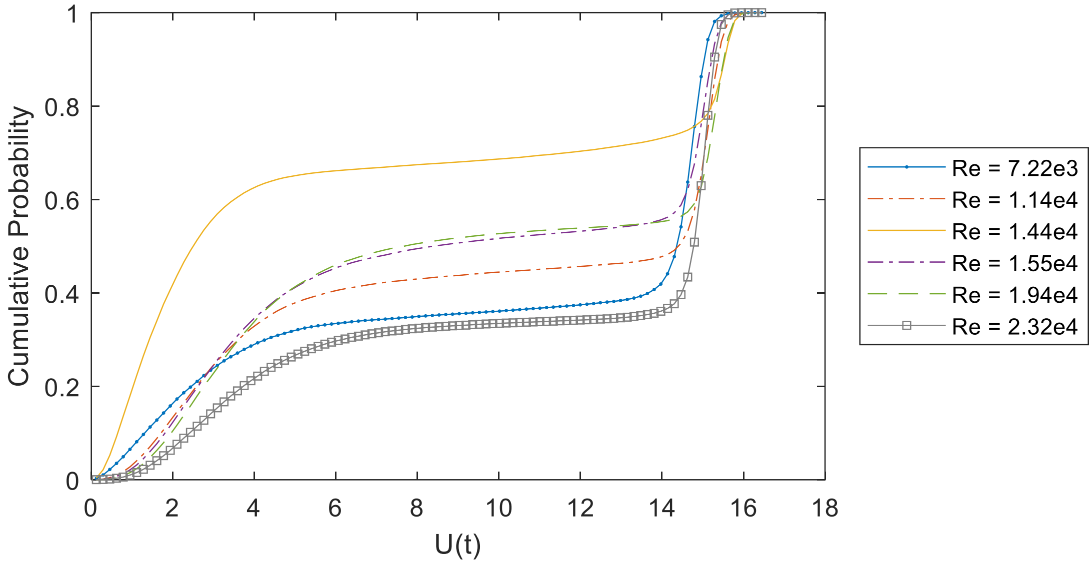

Figure 4.34 – Cumulative Probability for *p/D* = 1.26.

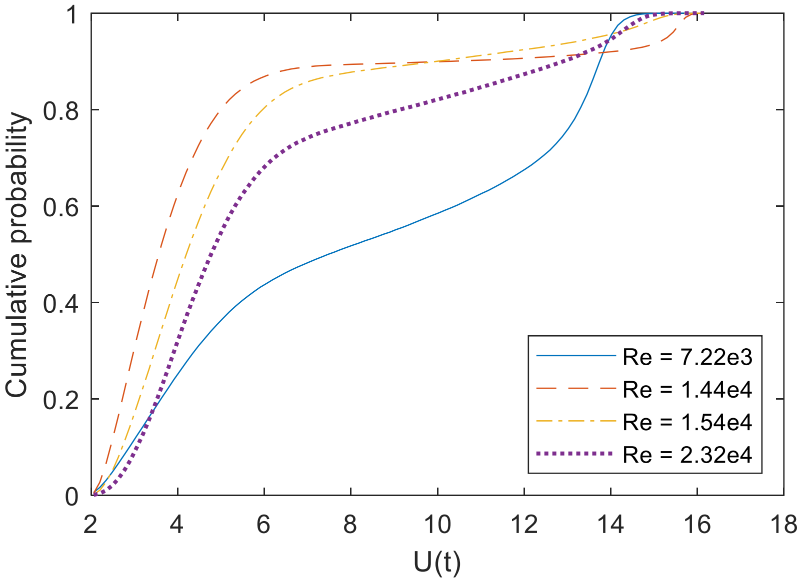

Figure 4.35 – Cumulative Probability for *p/D* = 1.16.

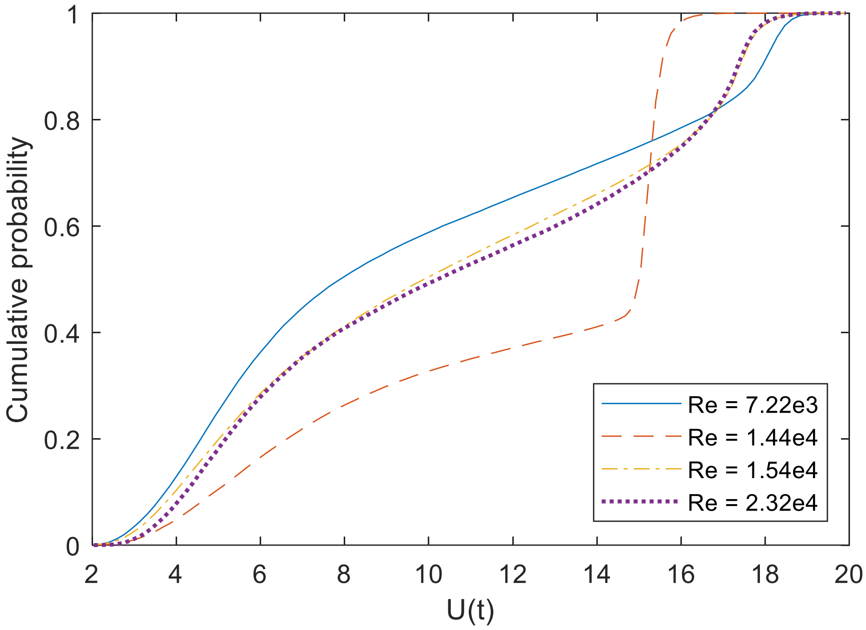

Figure 4.36 – Cumulative Probability for *p/D* = 1.60.

And at last, the two wake modes were analyzed separately. The average ln (divergence) of each wake mode system is represented in Fig. 4.37, Fig. 4.38, and Fig 4.39, for p/D = 1.26, 1.16, and 1.60 respectively. Analyzing the ln (divergence) for each wake separately it is possible to observe some interesting features.

The large wake, in Fig 4.37 a) starts with a negative divergence that grows and became chaotic (values are positive), and then stabilizes around a range of values, for all the embedding dimensions. The narrow wake mode, Fig. 4.37.b), on the other hand, starts with a positive divergence that decreases fast in the first realizations, it also presents very evident oscillations, that would result in a variation between positive and negative Lyapunov exponents. These oscillations could be associated with the narrow wake being more unstable than the large wake, and therefore possessing more dominance on the switching process. The same behavior was verified for the other Reynolds numbers in all *p/D*.

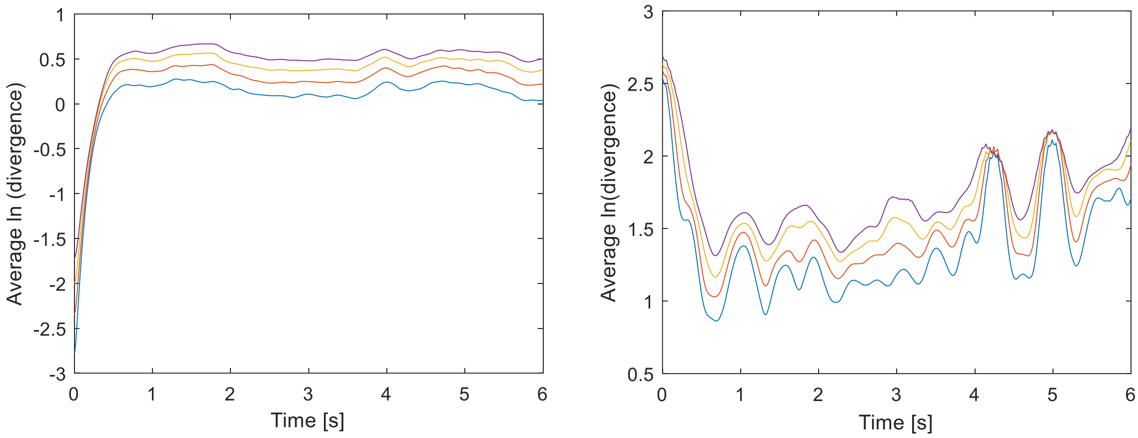

Figure 4.37 – Average ln divergence for a) Large Wake mode and b) Narrow Wake mode. *Re* = 1.44x10^4. *p/D* = 1.26.

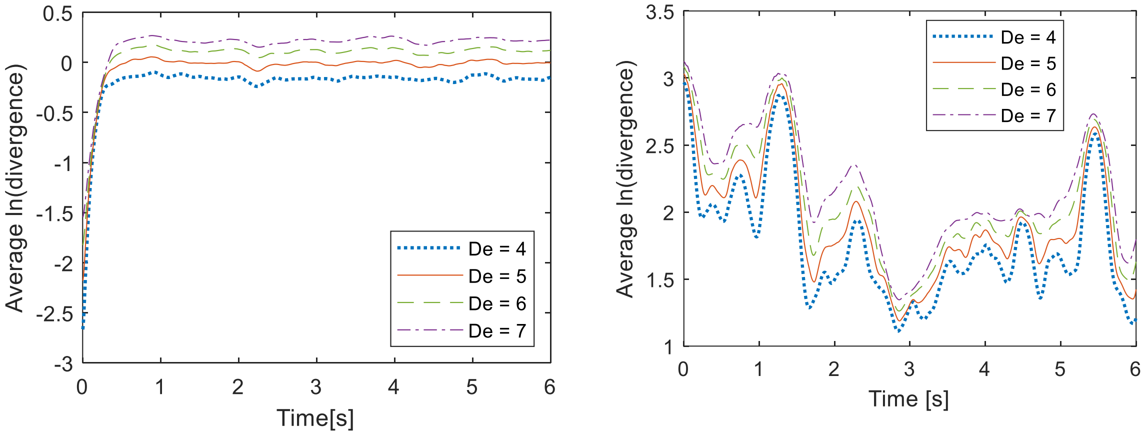

Figure 4.38 – Average ln divergence for a) Large Wake mode and b) Narrow Wake mode. *Re* = 1.44x10^4. *p/D* = 1.16.

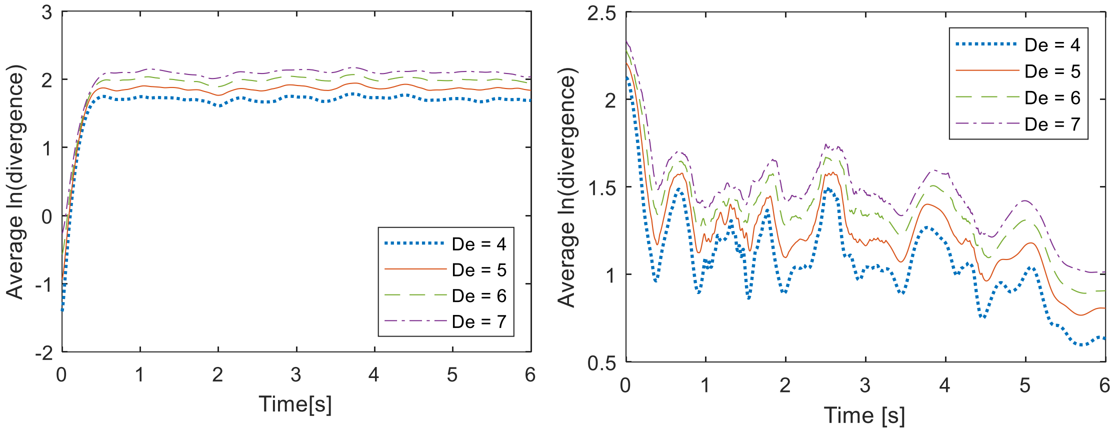

Figure 4.39 – Average ln divergence for a) Large Wake mode and b) Narrow Wake mode. *Re* = 1.44x10^4. *p/D* = 1.60.

A model for reconstructing the bistable flow is proposed. The pseudo-frequency of mode changing for the various Reynolds numbers and *p/D* was calculated according to the definition:

$$f_p = M.C./N \tag{50}$$

were *M.C.* is the number of mode switches that are counted considering a point of reference in the time series (like the mean value for example), and *N* is the number of data points or the length of the signal. The results are presented in Figure 4.40, Figure 4.41, and Figure 4.42 for p/D = 1.26, 1.16, and 1.60 respectively.

This pseudo-frequency is used as one of the parameters for the reconstruction of the general bistable signal. The values of the pseudo-frequency were assumed to behave as a uniform probability distribution and the values used in the reconstruction were selected by Monte Carlo, between the range of 2x10^{-4} and 7x10^{-4}. Using a random pseudo-frequency in the reconstruction made the results more robust and more relatable to the experimental data.

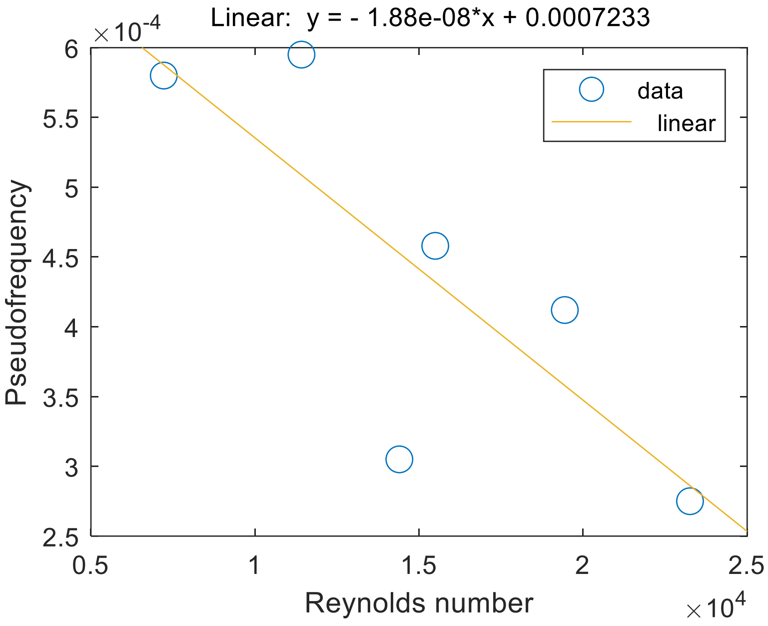

Figure 4.40– Variation of the Pseudo-frequency of mode changing with the Reynolds number for *p/D* = 1.26.

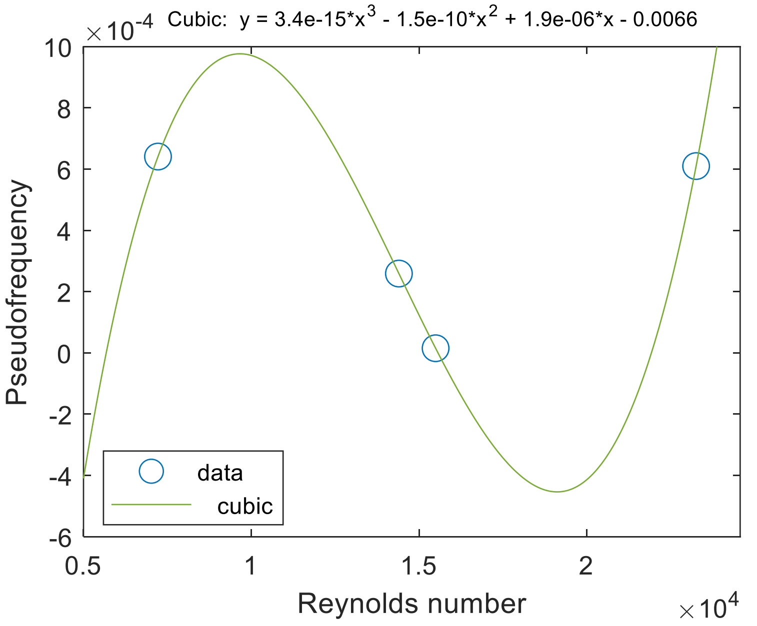

Figure 4.41– Variation of the pseudo-frequency of mode changing with the Reynolds number for *p/D* = 1.16.

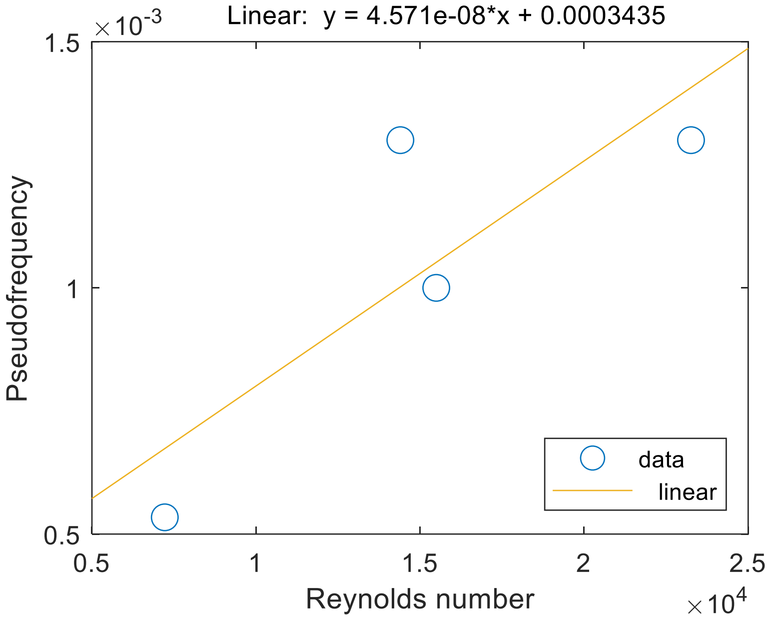

Figure 4.42– Variation of the pseudo-frequency of mode changing with the Reynolds number for *p/D* = 1.60.

The general bistable signals were then reconstructed based on two probability distribution functions: Uniform distribution and Normal distribution, and a third reconstruction was made using the filtered data originated from HHT for *p/D* = 1.26. The general bistable signals resulting from the process are represented in Figure 4.43.

For the reconstruction using the Normal distribution, in Fig 4.43.a), two parameters are necessary: mean (μ) and standard deviation (σ). Those values were chosen based on the statistical analysis made in Section 4.2, and the values used are those typically found for the large and narrow wake in experimental bistable time series, with *p/D* = 1.26. Therefore, for the distribution representing the large wake the values of choice where $\mu \approx 1.9087$ and $\sigma \approx 1.1637$, and for the distribution representing the narrow wake, $\mu \approx 13.7670$ and $\sigma \approx 3.5970$. A negative aspect is that this distribution may create negative points in the data set, due to its symmetric characteristic of distributing the values around a mean. So, if the values are close to zero, as in the case of the large wake, and if the standard deviation is big, some values may become negative.

The reconstruction using a Uniform distribution (Fig. 4.43.b)) consists of a much simple and general representation. The values are defined by an inferior and a superior limit for the distribution. Those values were based on the range of velocity values that occur for the large and narrow wake in the experimental time series. For the large wake, the limits chosen were between 0.5 and 4 m/s, and for the narrow wake 10 and 18 m/s. The interval between the limits is the range of values that comprehend the transition between the wake modes and therefore was ignored.

The HHT reconstruction, represented in Fig. 4.43.c), and previously mentioned in section 4.1, was used as a secondary method, to verify the effectiveness of the HHT method to represent the dynamic of the bistable time series, when compared to other tools.

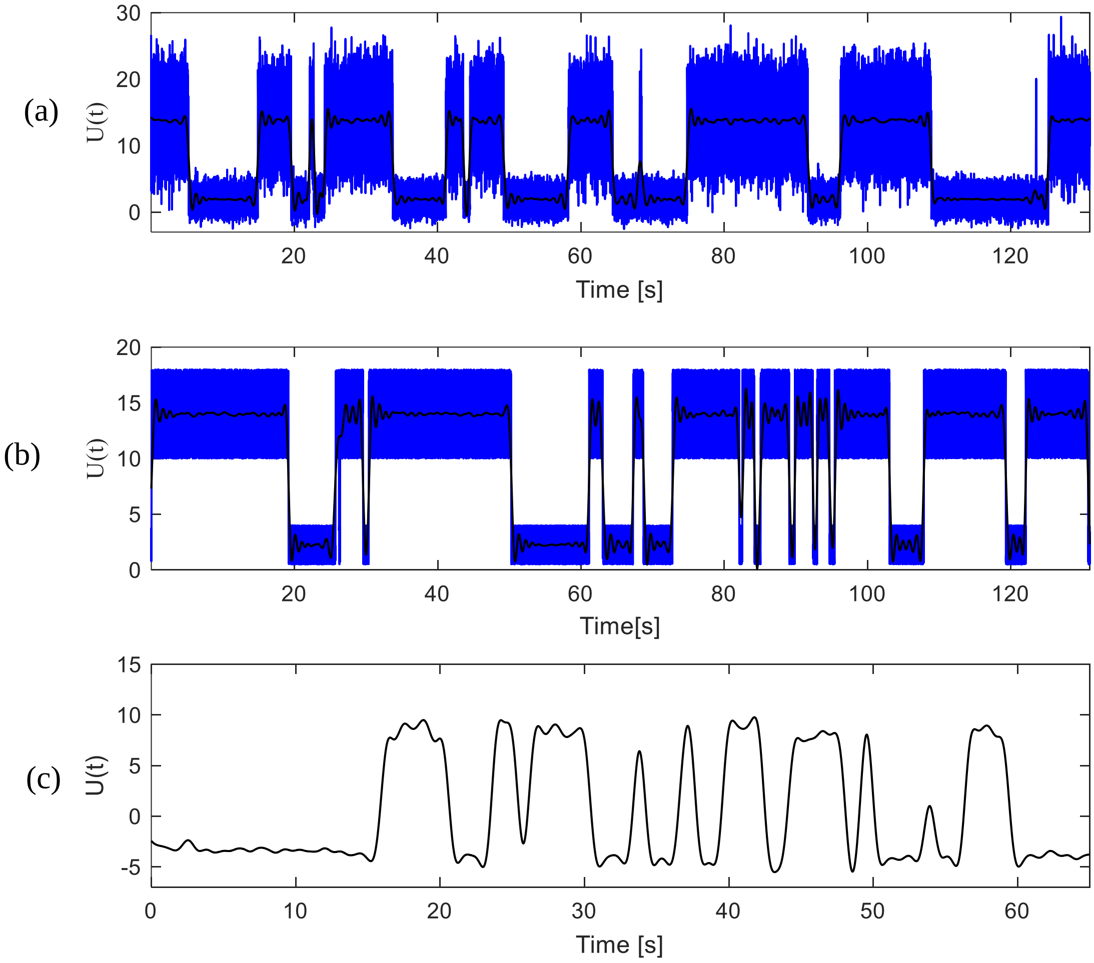

Figure 4.43– Reconstruction of a generic bistable signal using a) Normal distribution, b) Uniform distribution and c) HHT reconstruction from C16 to C11.

The PDFs of the general bistable signals are represented in Figure 4.44.a), Figure 4.44.b) and Figure 4.44.c) for Normal distribution, Uniform distribution, and the HHT reconstruction respectively. As one can see, all the cases capture the essence of the bistable phenomena somehow, with more or less accuracy.

When comparing with a PDF typical of a bistable phenomenon, like the one in Fig. 4.30, it is possible to identify the main differences between the methods. For the case of the

Normal distribution, in Fig 4.44.a), the resulting PDF does represent the signal very well and captures the two wake mode, but, the main differences and problematic aspects would be related to the positive skewness seen in the narrow wake values which are not properly represented.

The uniform distribution, in Fig. 4.44.b) is a general representation of the dynamics; therefore, it represents the general range in which the values may occur for each wake. Since it does not require a mean value or standard deviation, the representation is flat, and the probability is equal for all values. Nevertheless, it would be suitable to represent the dynamic system in a simplified way.

The HHT reconstruction PDF, represented in Fig. 4.44.c) has a most irregular distribution. This is probably because the data set used as a base for the PDF is filtered and possesses only the lower frequency present in the data, therefore, some information may be lost. Also, due to the characteristic of the EMD decomposition, the PDF does not represent properly the range of velocity values of the actual phenomenon.

The strange attractors are reconstructed for the general signals and are represented in 3D, for each case, in Figure 4.45. As it is possible to see, all the attractors are similar and could be said to represent properly the dynamics of the bistable flow and present features seen in an experimental bistable flow.

For the Normal distribution case, Fig. 4.45.a), the attractor seems flatter, meaning, the path between the two basins of attraction has a smaller inclination. The Uniform distribution case, Fig. 4.45.b) seems to be closer in shape, when compared to the strange attractor shown in Figure 4.21 for example. The strange attractor created by the HHT reconstruction, in Fig 4.45.c) is the most different in comparison, presenting some structures that resemble loops, and the path between basins of attraction is not well defined, but in general, the topology is similar to what is expected of a bistable strange attractor.

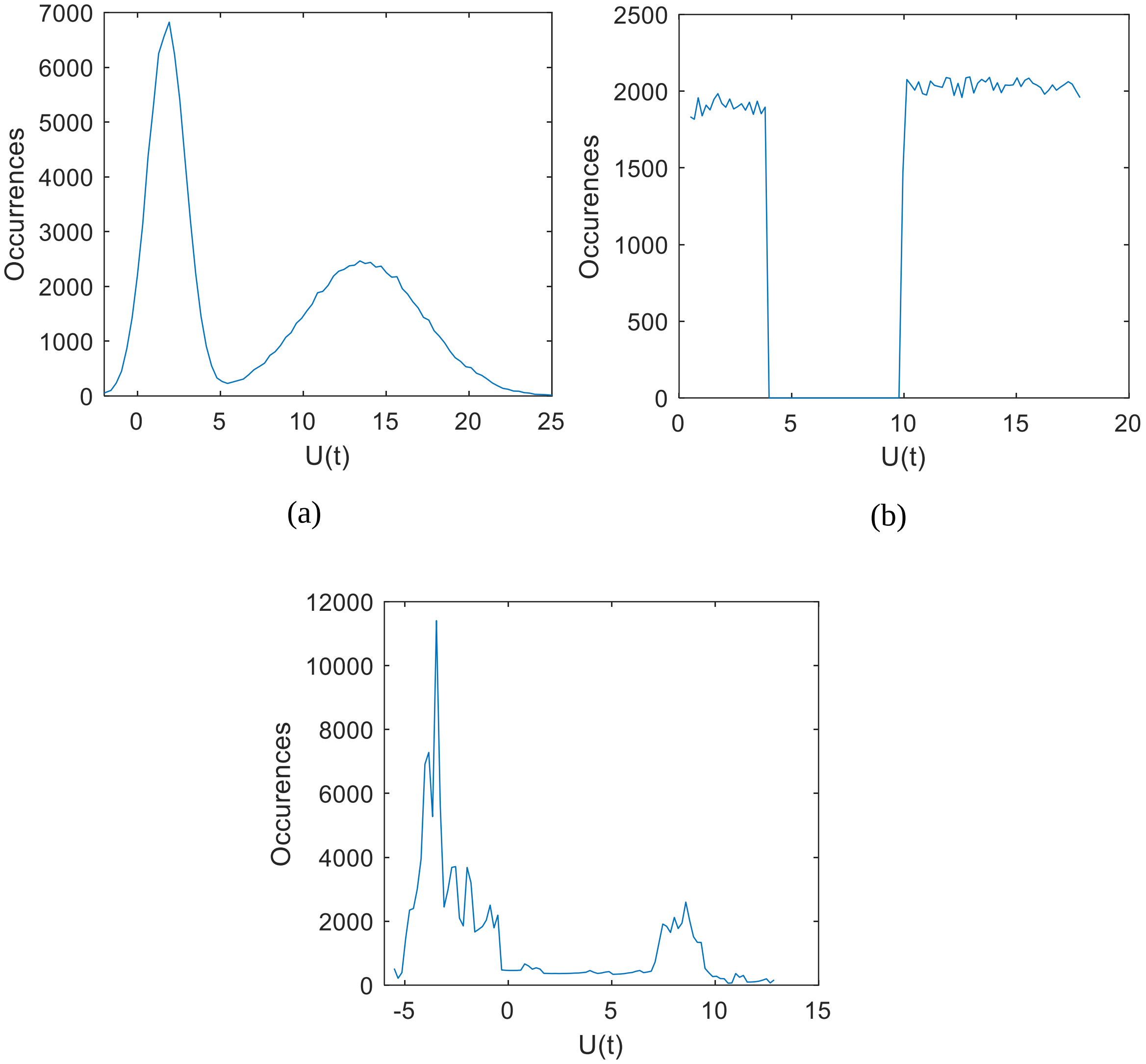

(a)

(b)

(c)

Figure 4.44– Probability density function for a) Normal distribution general bistable signal, b) Uniform distribution general signal and c) HHT reconstruction signal.

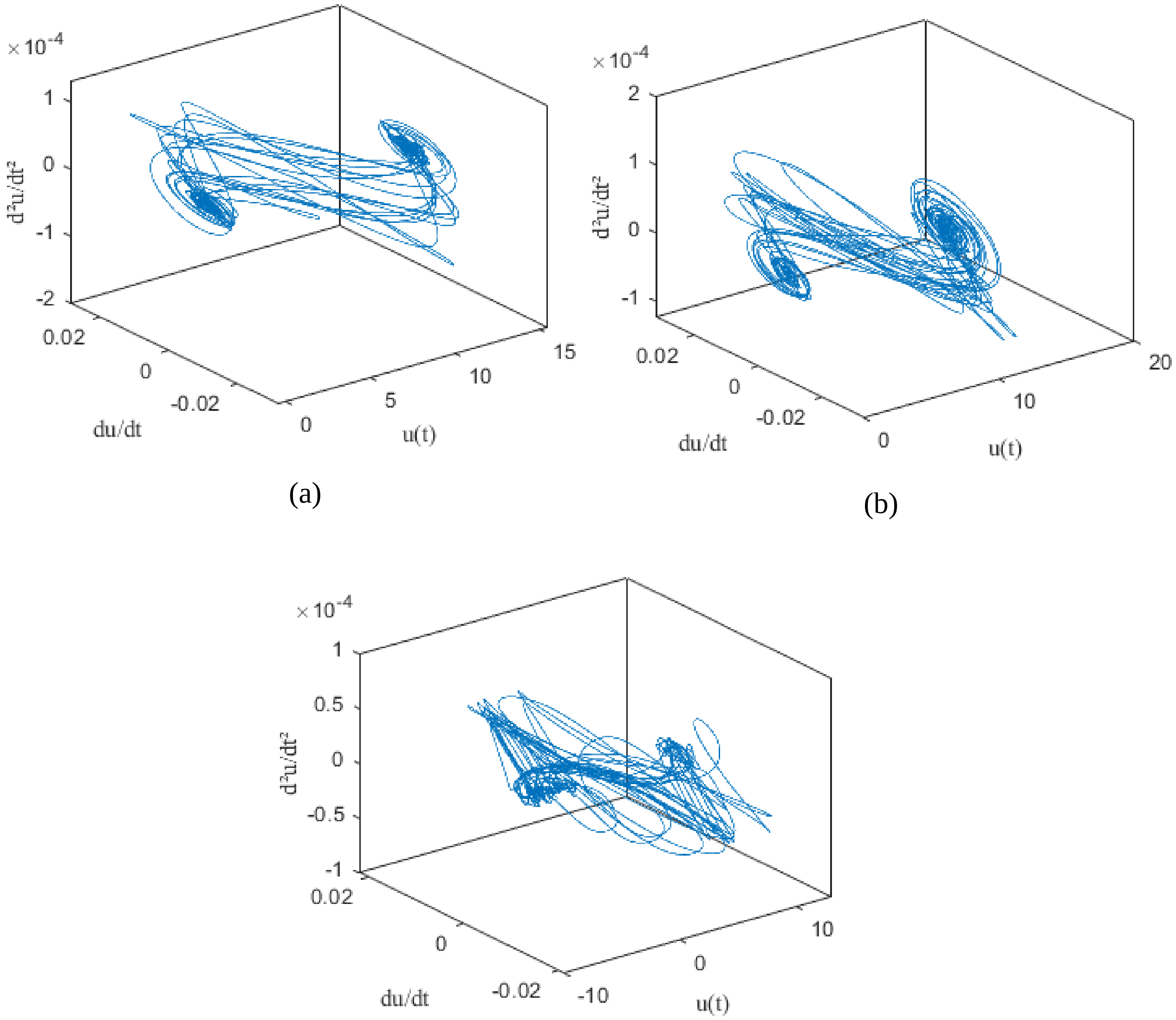

(a)

(b)

(c)

Figure 4.45– 3D strange attractor representation for a) Normal distribution general bistable signal, b) Uniform distribution general bistable signal and c) HHT reconstruction signal.

5 CONCLUDING REMARKS

This work presents a study of the bistable flow after two cylinders side-by-side using tools like Hilbert-Huang transform and statistical methods for signal analysis; and chaos theory for dynamic analysis.

The Hilbert-Huang transform is a combination, in this case, of the ensemble empirical mode decomposition (EEMD) and the Normalized Hilbert Spectral Analysis (NHSA), being a viable tool for non-linear and non-stationary data analysis. The statistical methodology is interesting for identifying patterns in the flow and the chaos theory combines a series of tools to describe the dynamic system, like Lyapunov exponents and fractal dimensions.

The HHT method was previously validated using a single cylinder (see Appendix A for results) as a parameter and extended to a bistable turbulent flow after two cylinders side-by-side. For the bistable flow, two cylinders of D = 25.1 mm were used, with a p/D = 1.16; 1.26 and 1.60, and various Reynolds numbers.

Results demonstrated that the IMFs that present the higher correlation and the most important amount of information in the bistable flow are those of lower frequency (higher IMF number). In the Hilbert spectrum, no specific range of frequency was highlighted, demonstrating that the method may not be so efficient in separating frequencies when they occur simultaneously and with values not far apart, as is the case in bistability. Some energy although could be observed in the lower frequency range, emphasizing that the bistability is a low frequency phenomenon. The power spectra of the IMF components showed that the EEMD decomposition may not separate the flow scales properly in complex flows like the bistable one.

The energy contained in each IMF component was calculated by the Mean Square Energy equation. Results demonstrated that the Reynolds number variation has no direct influence on the most energetic IMF component, and for the same p/D this component could be considered the same for all Reynolds. The aspect ratio p/D on the other hand has a direct influence on the most energetic component, the higher the p/D the lower the IMF component with higher energy. This means that the energy in higher p/D is contained in a smaller flow scale (higher frequency) than for smaller p/D. A similar relationship with Reynolds number and p/D was observed for the IMF correlation coefficient.

The statistical analysis was performed in fragments of eight seconds extracted from the original velocity time series. In this analysis the data was scanned by a window, creating blocks of data points that were converted into PDFs. The four first statistical moments were calculated for each PDF block. Results showed that the statistical moments behaved in a very similar pattern for each p/D. For the standard deviation when the flow was in the large wake mode, the values were higher and oscillated around 0.4 - 0.6. When the flow changed to the narrow wake mode, the values decreased to close to zero, and peaks could be observed in attempts of changing. For skewness, the large wake corresponds to positive values between zero and 2 and the narrow wake presents a negative skewness whose values oscillated between a wider range. At kurtosis was possible to observe that the large wake presented values the oscillated around zero, while the narrow wake presented higher values of kurtosis that varied according to the time the flow remained in this wake mode. It was not possible to establish a unique value for the wake modes statistics, but a range of values could be considered. It was possible to observe that the statistical moments behave following a pattern. No direct influence of the Reynolds number was observed in the statistical values.

Chaos theory was applied as a tool to study the dynamics of the bistable flow. The strange attractors created by the method showed the geometric behavior of the flow and the presence of two basins of attraction that can be associated with each wake mode. Also, the topological analysis of the attractor brought some light to the physics of the bistable phenomenon, demonstrating the influence of acceleration and jerk in the process of mode switching.

The largest Lyapunov exponent was calculated for the bistable flow, and as was already shown in previous works, bistability presents a chaotic behavior, demonstrated by the presence of a positive Lyapunov exponent. The influence of the Reynolds number in the Lyapunov exponent was explored, and the results showed that the Lyapunov exponent tends to increase as the Reynolds number increases. This result demonstrates that the bistable flow becomes more chaotic for higher Reynolds numbers. An analogy with a double-well model was made and the fact that the flow becomes more chaotic with the Reynolds, until the point where the bistability would be lost can be interpreted as a spontaneous symmetry breaking since the system is symmetric, but its behavior is not.

Each wake mode was also analyzed separately using the largest Lyapunov exponent. These results identified that even though both wake modes are chaotic, the narrow wake mode is more unstable since its ln (divergence) oscillates between higher and lower values and is not possible to establish only one Lyapunov exponent. The large wake, on the other hand, presents an ln (divergence) that increases and stabilizes around a value, and a positive Lyapunov exponent can be identified. These results demonstrate that the narrow wake, for its unstable characteristics, might be the dominant wake in the switching processes.

A general bistable model was created using Normal and Uniform probability functions and with the reconstruction created by the lower frequency IMFs from the HHT method. The data sets were sampled using Monte Carlo. The strange attractors of the general signals were reconstructed. Each result showed some particularities and some aspects that diverged from the original dynamics, but in general, all the methods were satisfactory and appropriately reproduced the bistable dynamics.

This work also showed that the bistable phenomenon can be reconstructed using only the lower frequency IMF components, excluding the IMF components that represent the turbulent part of the signal (same effect obtained by using DWT), and yet be well represented. The fact that the dissipative part can be removed, but bistability is still well characterized, leads to understand that bistability is not a dissipative phenomenon itself, and the dissipative part comes from the turbulence, which is alike for all turbulent flows. This is also corroborated by the interpretation that the bistability is a temporal-symmetric phenomenon, and if it was dissipative this symmetry would be broken.

6 REFERÊNCIAS BIBLIOGRÁFICAS

ABBATE, A.; DECUSATIS, C. M.; DAS, P. K. Time-Frequency Analysis of Signals. **Wavelets and Subbands**, Applied and Numerical Harmonic Analysis. p.103–187, 2002. Birkhäuser, Boston, MA.

ABARBANEL, H. D. I.; BROWN, R.; SIDOROWICH, J. J.; TSIMRING, L. SH. The analysis of observed chaotic data in physical systems. **Reviews of Modern Physics**, v. 65, n. 4, p. 1331–1392, 1993. American Physical Society.

ACHENBACH, E. Distribution of local pressure and skin friction around a circular cylinder in cross-flow up to Re = 5×10^6. **Journal of Fluid Mechanics**, v. 34, n. 4, p. 625–639, 1968.

ADACHI, T.; MATSUUCHI, K.; MATSUDA, S.; KAWAI, T. On the Force and Vortex Shedding on a Circular Cylinder from Subcritical up to Transcritical Reynolds Numbers. **Bulletin of JSME**, v. 28, n. 243, p. 1906–1909, 1985.

AKAR, M. A.; OGUZ, B.; AKILLI, H.; SAHIN, B. Flow behavior downstream of two side-by-side circular cylinders in shallow water. **Canadian Journal of Physics**, v. 94, n. 10, p. 975–981, 2016.

ALAM, M. M.; MEYER, J. P. Global aerodynamic instability of twin cylinders in cross flow. , 2013. Elsevier.

ALAM, M. M.; MORIYA, M.; SAKAMOTO, H. Aerodynamic characteristics of two side-by-side circular cylinders and application of wavelet analysis on the switching phenomenon. **Journal of Fluids and Structures**, Bluff-body/Flow interactions., v. 18, n. 3–4, p. 325–346, 2003.

ALAM, M. M.; ZHOU, Y. Flow around two side-by-side closely spaced circular cylinders. **Journal of Fluids and Structures**, v. 23, n. 5, p. 799–805, 2007.

ANTONIA, R. A.; BROWNE, L. W. B.; FULACHIER, L. Average wavelength of organized structures in the turbulent far wake of a cylinder. **Experiments in Fluids**, v. 5, n. 5, p. 298–304, 1987.

BATHAM, J. P. Pressure distributions on circular cylinders at critical Reynolds numbers. **Journal of Fluid Mechanics**, v. 57, n. 2, p. 209–228, 1973.

BATTISTA, B.; KNAPP, C.; MCGEE, T.; GOEBEL, V. Application of the empirical mode decomposition and Hilbert-Huang transform to seismic reflection data. **GEOPHYSICS**, v. 72, n. 2, p. H29–H37, 2007.

BEARMAN, P. W. On vortex shedding from a circular cylinder in the critical Reynolds number regime. **Journal of Fluid Mechanics**, v. 37, p. 577–585, 1969.

BEARMAN, P. W.; WADCOCK, A. J. The interaction between a pair of circular cylinders normal to a stream. **Journal of Fluid Mechanics**, v. 61, n. 03, p. 499–511, 1973.

BEDROSIAN, E. A product theorem for Hilbert transforms. **Proceedings of the IEEE**, v. 51, n. 5, p. 868–869, 1963.

BÉNARD, H., 1908-a, Formation périodique de centres de giration à l’arrière d’un obstacle en mouvement, **C.R. Acad. Sci**. 147, 839–842.

BÉNARD, H., 1908-b, Etude cinématographique des ramous et des rides produits par la translation d’un obstacle, **C.R. Acad. Sci**. 147, 970–972

BENDAT, J. S.; PIERSOL, A. G. **Random Data: Analysis and Measurement Procedures**. 4th ed. New York: Wiley, 2010.

BIERMANN, D.; HERRNSTEIN, W. H. The Interference Between Struts in Various Combinations., 1934. Report from National Advisory Committee for Aeronautics - Langley Memorial Aeronautical Laboratory.

BISHOP, R. E. D.; HASSAN, A. Y. The lift and drag forces on a circular cylinder in a flowing fluid. **Proc. R. Soc. Lond. A**, v. 277, n. 1368, p. 32–50, 1964.

BLEVINS, R. D. **Flow-induced vibration**. 2^{a} ed. Van Nostrand Reinhold, New York, 1990.

BLOOR, M. S.; GERRARD, J. H. Measurements on turbulent vortices in a cylinder wake. **Proc. R. Soc. Lond. A**, v. 294, n. 1438, p. 319–342, 1966.

BOZHKOV, V. M.; VASIL’EV, L. E.; ZHIGULEV, S. V. Transverse subsonic flow past a cylinder. **Fluid Dynamics**, v. 15, n. 2, p. 303–306, 1980.

CAPONE, A.; KLEIN, C.; DI FELICE, F.; MIOZZI, M. Phenomenology of a flow around a circular cylinder at sub-critical and critical Reynolds numbers. **Physics of Fluids**, v. 28, n. 7, p. 074101, 2016.

CARINI, M.; GIANNETTI, F.; AUTERI, F. On the origin of the flip-flop instability of two side-by-side cylinder wakes. **J. Fluid Mech**., v. 742, p. 552–576, 2014.

CHARRU, F. **Hydrodynamic Instabilities**. Cambridge: Cambridge University Press, 2011.

CHATTERJEE, D.; BISWAS, G. Dynamic behavior of flow around rows of square cylinders kept in staggered arrangement. **Journal of Wind Engineering and Industrial Aerodynamics**, v. 136, p. 1–11, 2015.

COHEN, L. **Time-frequency Analysis: Theory and Applications**. Upper Saddle River, NJ, USA: Prentice-Hall, Inc., 1995.

COUTANCEAU, M.; DEFAYE, J.-R. Circular Cylinder Wake Configurations: A Flow Visualization Survey. **Applied Mechanics Reviews**, v. 44, n. 6, p. 255–305, 1991.

DÄTIG, M.; SCHLURMANN, T. Performance and limitations of the Hilbert–Huang transformation (HHT) with an application to irregular water waves. **Ocean Engineering**, v. 31, n. 14–15, p. 1783–1834, 2004.

DAUBECHIES, I. **Ten Lectures on Wavelets**. Philadelphia: SIAM-Society for Industrial and Applied Mathematics, 1992.

DIKS, C. **Nonlinear Time Series Analysis: Methods And Applications**. Singapore: World Scientific Press, 1999.

DJERIDI, H.; BRAZA, M.; PERRIN, R.; et al. Near-Wake Turbulence Properties around a Circular Cylinder at High Reynolds Number. **Flow, Turbulence and Combustion**, v. 71, n. 1–4, p. 19–34, 2003.

DRYDEN, H. L.; HILL, G. C. Wind pressure on circular cylinders and chimneys. **Bureau of Standards Journal of Research**, v. 5, n. 3, p. 653, 1930.

DUMAN, F.; ÖZDEMIR, N.; YILDIRIM, E. Patient specific seizure prediction algorithm using Hilbert-Huang Transform. Proceedings of 2012 IEEE-EMBS International Conference on Biomedical and Health Informatics. **Anais**. p.705–708, 2012.

ECKMANN, J.-P.; RUELLE, D. Fundamental limitations for estimating dimensions and Lyapunov exponents in dynamical systems. **Physical D: Nonlinear Phenomena**, v. 56, n. 2, p. 185–187, 1992.

FAGE, A.; FALKNER, V. M. **Further experiments on the flow around a circular cylinder**. London: H.M.S.O., 1931.

FARGE, M. Wavelet transforms and their applications to turbulence. **Annual Review of Fluid Mechanics**, v. 24, n. 1, p. 395–458, 1992.

FELDMAN, M. Hilbert transform in vibration analysis. **Mechanical Systems and Signal Processing**, v. 25, n. 3, p. 735–802, 2011.

FERNÁNDEZ-MARTÍNEZ, M.; SÁNCHEZ-GRANERO, M. A. Fractal dimension for fractal structures: A Hausdorff approach revisited. **Journal of Mathematical Analysis and Applications**, v. 409, n. 1, p. 321–330, 2014.

FERNÁNDEZ-MARTÍNEZ, M.; SÁNCHEZ-GRANERO, M. A. How to calculate the Hausdorff dimension using fractal structures. **Applied Mathematics and Computation**, v. 264, p. 116–131, 2015.

FLANDRIN, P. **Time-Frequency/Time-Scale Analysis**. Academic Press, 1999a.

FLANDRIN, P. (ORG.). Chapter 1 The time-frequency problem. **Wavelet Analysis and Its Applications**, Time-Frequency/Time-Scale Analysis. v. 10, p.9–47, 1999b. Academic Press.

FLANDRIN, P. Empirical Mode Decomposition. Disponível em: <http://perso.ens-lyon.fr/patrick.flandrin/emd.html>. Acesso em: 23/1/2019.

FLANDRIN, P.; RILLING, G.; GONCALVES, P. Empirical mode decomposition as a filter bank. **IEEE Signal Processing Letters**, v. 11, n. 2, p. 112–114, 2004.

FOUCHER, F.; RAVIER, P. Determination of turbulence properties by using empirical mode decomposition on periodic and random perturbed flows. **Experiments in Fluids**, v. 49, p. 379–390, 2010.

FRANZINI, G. R.; GONÇALVES, R. T.; PESCE, C. P.; et al. Vortex-induced vibration experiments with a long semi-immersed flexible cylinder under tension modulation: Fourier transform and Hilbert–Huang spectral analyses. **Journal of the Brazilian Society of Mechanical Sciences and Engineering**, v. 37, n. 2, p. 589–599, 2015.

GAVILÁN MORENO, C. J. Analysis and simulation of the flow signal in the recirculation loop of a nuclear power station during a bistable flow event. **Nuclear Engineering and Design**, v. 238, n. 10, p. 2754–2760, 2008.

GRASSBERGER, P.; PROCACCIA, I. Characterization of Strange Attractors. **Physical Review Letters**, v. 50, n. 5, p. 346–349, 1983. American Physical Society.

GRASSBERGER, P.; PROCACCIA, I. Measuring the Strangeness of Strange Attractors. In: B. R. Hunt; T.-Y. Li; J. A. Kennedy; H. E. Nusse (Orgs.); **The Theory of Chaotic Attractors**. p.170–189, 2004. New York, NY: Springer.

GREENSIDE, H. S.; WOLF, A.; SWIFT, J.; PIGNATARO, T. Impracticality of a box-counting algorithm for calculating the dimensionality of strange attractors. **Physical Review A.**, v. 25, n. 6, p. 3453–3456, 1982. American Physical Society.

GUCKENHEIMER, J. Noise in chaotic systems. **Nature**, v. 298, n. 5872, p. 358–361, 1982. Nature Publishing Group.

GUCKENHEIMER, J. Strange Attractors in Fluids: Another View. **Annual Review of Fluid Mechanics**, v. 18, n. 1, p. 15–29, 1986.

GUILLAUME, D. W.; LARUE, J. C. Investigation of the flopping regime with two-, three- and four-cylinder arrays. **Experiments in Fluids**, v. 27, p. 145–156, 1999.

HABOWSKI, P. B.; DE PAULA, A. V.; MÖLLER, S. V. Wake behavior analysis for two circular cylinders placed at several angles to the flow. **Journal of the Brazilian Society of Mechanical Sciences and Engineering**, v. 42, n. 8, p. 441, 2020.

HAHN, S. L. **Hilbert Transforms in Signal Processing**. Boston: Artech House, 1996.

HÉNON, M. A Two-dimensional Mapping with a Strange Attractor. In: B. R. Hunt; T.-Y. Li; J. A. Kennedy; H. E. Nusse (Orgs.); **The Theory of Chaotic Attractors**. p.94–102, 2004. New York, NY: Springer.

HOLMES, P. J.; MOON, F. C. Strange Attractors and Chaos in Nonlinear Mechanics. **Journal of Applied Mechanics**, v. 50, n. 4b, p. 1021–1032, 1983.

HORSZCZARUK, R. S. S.; MÖLLER, S. V. Analysis of bistability phenomenon of the flow on two circular cylinders side-by-side with hilbert-huang transform method. **22nd International Congress of Mechanical Engineering (COBEM 2013)**, 2013.

HUANG, N. E. Computing Instantaneous Frequency by normalizing Hilbert Transform. 2005. NASA Patent 10/615,365; Washington, DC.

HUANG, N. E. **Hilbert-Huang Transform and Its Applications**. World Scientific, 2014.

HUANG, N. E.; SHEN, S. S. **Hilbert-Huang Transform and Its Applications**. World Scientific, 2005.

HUANG, N. E.; SHEN, Z.; LONG, S. R.; et al. The empirical mode decomposition and the Hilbert spectrum for nonlinear and non-stationary time series analysis. **Proceedings of the Royal Society of London: Mathematical, Physical and Engineering Sciences**, v. 454, n. 1971, p. 903–995, 1998.

HUANG, N. E.; SHEN, Z.; LONG, S. R. A NEW VIEW OF NONLINEAR WATER WAVES: The Hilbert Spectrum. **Annual Review of Fluid Mechanics**, v. 31, n. 1, p. 417–457, 1999.

HUANG, N. E.; WU, M.-L. C.; LONG, S. R.; et al. A confidence limit for the empirical mode decomposition and Hilbert spectral analysis. **Proceedings of the Royal Society of London A: Mathematical, Physical and Engineering Sciences**, v. 459, n. 2037, p. 2317–2345, 2003.

HUANG, N. E.; WU, M.-L.; QU, W.; LONG, S. R.; SHEN, S. S. P. Applications of Hilbert–Huang transform to non-stationary financial time series analysis. **Applied Stochastic Models in Business and Industry**, v. 19, n. 3, p. 245–268, 2003.

HUANG, N. E.; WU, Z. A review on Hilbert-Huang transform: Method and its applications to geophysical studies. **Reviews of Geophysics**, v. 46, n. 2, p. RG2006, 2008.

HUANG, N. E.; WU, Z.; LONG, S. R.; et al. On instantaneous frequency. **Advances in Adaptive Data Analysis**, v. 01, n. 02, p. 177–229, 2009.

HUANG, X.; HUANG, L.; JUNG, T.-P.; CHENG, C.-K.; MANDELL, A. J. Intrinsic mode functions locate implicit turbulent attractors in time in frontal lobe MEG recordings. **Neuroscience**, v. 267, p. 91–101, 2014.

HUANG, Y. X.; SCHMITT, F. G.; GAGNE, Y. Two-scale correlation and energy cascade in three-dimensional turbulent flows. **Journal of Statistical Mechanics: Theory and Experiment**, v. 2014, n. 5, p. P05002, 2014.

HUANG, Y. X.; SCHMITT, F. G.; LU, Z. M.; LIU, Y. L. An amplitude-frequency study of turbulent scaling intermittency using Empirical Mode Decomposition and Hilbert Spectral Analysis. **EPL (Europhysics Letters)**, v. 84, n. 4, p. 40010, 2008.

HUANG, Y. X.; SCHMITT, F.; LU, Z.; LIU, Y. Analysis of Experimental Homogeneous Turbulence Time Series by Hilbert−Huang Transform. 18 ème Congrès Français de Mécanique. **Anais...** , 2007. Grenoble.

HUANG, Z.; CHEN, Y.; PAN, M. Time-frequency characterization of atrial fibrillation from surface ECG based on Hilbert-Huang transform. **Journal of Medical Engineering & Technology**, v. 31, n. 5, p. 381–389, 2007.

INDRUSIAK, M. L. S. **Caracterização de Escoamentos Turbulentos Transientes usando a Transformada de ondaletas**, 2004. Doutorado, Porto Alegre: Universidade Federal do Rio Grande do Sul.

INDRUSIAK, M. L. S.; GOULART, J. V.; OLINTO, C. R.; MÖLLER, S. V. Wavelet time–frequency analysis of accelerating and decelerating flows in a tube bank. **Nuclear Engineering and Design**, v. 235, p. 1875–1887, 2005.

INDRUSIAK, M. L. S.; KOZAKEVICIUS, A. J.; MÖLLER, S. V. Wavelet analysis considerations for experimental nonstationary flow phenomena. **Thermal Engineering**, v. 15, n. 1, p. 10, 2016.

INDRUSIAK, M. L. S.; MÖLLER, S. V. Wavelet analysis of unsteady flows: Application on the determination of the Strouhal number of the transient wake behind a single cylinder. **Experimental Thermal and Fluid Science**, v. 35, n. 2, p. 319–327, 2011.

KANTZ, H.; SCHREIBER, T. **Nonlinear Time Series Analysis**. 2 edition ed. Cambridge, UK ; New York: Cambridge University Press, 2004.

KAPLAN, J. L.; YORKE, J. A. Chaotic behavior of multidimensional difference equations. In: H.-O. Peitgen; H.-O. Walther (Orgs.); Functional Differential Equations and Approximation of Fixed Points. **Anais**... , Lecture Notes in Mathematics. p.204–227, 1979. Berlin, Heidelberg: Springer.

KENNEL, M. B.; BROWN, R.; ABARBANEL, H. D. I. Determining embedding dimension for phase-space reconstruction using a geometrical construction. **Physical Review A**, v. 45, n. 6, p. 3403–3411, 1992. American Physical Society.

KEOGH, D. B.; MESKELL, C. BI-STABLE FLOW IN PARALLEL TRIANGULAR TUBE ARRAYS WITH A PITCH-TO-DIAMETER RATIO OF 1.375. **Nuclear Engineering and Design**, v. 285, 2014.

KIM, H. J.; DURBIN, P. A. Investigation of the flow between a pair of circular cylinders in the flopping regime. **Journal of Fluid Mechanics**, v. 196, p. 431–448, 1988.

KIM, S.; ALAM, M. M. Characteristics and suppression of flow-induced vibrations of two side-by-side circular cylinders. **Journal of Fluids and Structures**, v. 54, p. 629–642, 2015.

LANDAU, L. D.; LIFSHITZ, E. M. **Fluid Mechanics: Landau and Lifshitz: Course of Theoretical Physics**, Volume 6. 2º ed. Pergamon, 1987.

LANFORD, O. E., III. The strange attractor theory of turbulence. **Annual Review of Fluid Mechanics**, v. 14, p. 347–364, 1982.

LEGUA, M.; SÁNCHEZ-RUIZ, L. M. Cauchy Principal Value Contour Integral with Applications. **Entropy**, v. 19, n. 5, p. 215, 2017.

LI, H.; YANG, L.; HUANG, D. The study of the intermittency test filtering character of Hilbert–Huang transform. **Mathematics and Computers in Simulation**, v. 70, n. 1, p. 22–32, 2005.

LIU, B.; JAIMAN, R. K. Dynamics of gap flow interference in a vibrating side-by-side arrangement of two circular cylinders at moderate Reynolds number. arXiv:1801.05109 [physics], 2018.

LO, M.-T.; TSAI, P.-H.; LIN, P.-F.; LIN, C.; HSIN, Y. L. The nonlinear and nonstationary properties in eeg signals: probing the complex fluctuations by hilbert–huang transform. **Advances in Adaptive Data Analysis**, v. 01, n. 03, p. 461–482, 2009.

LORENZ, E. N. Deterministic Nonperiodic Flow. **Journal of the Atmospheric Sciences**, v. 20, n. 2, p. 130–141, 1963.

MAZELLIER, N.; FOUCHER, F. Separation between coherent and turbulent fluctuations: what can we learn from the empirical mode decomposition? **Experiments in Fluids**, v. 51, n. 2, p. 527–541, 2011.

MCDONOUGH, J.; BYWATER, R.; BUELL, J. An investigation of strange attractor theory and small-scale turbulence. **17th Fluid Dynamics, Plasma Dynamics, and Lasers Conference**, 1984. Colorado: American Institute of Aeronautics and Astronautics.

MEDINA, O. D.; SCHMITT, F. G.; CALIF, R. Multi-scale correlations between synchronized power and wind measurements: a way to characterize turbulent effect in a scale invariant way. p.3, 2015. Paris.

MENEGHINI, J. R.; ÁSSI, G. R. S.; ORSELLI, R. M.; et al. Ruido e Vibrações Induzidos por Vórtices. **Turbulência**, ABCM. v. 7, p.259–324, 2010. Rio de Janeiro.

MENG, H.; LIU, Z.; YU, Y.; WU, J. Time-frequency analysis of Hilbert spectrum of pressure fluctuation time series in a Kenics Static Mixer based on empirical mode decomposition. **Brazilian Journal of Chemical Engineering**, v. 29, n. 1, p. 167–182, 2012.

MIAU, J. J.; HU, C. C.; TU, J. K. Hilbert and Wavelet analyses of unsteady, three-dimensional characteristics of vortex shedding from a circular cylinder. **Journal of the Chinese Society of Mechanical Engineers, Transactions of the Chinese Institute of Engineers, Series C/Chung-Kuo Chi Hsueh Kung Ch’eng Hsuebo Pao**, v. 28, n. 1, p. 99–109, 2007.

MIAU, J. J.; TSAI, H. W.; LIN, Y. J.; et al. Experiment on smooth, circular cylinders in cross-flow in the critical Reynolds number regime. **Experiments in Fluids**, v. 51, n. 4, p. 949–967, 2011.

MIAU, J.-J.; TU, J. K.; LIAO, T. W. Insights into Vortex Shedding with Data Analysis. **Journal of Fluid Science and Technology**, v. 4, n. 2, p. 415–429, 2009.

MÖLLER, S. V.; SILVESTRINI, J. H. Turbulência. **Turbulência: Fundamentos.**, Coleção de Cadernos de Turbulência. v. 4, p.1–32, 2004. ABCM. Rio de Janeiro.

NEUMEISTER, R. F.; PETRY, A. P.; MÖLLER, S. V. Characteristics of the wake formation and force distribution of the bistable flow on two cylinders side-by-side. **Journal of the Brazilian Society of Mechanical Sciences and Engineering**, v. 40, n. 12, p. 564, 2018.

NG, C. W.; CHENG, V. S. Y.; KO, N. W. M. Numerical study of vortex interactions behind two circular cylinders in bistable flow regime. **Fluid Dynamics Research**, v. 19, n. 6, p. 379–409, 1997.

NIEMANN, H.-J.; HÖLSCHER, N. A review of recent experiments on the flow past circular cylinders. **Journal of Wind Engineering and Industrial Aerodynamics**, v. 33, n. 1, p. 197–209, 1990.

NOVAK, M., 1969. Aeroelastic galloping of prismatic bodies. **ASCE Journal of the Engineering Mechanics**. Division 96, 115–142

NOVAK, M., 1972. Galloping oscillations of prismatic structures. **ASCE Journal of the Engineering Mechanics**. Division 98, 27–46

NUTTALL, A. H.; BEDROSIAN, E. On the quadrature approximation to the Hilbert transform of modulated signals. **Proceedings of the IEEE**, v. 54, n. 10, p. 1458–1459, 1966.

OLINTO, C. R. **Estudo experimental das características do escoamento turbulento nas primeiras fileiras de bancos de tubos**, 2005.

ONG, L.; WALLACE, J. The velocity field of the turbulent very near wake of a circular cylinder. **Experiments in Fluids**, v. 20, n. 6, p. 441–453, 1996.

OTT, E. Strange attractors and chaotic motions of dynamical systems. **Reviews of Modern Physics**, v. 53, n. 4, p. 655–671, 1981. American Physical Society.

PACKARD, N. H.; CRUTCHFIELD, J. P.; FARMER, J. D.; SHAW, R. S. Geometry from a Time Series. **Physical Review Letters**, v. 45, n. 9, p. 712–716, 1980. American Physical Society.

PAÏDOUSSIS, M. P.; PRICE, S. J.; LANGRE, E. DE. **Fluid-Structure Interactions: Cross-Flow-Induced Instabilities**. Cambridge University Press, 2010.

PARKINSON, G., SMITH J., 1964. The square cylinder as an aeroelastic non-linear oscillator **Quarterly Journal of Mechanics and Applied Mathematics** 17, 225–239

DE PAULA, A. V. **Determinação de Parâmetros que Caracterizam o fenômeno da biestabilidade em escoamentos turbulentos.**, 2013. Doutorado, Porto Alegre: Universidade Federal do Rio Grande do Sul.

DE PAULA, A. V.; MÖLLER, S. V. Finite mixture model applied in the analysis of a turbulent bistable flow on two parallel circular cylinders. **Nuclear Engineering and Design**, SI:NURETH-14., v. 264, p. 203–213, 2013.

DE PAULA, A. V.; MÖLLER, S. V. On the chaotic nature of bistable flows. **Experimental Thermal and Fluid Science**, v. 94, p. 172–191, 2018.

PENG, Z. K.; TSE, P. W.; CHU, F. L. An improved Hilbert–Huang transform and its application in vibration signal analysis. **Journal of Sound and Vibration**, v. 286, n. 1–2, p. 187–205, 2005.

PESCE, C. P.; FUJARRA, A. L. C.; KUBOTA, L. K. The Hilbert-Huang Spectral Analysis Method Applied to VIV. Proceedings of OMAE2006 25th International Conference on

Offshore Mechanics and Arctic Engineering. **Anais...** . p.551–561, 2006. Hamburg, Germany.

PESCHARD, I.; LE GAL, P. Coupled Wakes of Cylinders. **Physical Review Letters**, v. 77, n. 15, p. 3122–3125, 1996.

PHILLIPS, S. C.; GLEDHILL, R. J.; ESSEX, J. W.; EDGE, C. M. Application of the Hilbert−Huang Transform to the Analysis of Molecular Dynamics Simulations. **The Journal of Physical Chemistry A**, v. 107, n. 24, p. 4869–4876, 2003.

RICHARDSON, M. J.; DALE, R.; MARSH, K. L. Complex Dynamical Systems in Social and Personality Psychology: Theory, Modeling, and Analysis. **Handbook of Research Methods in Social and Personality Psychology**. 2o ed, p.253–282, 2014.

RODRÍGUEZ, I.; LEHMKUHL, O.; CHIVA, J.; BORRELL, R.; OLIVA, A. On the flow past a circular cylinder from critical to super-critical Reynolds numbers: Wake topology and vortex shedding. **International Journal of Heat and Fluid Flow**, v. 55, p. 91–103, 2015. Marbella, Spain.

ROSENSTEIN, M. T.; COLLINS, J. J.; DE LUCA, C. J. A practical method for calculating largest Lyapunov exponents from small data sets. **Physica D: Nonlinear Phenomena**, v. 65, n. 1, p. 117–134, 1993.

ROSHKO, A. Experiments on the flow past a circular cylinder at very high Reynolds number. **Journal of Fluid Mechanics**, v. 10, n. 3, p. 345–356, 1961.

ROUX, J.-C.; SIMOYI, R. H.; SWINNEY, H. L. Observation of a strange attractor. **Physica D: Nonlinear Phenomena**, v. 8, n. 1, p. 257–266, 1983.

ROVERI, N.; CARCATERRA, A. Damage detection in structures under traveling loads by Hilbert–Huang transform. **Mechanical Systems and Signal Processing**, Interdisciplinary and Integration Aspects in Structural Health Monitoring., v. 28, p. 128–144, 2012.

RUELLE, D. **Strange Attractors. Turbulence, Strange Attractors and Chaos**, World Scientific Series on Nonlinear Science Series A. v. Volume 16, p.195–206, 1995.

RUELLE, D.; TAKENS, F. On the nature of turbulence. **Communications in Mathematical Physics**, v. 20, n. 3, p. 167–192, 1971.

SAUER, T.; YORKE, J. A.; CASDAGLI, M. Embedology. **Journal of Statistical Physics**, v. 65, n. 3, p. 579–616, 1991.

SHIH, C.-L.; CHEN, W.-C.; CHANG, K.-C.; WANG, M.-R. Velocity measurements of turbulent wake flow over a circular cylinder. **International Journal of Modern Physics: Conference Series**, v. 42, p. 1660182, 2016.

SIKKANDAR, M. Y.; AKSHAYAA, V.; DINESH, A. D.; DINIKSHAA SREE, L. Analysis of cardiac abnormalities using Hilbert-Huang transform. **International Journal of Biomedical Engineering and Technology**, v. 13, n. 1, p. 69–86, 2013.

SILVEIRA, R. S.; MÖLLER, S. V. Hilbert-Huang Transform A Comparison With Fourier And Wavelet Transform For The Analysis Of The Shedding Process. 2012. Dublin.

SPIVACK, H. M. Vortex Frequency and Flow Pattern in the Wake of Two Parallel Cylinders at Varied Spacing Normal to an Air Stream. **Journal of the Aeronautical Sciences**, v. 13, n. 6, p. 289–301, 1946.

STROUHAL, V. Ueber eine besondere Art der Tonerregung. **Annalen der Physik**, v. 241, n. 10, p. 216–251, 1878.

SUMNER, D. Two circular cylinders in cross-flow: A review. **Journal of Fluids and Structures**, v. 26, n. 6, p. 849–899, 2010.

SUMNER, D.; WONG, S. S. T.; PRICE, S. J.; PAÏDOUSSIS, M. P. Fluid Behavior of side-by-side circular cylinders in steady cross-flow. **Journal of Fluids and Structures**, v. 13, p. 309–338, 1999.

SWINNEY, H. L.; GOLLUB, J. P. Characterization of hydrodynamic strange attractors. **Physica D: Nonlinear Phenomena**, v. 18, n. 1, p. 448–454, 1986.

TAKENS, F. Detecting strange attractors in turbulence. In: D. Rand; L.-S. Young (Orgs.); Dynamical Systems and Turbulence, Warwick 1980. **Anais**... , Lecture Notes in Mathematics. p.366–381, 1981. Berlin, Heidelberg: Springer.

TENNEKES, H.; LUMLEY, J. L. **A First Course in Turbulence**. Cambridge, MA, 1972.

TITCHMARSH, E. **Introduction to the Theory of Fourier Integrals**. 2 edition ed. Oxford: Clarendon Press, 1948.

TONG, H. **Non-linear Time Series: A Dynamical System Approach**. Oxford: Oxford University Press, 1993.

TOWNSEND, A. A. **The Structure of Turbulent Shear Flow**. London: Cambridge University Press, 1956.

TSAI, F.-F.; FAN, S.-Z.; LIN, Y.-S.; HUANG, N. E.; YEH, J.-R. Investigating Power Density and the Degree of Nonlinearity in Intrinsic Components of Anesthesia EEG by the Hilbert-Huang Transform: An Example Using Ketamine and Alfentanil. **PLoS ONE**, v. 11, n. 12, 2016.

TSAI, P.-H.; LIN, C.; TSAO, J.; et al. Empirical mode decomposition based detrended sample entropy in electroencephalography for Alzheimer's disease. **Journal of Neuroscience Methods**, v. 210, n. 2, p. 230–237, 2012.

VELTCHEVA, A. D.; SOARES, C. G. Identification of the components of wave spectra by the Hilbert Huang transform method. **Applied Ocean Research**, v. 26, n. 1–2, p. 1–12, 2004.

VELTCHEVA, A. D.; SOARES, C. G. Analysis of Abnormal Wave Records by the Hilbert–Huang Transform Method. **Journal of Atmospheric and Oceanic Technology**, v. 24, n. 9, p. 1678–1689, 2007.

VINCENT, C.; GIEBEL, G.; PINSON, P.; MADSEN, H. Resolving Nonstationary Spectral Information in Wind Speed Time Series Using the Hilbert–Huang Transform. **Journal of Applied Meteorology and Climatology**, v. 49, n. 2, p. 253–267, 2010.

WIESELSBERGER, C. **New data on the laws of fluid resistance**. Washington D.C. : National Advisory Committee for Aeronautics, 1922.

WILLIAMSON, C. H. K. Vortex Dynamics in the Cylinder Wake. **Annual Review of Fluid Mechanics**, v. 28, n. 1, p. 477–539, 1996.

WOLF, A.; SWIFT, J. B.; SWINNEY, H. L.; VASTANO, J. A. Determining Lyapunov exponents from a time series. **Physica D: Nonlinear Phenomena**, v. 16, n. 3, p. 285–317, 1985.

WU, Z.; HUANG, N. E. Ensemble empirical mode decomposition: a noise-assisted data analysis method. **Advances in Adaptive Data Analysis**, v. 01, n. 01, p. 1–41, 2009.

XIE, H.; WANG, Z. Mean frequency derived via Hilbert-Huang transform with application to fatigue EMG signal analysis. **Computer Methods and Programs in Biomedicine**, v. 82, n. 2, p. 114–120, 2006.

YANG, A. C.; HUANG, N. E.; PENG, C.-K.; TSAI, S.-J. Do Seasons Have an Influence on the Incidence of Depression? The Use of an Internet Search Engine Query Data as a Proxy of Human Affect. **PLOS ONE**, v. 5, n. 10, p. e13728, 2010.

YANG, F.; AN, H.; CHENG, L. Drag crisis of a circular cylinder near a plane boundary. **Ocean Engineering**, v. 154, p. 133–142, 2018.

YANG J. N.; LEI Y.; LIN S.; HUANG N. Hilbert-Huang Based Approach for Structural Damage Detection. **Journal of Engineering Mechanics**, v. 130, n. 1, p. 85–95, 2004.

YEON, S. M.; YANG, J.; STERN, F. Large-eddy simulation of the flow past a circular cylinder at sub- to super-critical Reynolds numbers. **Applied Ocean Research**, v. 59, p. 663–675, 2016.

YINFENG, D.; YINGMIN, L.; MINGKUI, X.; MING, L. Analysis of earthquake ground motions using an improved Hilbert–Huang transform. **Soil Dynamics and Earthquake Engineering**, v. 28, n. 1, p. 7–19, 2008.

ZAN, S. J. Experiments on circular cylinders in crossflow at Reynolds numbers up to 7 million. **Journal of Wind Engineering and Industrial Aerodynamics**, 5th International Colloquium on Bluff Body Aerodynamics and Applications., v. 96, n. 6, p. 880–886, 2008.

ZDRAVKOVICH, M. M. REVIEW—Review of Flow Interference Between Two Circular Cylinders in Various Arrangements. **Journal of Fluids Engineering**, v. 99, n. 4, p. 618–633, 1977.

ZDRAVKOVICH, M. M. **Flow Around Circular Cylinders: Volume I: Fundamentals**. OUP Oxford, 1997.

ZHOU, Y.; ALAM, M. Wake of two interacting circular cylinders: A review. **International Journal of Heat and Fluid Flow**, v. 62, p. 510–537, 2016.

ZHU, L.; QIU, X.; LUO, J.; LIU, Y. Scale properties of turbulent transport and coherent structure in stably stratified flows. **Applied Mathematics and Mechanics**, v. 37, n. 4, p. 443–458, 2016.

APPENDIX A Single Cylinder Results

A.1 Same Reynolds number

In this section, the different diameters are analyzed under the same Reynolds number, $Re = 1.71\text{x}10^4$. Figure A.1 shows the power spectral density, as a function of the Strouhal number, for three diameters. The frequency peaks found in the spectra correspond to Strouhal numbers of 0.2240, 0.2181 and 0.2289 for D = 25.1 mm, 32 mm, and 50 mm respectively.

The Ensemble empirical mode decomposition (EEMD) was performed on the velocity signals for the three diameters. The decomposition resulted for each signal in 16 Intrinsic Mode Functions (IMF) plus a residue which is a monotonic function from which no further IMF can be extracted. The IMFs for D = 25.1 mm are represented in Fig. A.2, only the first 10 seconds of data are shown to enable better visualization of the oscillatory behavior of each component. The IMFs for the other diameters have very similar characteristics and therefore will be disregarded.

Each oscillatory mode present in the flow is represented by an IMF; small order IMF components represent the high frequency terms and the finest scales in the flow. In Fig. A.2 it is possible to see that the total amplitude of the IMFs reduces as the frequency reduces. The oscillatory behavior that can be associated with the vortex formations and flow scales can be identified from IMF 1 to 8 (C1 to C8). Looking in detail to IMF 3 (C3), Fig. A.3 a), it is possible to see an oscillatory behavior characteristic of vortex shedding caused by the cylinder in the flow. This oscillatory behavior is also seen in smaller amplitudes in IMF 4 and 5 (C4 and C5), Fig. A.3 b) and c). This demonstrates that the vortex shedding does not occur at a fixed frequency, but rather oscillates around a frequency range. IMF 8 (C8), which corresponds to the lower frequency and a larger scale, presents a more homogeneous oscillatory characteristic. High order IMFs (IMF C9 to C16) present an almost monotonic behavior and frequencies very close to zero. Those IMFs do not have any physical significance in the flow and can be considered as pseudo frequencies originated from the decomposition.

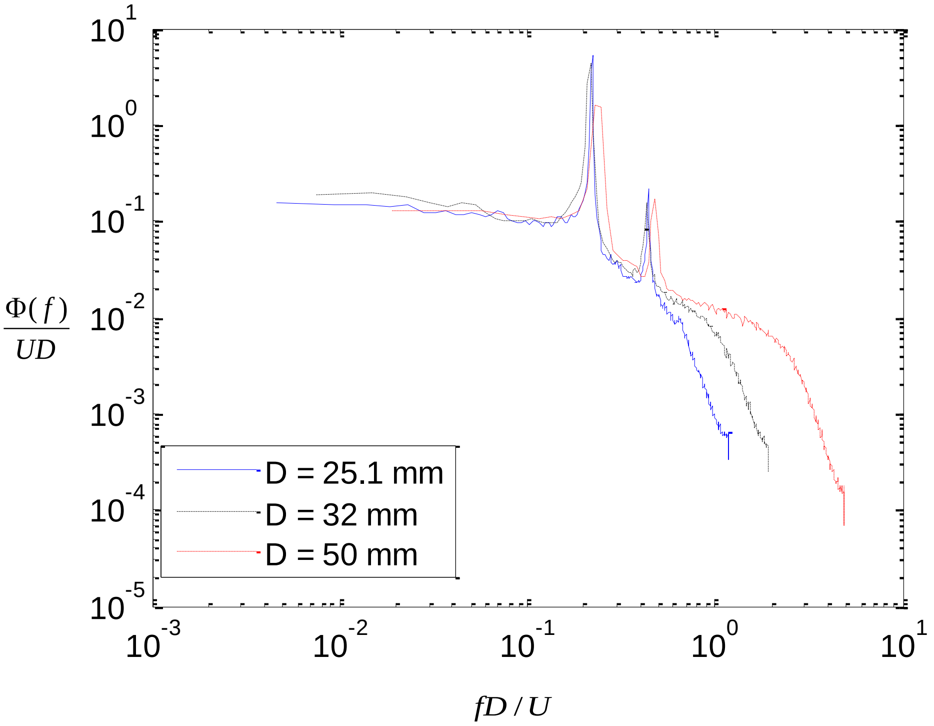

Figure A.1- Dimensionless power spectra for different diameters and *Re* = 1.71x10^4.

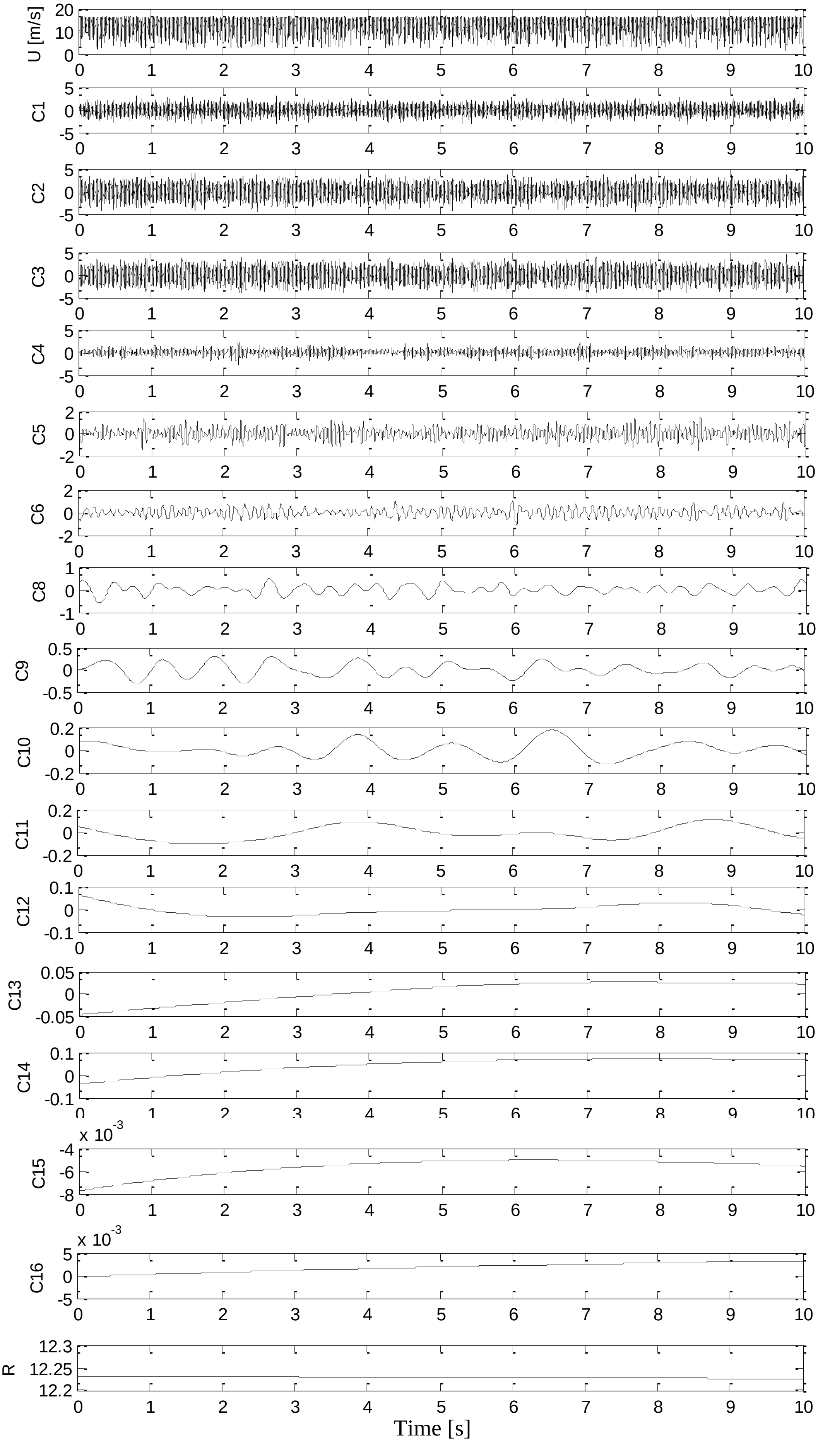

Figure A.2 – Intrinsic Mode Functions and residue for *D* = 25.1 mm. *Re* = 1.71x10^4.

According to Huang et al., 2013 the physical meaning of IMFs is the decomposition of the original signal in *quasieigenmodes* with locally homogeneous oscillating properties. The intrinsic mode functions represent, therefore, the flow wave modulations in their characteristic time scale. For a better comprehension of the scales involved in the flow, Fig. A.4, shows the wavenumber spectra of the 16 IMFs of the 25.1 mm diameter at $Re = 1.71 \text{x} 10^4$ and the spectra of the original velocity fluctuation.

It is possible to observe in the spectra that the first five IMF components are those carrying the features of the signal corresponding to the vortex shedding frequencies and the first harmonic, characterized by the peaks in turbulence spectra and corresponding IMF. Components from IMF 5 to IMF 8 correspond to the energy comprehended in the largest scales of the flow and generated by the channel itself. Subsequent IMFs have almost uniform energy for a gradual increase of the scales, characterized by the reduction of the dimensionless wavenumbers; therefore, they do not contribute with the fluid motion and present no physical flow meaning, and can be interpreted as an artifice of the method to fulfill the number of total IMFs. For better visualization of IMF features, in the following spectra, only the 8 first components will be represented.

Figures A.5, A.6, and A.7 present the dimensionless wavenumber spectra of IMF and velocity fluctuation for the three diameters 25.1 mm, 32 mm, and 50 mm, respectively, and the same Reynolds number $Re = 1.71 \text{x} 10^4$. The five first IMF are indicated by tags (C1 to C5) and contain information about the small scales in the flow, and the vortex shedding frequencies. One can see that the IMF components behave essentially the same way for all studied diameters, demonstrating the hypothesis of similarity and self-preservation of the flow by associating the IMF corresponding scale to a wavenumber in spectra. That hypothesis states that at all high Reynolds numbers the processes that determine the main structure of turbulent motion are independent of the fluid viscosity and that the structure at all instants of time is similar [Townsend, 1956].

Since each IMF represents locally homogeneous oscillating properties, it is possible to associate each one of them to a corresponding dimensionless wavenumber k^*, and consequently to a flow scale. The first IMF (C1) can be associated with the finest scales in the flow and fits in the wavenumber range of $4 < k^* < 21$. Component C2 englobes part of the fine scales and the frequencies related to the first harmonic, $1 < k^* < 6$. Third, to fifth IMFs (C3 to C5) present the contents corresponding to the energy of vortex shedding, fitting in the range of wavenumber $0.2 < k^* < 2$. IMFs C6 to C8 correspond to the wave modulations of the largest scales in the flow and contribute to the fluid motion energy, also they are related to vortices generated by the channel itself from $0.02 < k^* < 0.2$. Higher orders IMFs do not have a significant energetic contribution to the fluid motion and can be considered as a *pseudofrequency*, originated from the decomposition method, they present dimensionless wavenumber $k^* < 0.02$.

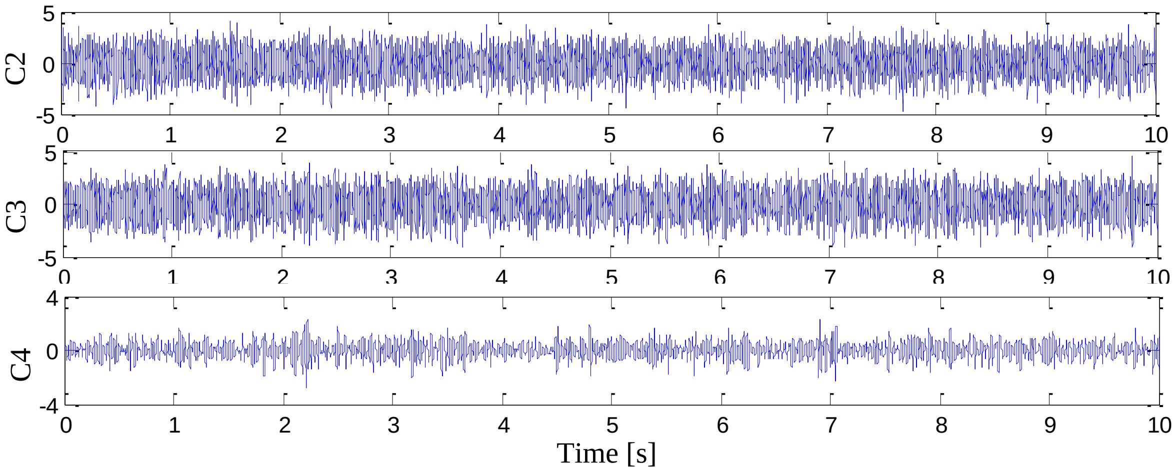

Figure A.3 – Detail of IMF components C2, C3, and C4.

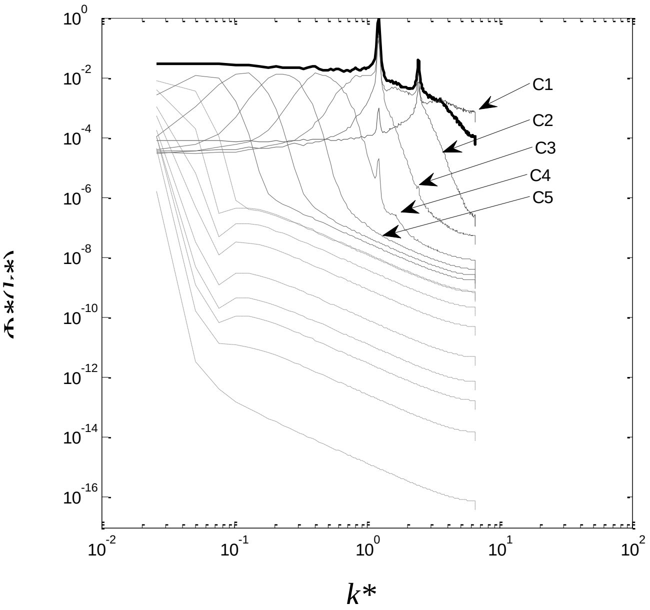

Figure A.4 – Dimensionless wavenumber spectra of IMF components and velocity fluctuation for D = 25.1 mm, $Re = 1.71\text{x}10^4$. Velocity fluctuation is a solid black bold line. IMF components 1 to 5 are in solid grey lines and indicated by arrows (C1 to C5). Higher-order IMFs are in dashed lines.

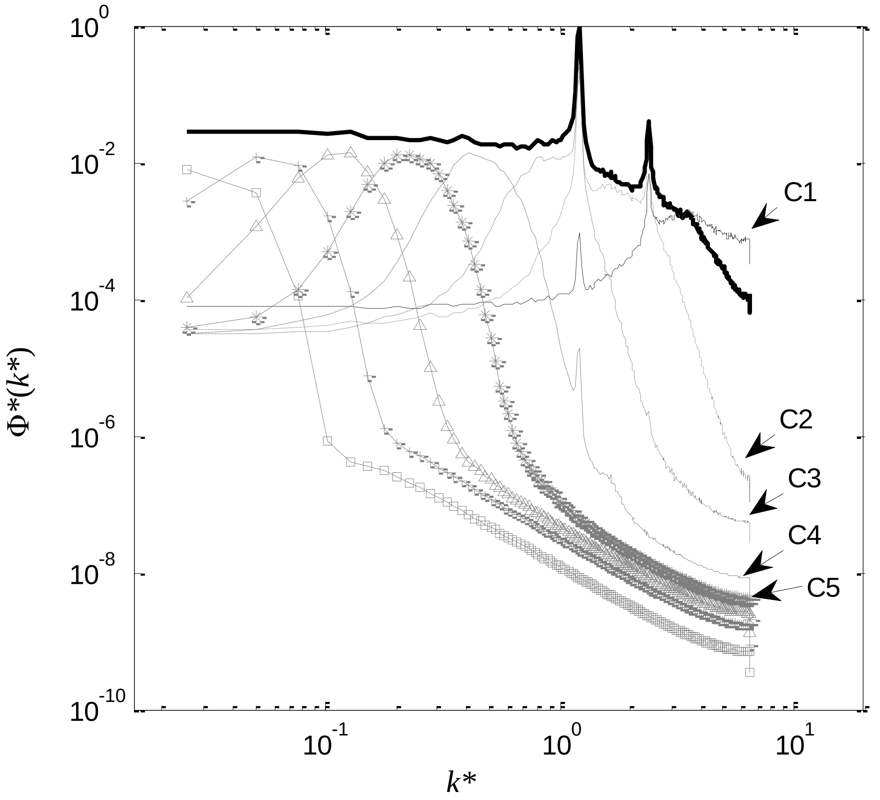

Figure A.5 – Dimensionless wavenumber spectra for *D* = 25.1 mm. *Re* = 1.71×10^4.

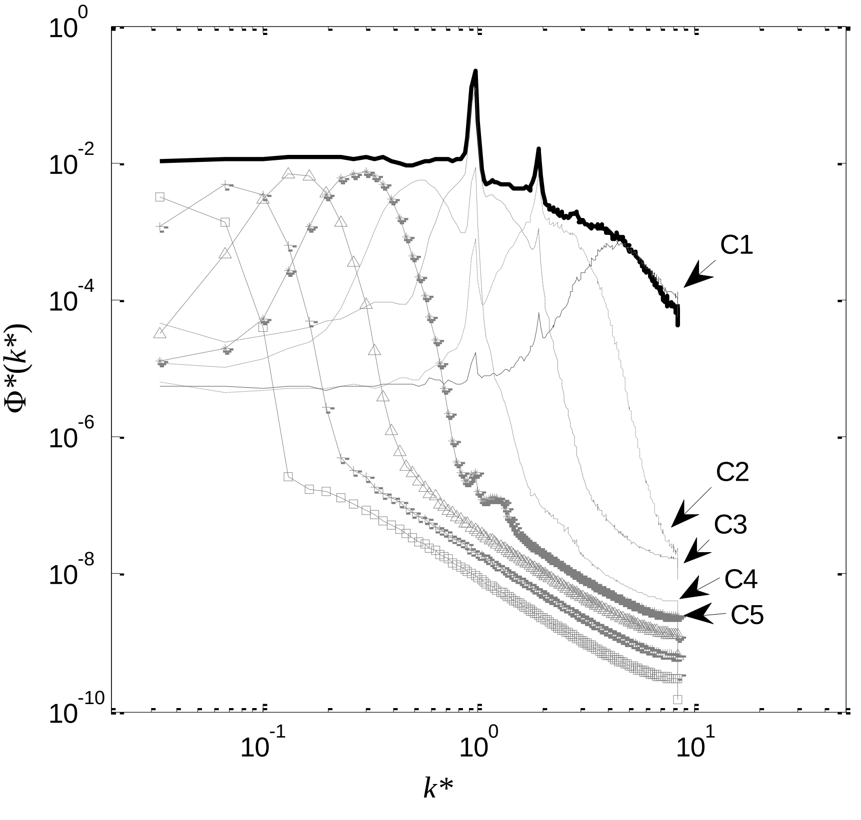

Figure A.6 - Dimensionless wavenumber spectra for *D* = 32 mm and. *Re* = 1.71×10^4.

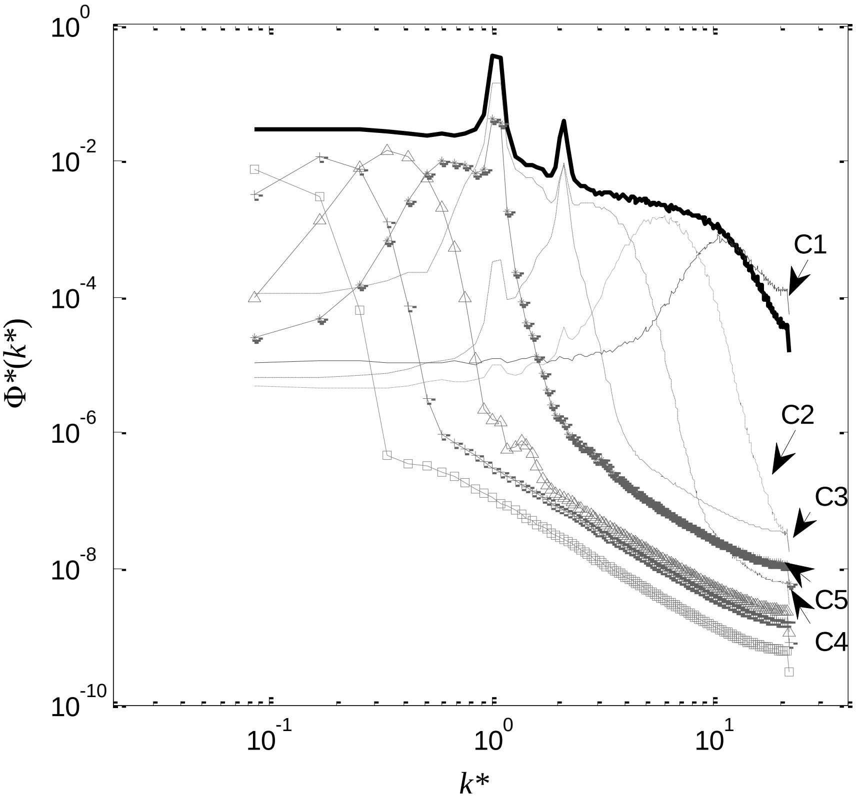

Figure A.7 – Dimensionless wavenumber spectra for D = 50 mm. $Re = 1.71\times10^4$.

Based on the definition of IMF, which is any function having symmetrical envelopes defined by the local maxima and minima separately, in which the number of zero-crossings differs at most by one from the number of extrema, one can determine the mean period of the function by counting the number of peaks (local maxima) of the function. Table A.1 lists the mean period in terms of the number of data points, and the corresponding period in seconds, for the IMF mode generated for the signal from the 25.1 mm cylinder with a data sample of 131,072 points. By analyzing the mean period of each of the 16 IMF, it is possible to identify that for any IMF component each mean period almost doubles the value of the previous one. From the spectra of the IMF components in Fig. A.4, it is observed that the IMFs tend to organize themselves like a filter bank structure. The filter associated with the first mode (C1) is essentially a high pass filter, and the modes of higher order are characterized by a set of overlapping bandpass filters. Furthermore, each mode of the index (i + 1), $i \geq 2$ occupies a frequency domain which is approximately the upper half-band of that of the previous index [Flandrin et al., 2004].

Table A.1 - Mean period associated with each IMF, for D = 25.1 mm, $Re = 1.71\times10^4$.

IMF Mode nº	1	2	3	4	5	6	7	8
Mean Period *T*	3.1508	7.3454	10.0269	23.3017	47.0298	92.4344	182.8061	363.0803
Period *T* [s]	0.024	0.056	0.077	0.178	0.358	0.705	1.395	2.770
IMF Mode nº	9	10	11	12	13	14	15	16
Mean Period *T*	740.52	1456.4	2849.4	5461.3	13170	21845	65536	131072
Period *T* [s]	5.649	11.111	21.739	41.666	100.479	166.664	500.000	1000.000

After performing the EEMD on the velocity signal, the Hilbert transform is applied to each IMF component. The Hilbert spectral analysis shows each instantaneous frequency at its corresponding time and energy amplitude. It can be interpreted as a weighted non-normalized joint amplitude-frequency-time distribution, the local amplitude being the weight assigned to each time-frequency cell, giving the exact occurring time of the oscillations [Huang et al., 1998].

Figure A.8 shows the normalized Hilbert Energy Spectra (NHES) for different diameters and a constant Reynolds number. The vertical axis on the left side of the graphic represents frequency in Hz, the vertical axis on the right side is the corresponding Strouhal number. The lower horizontal axis represents time in seconds, and the upper horizontal axis is a dimensionless time. It is observed that the higher concentrations of amplitude for each diameter are in the band range that corresponds to the vortex shedding frequencies, which are 93.74 Hz, 56.64 Hz, and 23.44 Hz, and corresponding Strouhal numbers of 0.2240, 0.2181, and 0.2289. That was expected since this range corresponds to the most energetic IMFs. It is also visible that the shedding frequency is not constant; rather it oscillates about a constant value, corresponding to a St ≈ 0.21 along time. The energy contents of the first harmonics are also present in the NHES but in a larger frequency band, giving to them a more dispersed appearance and very poor resolution, which difficult identification. The pseudo frequencies created by the decomposition method appear concentrated in the frequencies close to zero and have no physical meaning.

Figure A.9 shows the continuous Wavelet transform of the velocity signal. A db20 wavelet was used in this analysis. The highlighted energy is concentrated in the bands around the vortex shedding frequency. Due to the characteristic of the wavelet transform of a giving frequency resolution and consequently uniformly poor time resolution [Huang et al., 1999], the effects of the wavelet are visible in frequencies higher and lower than the actual vortex shedding frequency. In comparison, the NHES defines clearly what the frequency limits are, and though there is some dispersion in the highest frequencies, it is also possible to visualize the presence of the first harmonic, especially in Fig. A.8 b), in the region around 100 Hz. Results corroborate that the shedding frequency is not constant as shown in Fig. A.9.

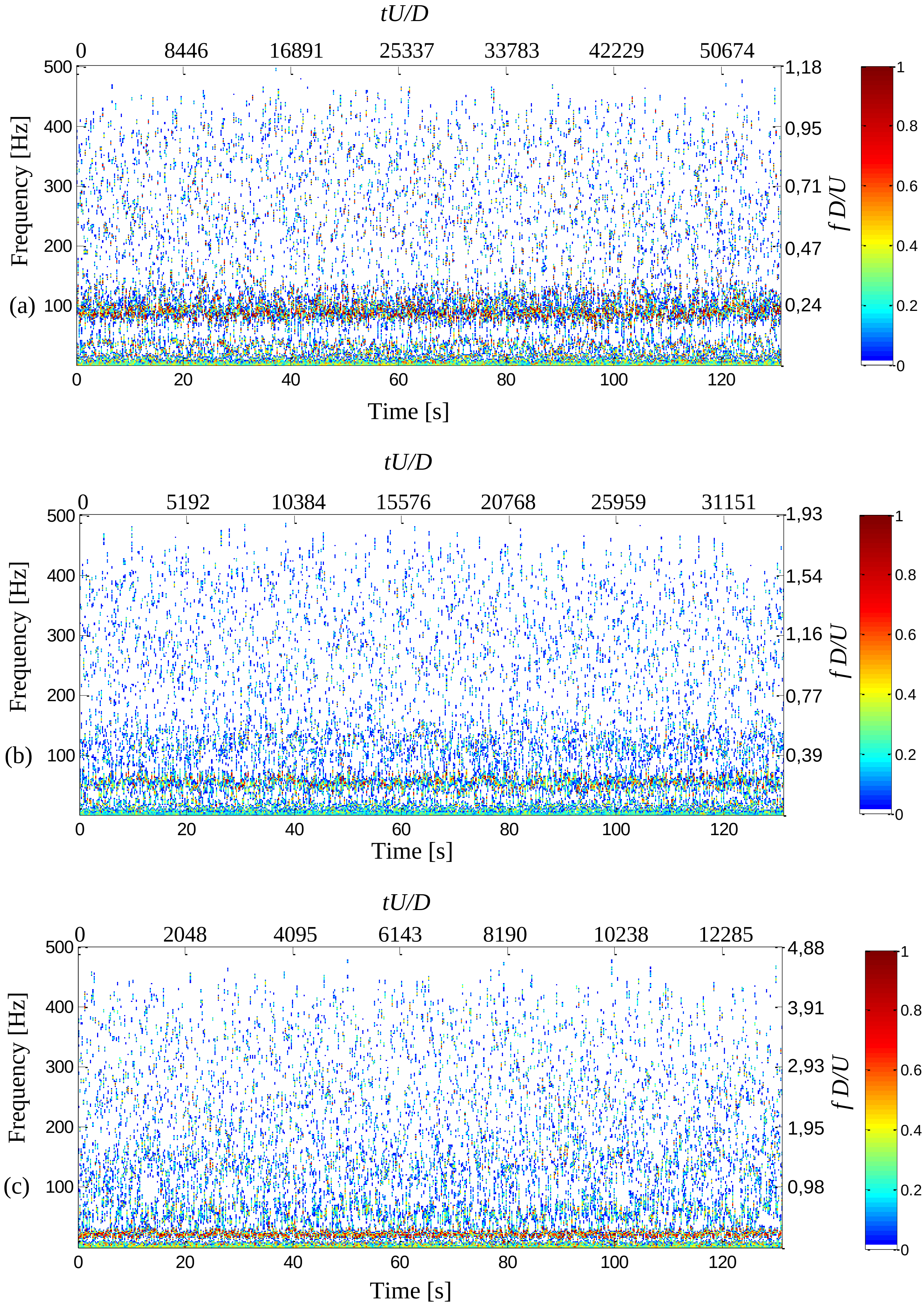

Figure A.8 – Normalized Hilbert spectrum for (a) D = 25.1 mm, (b) D = 32 mm and (c) D = 50 mm. $Re = 1.71 \times 10^4$.

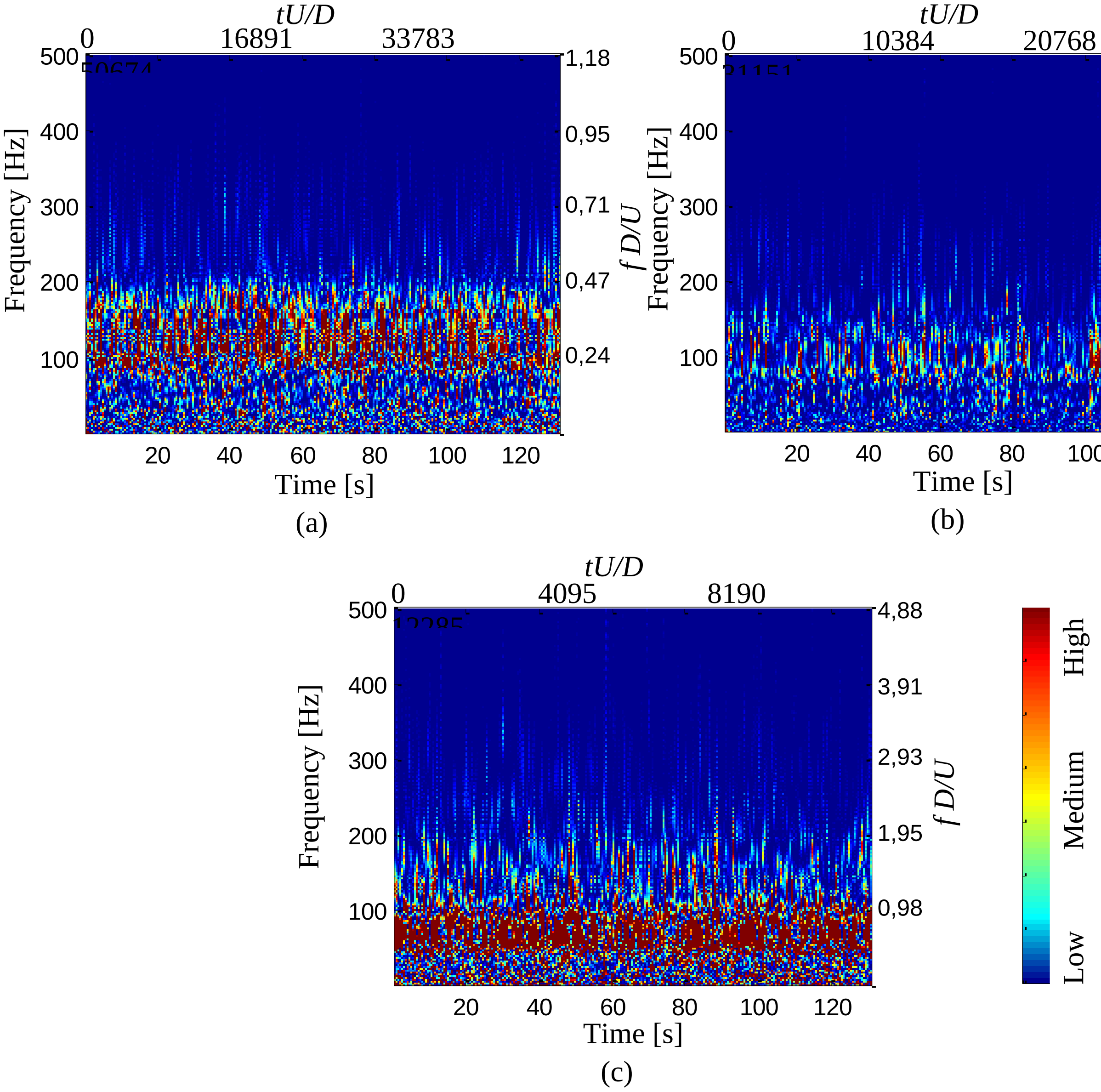

Figure A.9 - Continuous Wavelet transform (a) *D* = 25.1mm, (b) *D* = 32 mm, and (c) *D* = 50 mm. *Re* = 1.71×10^4.

By definition, a coherent structure is a large-scale turbulent mass of fluid with phase-correlated vorticity over its spatial extent [Hussain, 1983], distinguished in a turbulent flow from how much energy it contains. The EEMD method also recognizes the coherent structure in the sense of the mean energy. A mode can be considered a coherent structure if its mean energy exceeds 10% of the whole fluctuation energy [Zhu et al., 2016].

The Mean Square Energy (MSE) was calculated according to Eq. 40. Figure A.10 illustrates the dimensionless mean square energy of each IMF for the three diameters at the same Reynolds number, *Re* = 1.71×10^4. The energy increases in the first IMF modes, reaching the maximum value at the third IMF (C3) for 25.1 and 32 mm; the maximum value occurs at the fourth IMF (C4) for the 50 mm. Compared with the whole energy fluctuations, those modes with maximum values account for 62.7 %, 48.9 %, and 53.36 % of the total energy, respectively. After reaching the maximum value, the energy starts decreasing in the higher-order IMFs reaching a minimum at C8 and remaining constant for higher-order IMFs. The decrease in the energy amounts for the higher-order IMF is also indicative that the large scale does not have a significant contribution to the dynamics of the fluid motion after the cylinder. Hence, IMF 9 to 16 have similar energy for all diameters, most likely because they correspond to pseudo frequencies generated by the decomposition method, and do not have physical significance.

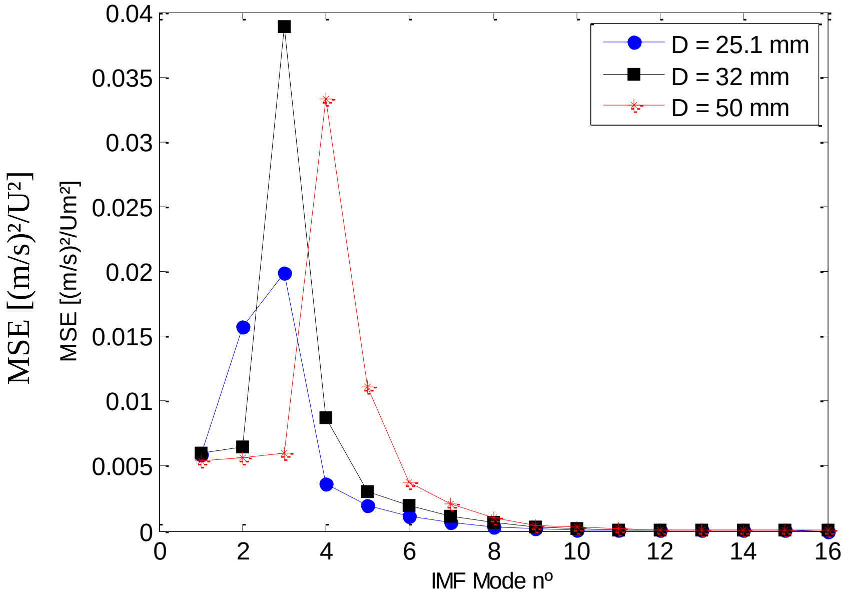

Figure A.10 – Dimensionless Mean Square energy for different diameters. *Re* = 1.71x10^4.

Figure A.11 presents the joint Probability Density Function (PDF) of the normalized amplitude and frequency of the first five IMF components for the various diameters at the same Reynolds number. The inferior horizontal axis represents frequency in Hz, and the upper horizontal axis represents the dimensionless wavenumber (*k**). It is possible to observe that the first IMF contains higher frequencies, and its amplitude is lower, with the concentrations distributed in a wide range of frequency values, from around 200 Hz to 500 Hz. For 25.1 mm the first IMF (C1) presents two areas of main concentrations, one in the range of 200 Hz to

320 Hz and the other in the range of 350 Hz to 450 Hz. This behavior for C1 is not visualized in the PDFs for other diameters. As the IMF order increases, the distributions concentrate in smaller ranges of frequencies, since the increase in the IMF order means large flow scales and a more monotonic IMF component. Also, the overlapping of IMF components is observed in the range of the vortex shedding frequencies; this behavior is due to the oscillation of the vortex shedding frequency around a fixed value, hence more than one IMF containing those frequencies, as was observed in the spectra in Figs. A.5, A.6, and A.7.

By observing Fig. A.11 the IMFs with higher energy for $Re = 1.71\times10^4$ are C3, for cylinders with a diameter of 25.1 and 32 mm and C4 and C5 for the 50mm cylinder. These IMFs have two important features, compared to the others: they are concentrated on a region about the shedding frequency, showing that the shedding process does not occur on a sharp fixed frequency, rather it wanders about that value, and there is a high probability of these frequencies present high amplitudes combined with high energy values. These IMFs correspond to the shedding vortices characterizing, according to Hussain, 1983, the so-called preferred mode, the characteristic geometric configuration of the structure in the physical space. The wandering shedding frequency may be a consequence of the three-dimensionality of the wake flow resulting from vortex dislocation along the cylinder and time [Miau et al., 2007]. Therefore, EEMD is an efficient process of the eduction of coherent structures.

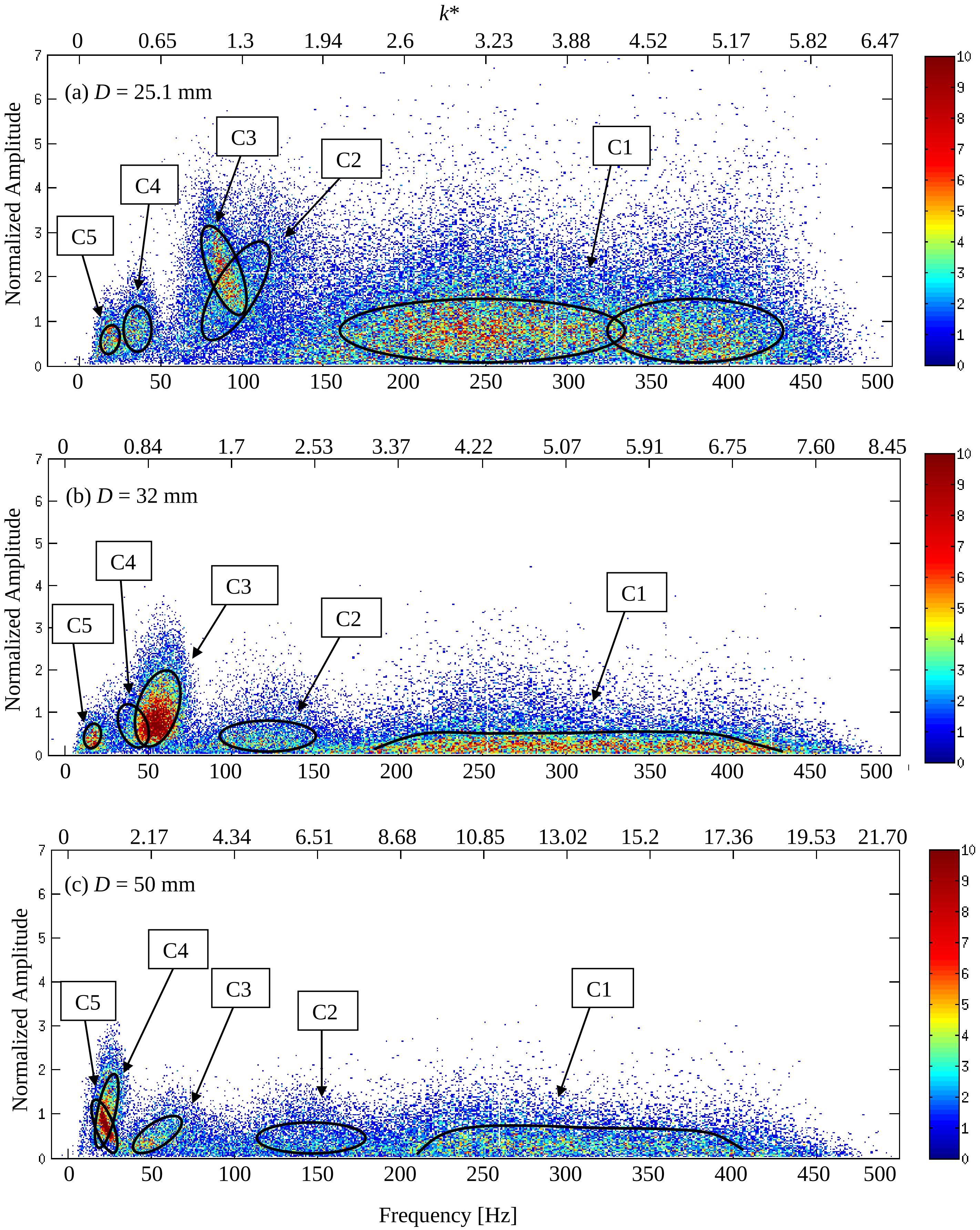

Figure A.11 – Joint PDF of amplitude and frequency for (a) D = 25.1mm, (b) D = 32 mm and (c) D = 50 mm. $Re = 1.71\times10^4$.

A.2 Different Reynolds numbers

In this section, the previous study is extended to various Reynolds numbers for the previous diameters. Figure A.12 represents the dimensionless power spectra as a function of Strouhal number for the diameters of 25.1, 32, and 50 mm at various Reynolds numbers corresponding to free stream velocities of U = 5.08, 10.5, and 16 m/s, according to Table A.1.

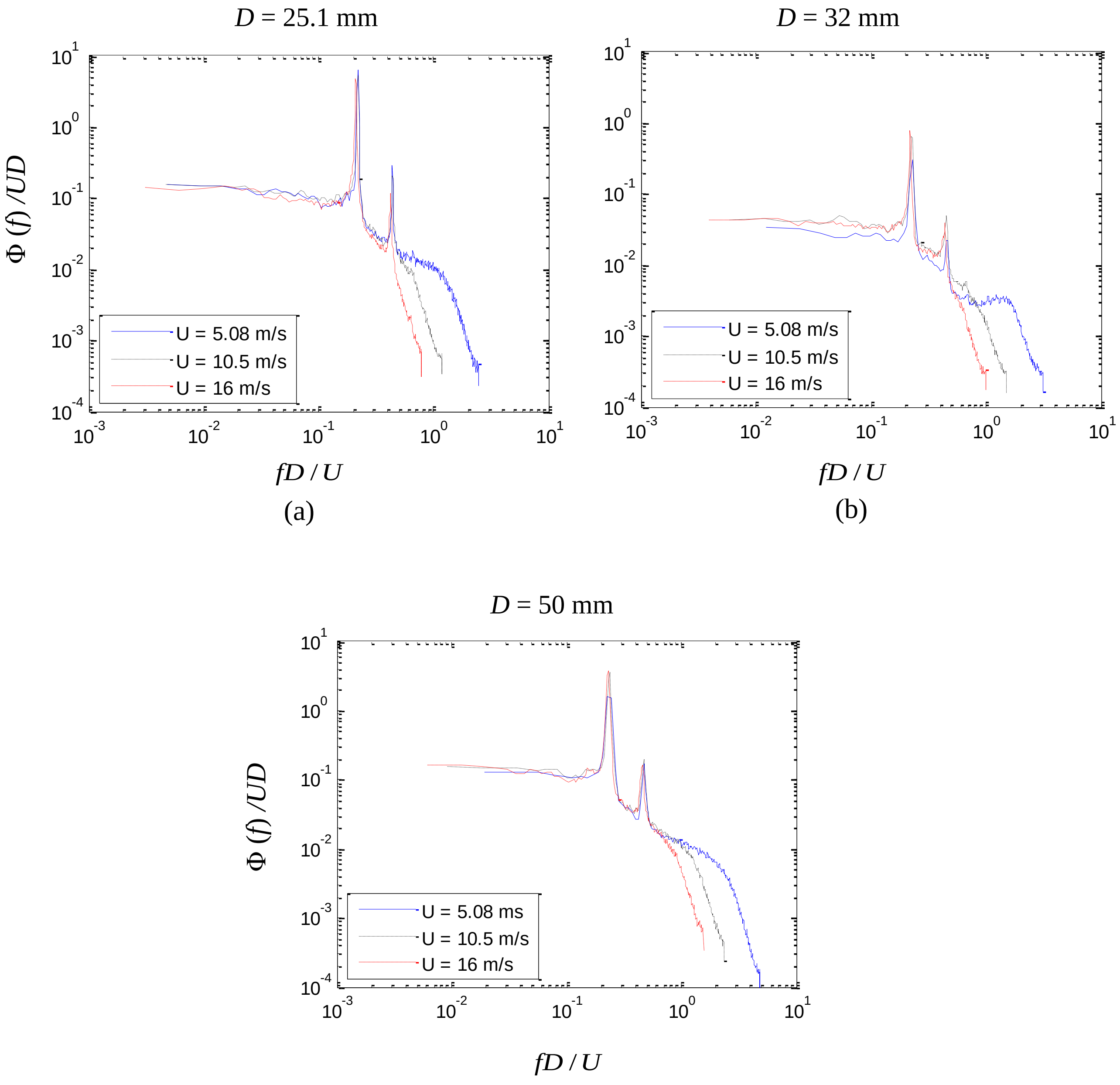

(a)

(b)

(c)

Figure A.12 - Dimensionless power spectra for different diameters for various *Re*, (a) D = 25.1 mm; (b) D = 32 mm and (c) D = 50 mm.

The EEMD method was applied to the various velocity signals generating a set of 16 IMF components for each signal. Due to the similarities with the IMF components shown in Fig. A.2, this part will be omitted in this section.

The wavenumber spectra showing the variation in the Reynolds number and the influence in the IMF structure are shown for various diameters in Fig. A.13, for *D* = 25.1 mm, Fig. A.14, for *D* = 32 mm, and Fig. A.15, for *D* = 50 mm. Essentially all the IMFs in the many different Reynolds numbers behave the same. The first IMFs, usually C1 to C5, comprehend the flow features such as the vortex shedding frequency. Higher-order IMFs, from C6 to C8, represent the flow motion energy or the large scales. Therefore, as one can see, the self-preservation and self-similarity hypotheses do not depend on the Reynolds number.

The filter bank characteristic of IMF also does not suffer the influence of the Reynolds number. It is visible that as the Reynolds number increases, the spectra dislocate the first IMFs to the right (higher wavenumbers), this influences the IMFs corresponding to the vortex shedding frequencies. So, as the Reynolds number reduces, the order of the IMFs corresponding to the shedding process increases.

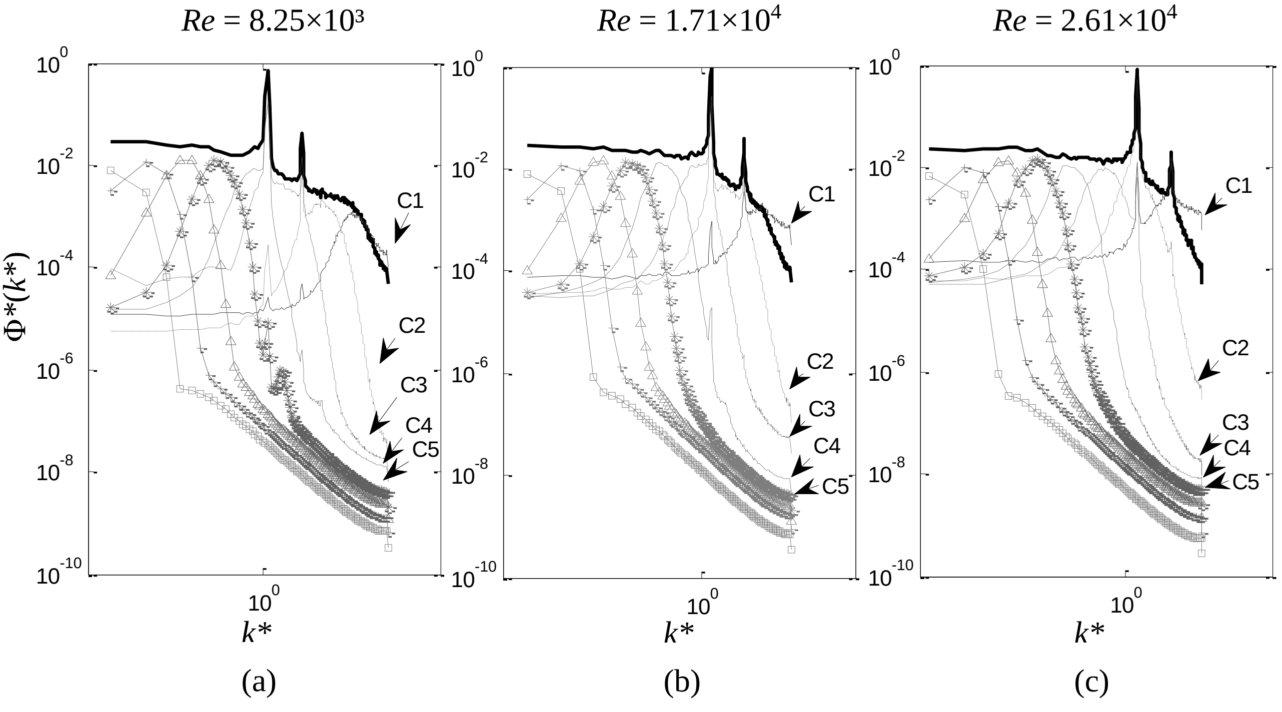

Figure A.13 – Dimensionless wavenumber power spectral density for *D* = 25.1 mm, (a) *Re* = 8.25×10^3, (b) *Re* = 1.71×10^4, and (c) *Re* = 2.61×10^4.

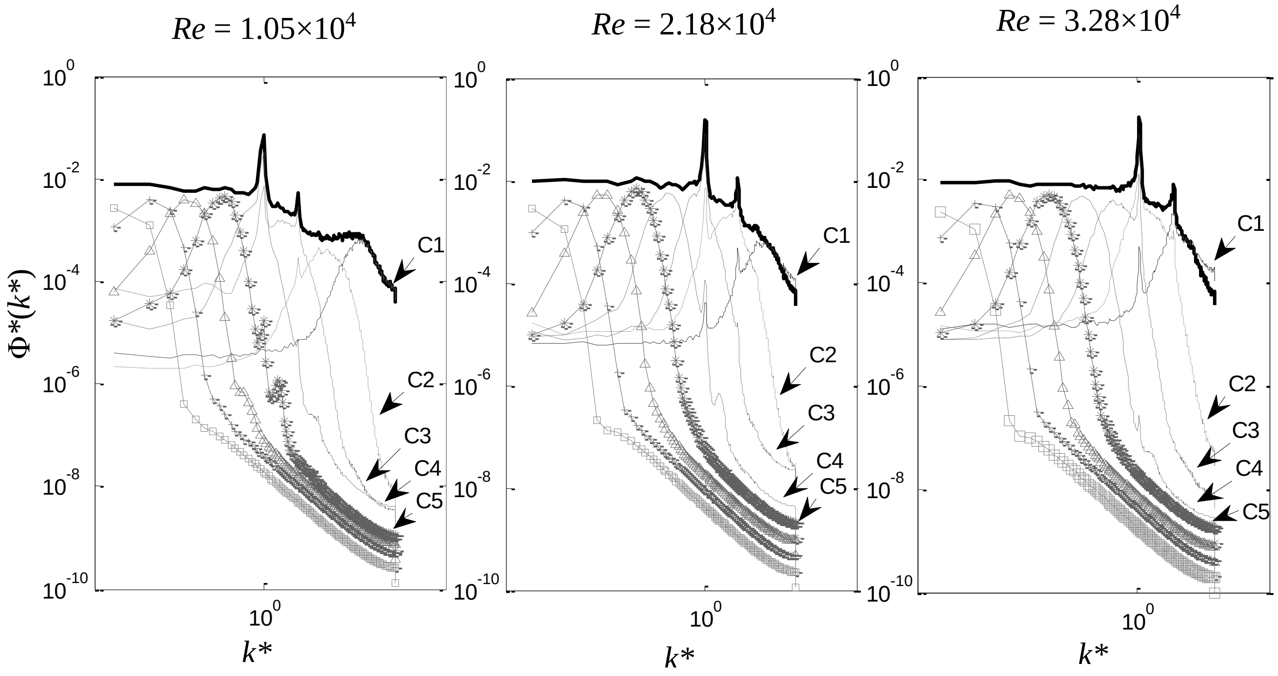

(a) (b) (c)

Figure A.14 – Dimensionless wavenumber power spectral density for D = 32 mm, (a) $Re = 1.05\times10^4$, (b) $Re = 2.18\times10^4$, and (c) $Re = 3.28\times10^4$.

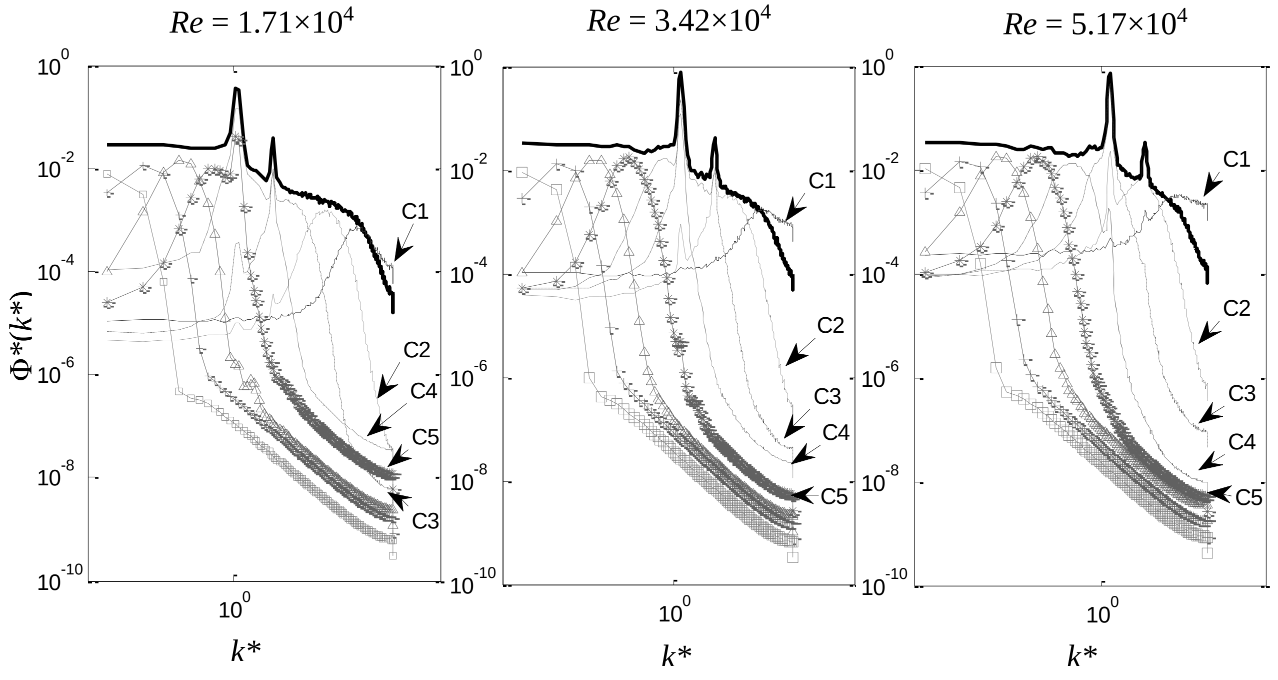

(a) (b) (c)

Figure A.15 - Dimensionless wavenumber power spectral density for D = 50 mm, (a) $Re = 1.71\times10^4$, (b) $Re = 3.42\times10^4$, and (c) $Re = 5.17\times10^4$.

The Normalized Hilbert-Huang transform was performed on each set of IMFs of each signal. Figure A.16 shows the NHES for $D = 25.1$ mm at various Reynolds numbers. One can see the evolution and increase in the frequency of vortex shedding with the increase in Reynolds number.

Calculating the mean square energy of the IMFs for each diameter, represented in Fig. A.17 for $D = 25.1$; Fig. A.18 for $D = 32$ mm and Fig. A.19 for $D = 50$ mm, is possible to identify a pattern in the behavior of the most energetic IMF. The augment in Reynolds number reduces the order of the IMF containing the biggest amount of energy that is also visible in the power spectrum represented in Figs. A.13, A.14, and A.15. The most energetic IMF, corresponding to the location of the coherent structures of the flow varies from IMF 4 or 3, for the lowest velocity, and IMF 2 or 1 for the highest velocity.

The Joint PDFs the normalized amplitude and frequency for the first five IMFs, in the various Reynolds numbers, for $D = 32$ mm, are shown in Fig. A.20. The upper horizontal axis represents dimensionless wavenumber (k^*), the lower horizontal axis represents frequency in Hz. As the Reynolds number increases for a constant diameter, the amplitude of the energy also increases. The higher energy IMF changes according to the Reynolds numbers, for the smallest Reynolds number $Re = 1.05\times10^4$, is C4, for $Re = 2.18\times10^4$ is C3 and for $Re = 3.28\times10^4$ is C2. It is possible to see that those IMF containing the vortex shedding features tend to overlap with other IMF components like C4 with C3 and C5 for $Re = 1.05\times10^4$, and C2 with C3 for $Re = 2.18\times10^4$, showing that the shedding process does not occur at a fixed frequency, but due to the three-dimensionality of the wake flow wanders around that value. This fact also demonstrates that the coherent structures are present and identified around the same flow scale, corresponding to the wavenumber range of $k^* = 0.9$ to $k^* = 2.50$.

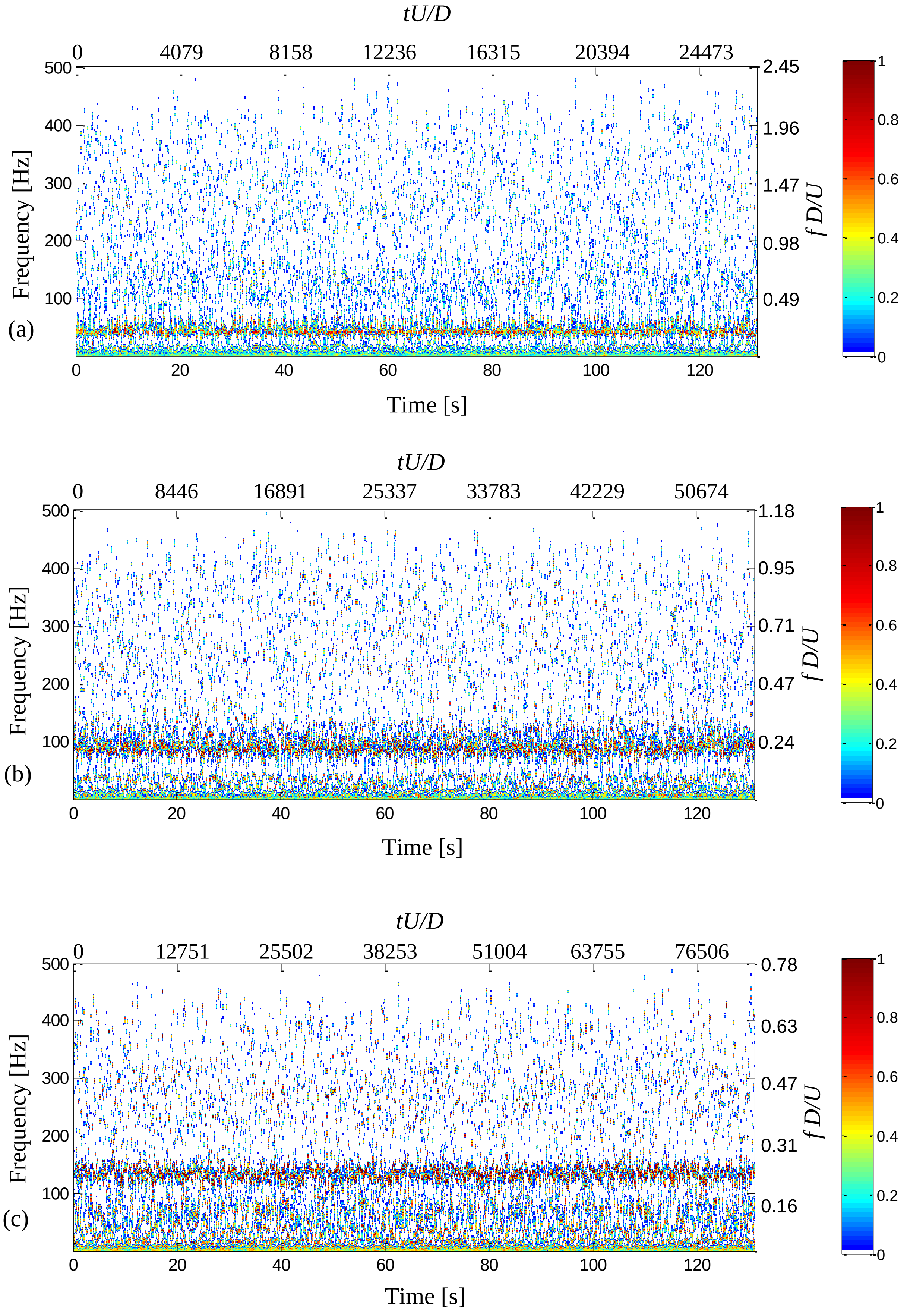

Figure A.16 – Normalized Hilbert spectrum for D = 25.1 mm. (a) $Re = 8.25\times10^3$, (b) $Re = 1.71\times10^4$, and (c) $Re = 2.61\times10^4$.

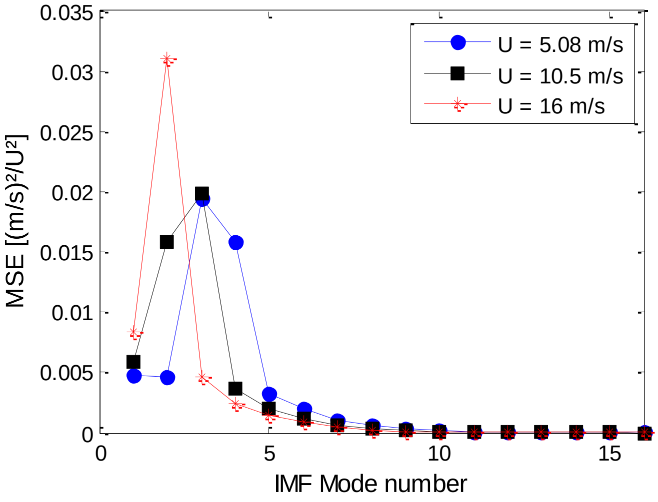

Figure A.17 – Dimensionless mean square energy for *D* =25.1 mm at various Reynolds numbers.

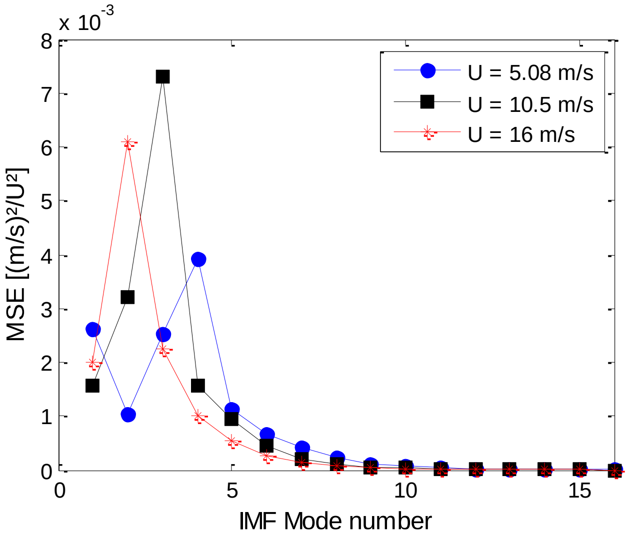

Figure A.18 – Dimensionless mean square energy for *D* =32 mm at various Reynolds numbers.

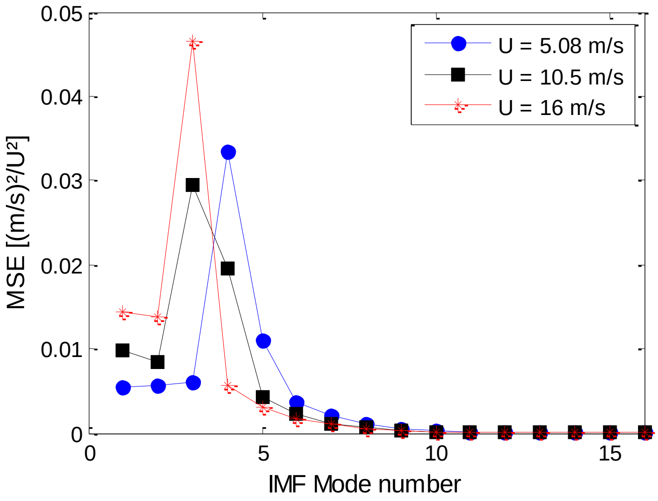

Figure A.19 – Dimensionless mean square energy for *D* =50 mm at various Reynolds numbers.

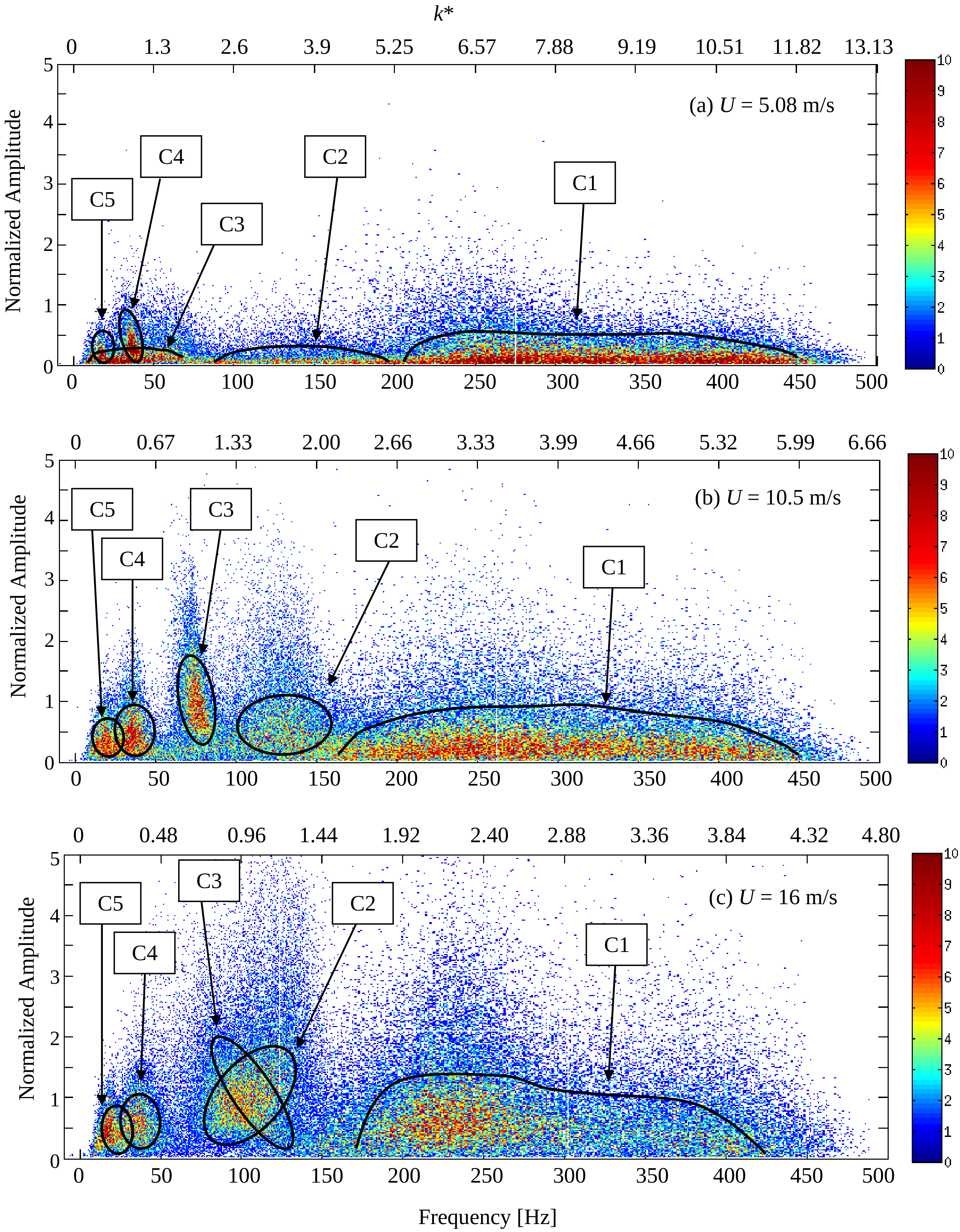

Figure A.20 - Joint PDF of amplitude and frequency for *D* = 32 mm at (a) *U* = 5.08 m/s, (b) *U* = 10.5 m/s and (c) *U* = 16 m/s.

APPENDIX B Double Well Analogy

Figure B.1 is referent to the analogy made in Chapter 4, Section 4.3.

For a simple mechanical system, considering the potential V(t) to be kinetic energy,M1 and M2 represent the two wake modes. For lower values of Reynolds for example, there will be a minimum admissible velocity for the system, represented as a grey line in Fig. B.1. Since the system is non-linear, there would be some time instant and some modes where the system would accumulate energy in one of the modes and jump into the other mode. As the Reynolds increases, the contribution of energy became more elevated, meaning that the switch between the two bistable modes became easier since the value of energy that needs to accumulate to jump from one mode to the other is smaller. Therefore, the system became more chaotic and more unpredictable, and eventually, the bistable characteristics would be lost, and the flow would assume a flip-flopping configuration.

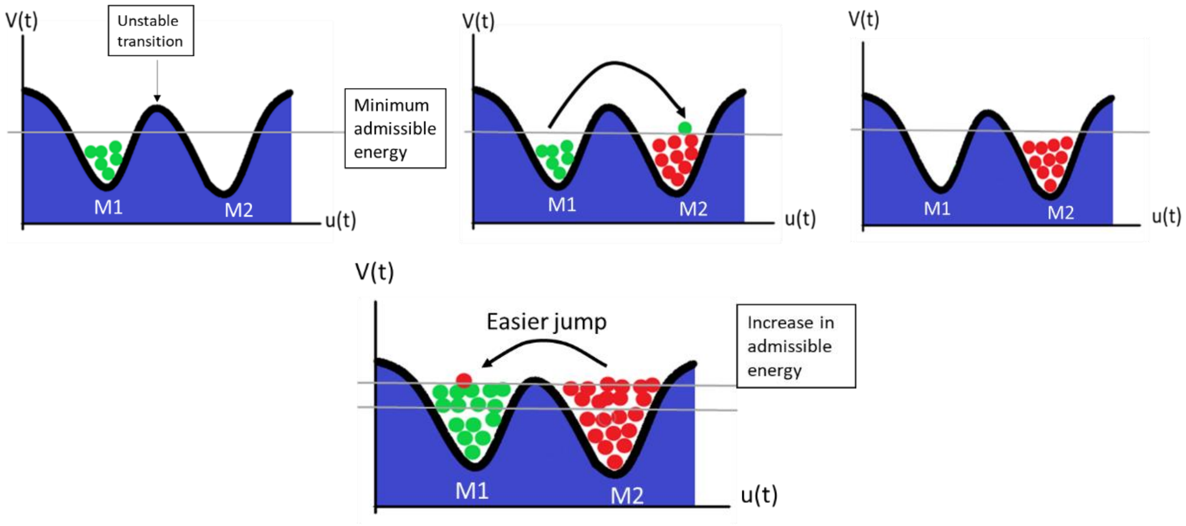

Figure B. 1 – Double well energy model analogy for the bistable phenomenon.

APPENDIX C Papers

The following papers are referent to the results concerning to the development of this theses.

Submitted and waiting for review:

OST, ANA P.; MÖLLER, S. V.. On the strange attractor of the bistable phenomenon behind two parallel cylinders in cross flow. Submitted to: **Meccanica** in nov/19/2021.

Submitted and published in journals and congress proceedings:

OST, ANA PAULA; NEUMEISTER, ROBERTA FÁTIMA; MÖLLER, SERGIO VIÇOSA. Analysis of wake velocities and pressure fluctuations in a bistable flow using Hilbert-Huang transform and wavelets. **Journal of the Brazilian Society of Mechanical Sciences and Engineering**, v. 43, p. 65, 2021.

OST, ANA; NEUMEISTER, ROBERTA FATIMA; MÖLLER, S. V.. Statistical Analysis Of A Bistable Flow Velocity Signal. In: 18th Brazilian Congress of Thermal Sciences and Engineering, 2020, Online Conference. **18th Brazilian Congress of Thermal Sciences and Engineering**, 2020

OST, ANA; PAULA, A. V. ; MÖLLER, S. V. . Signal analysis through the ensemble empirical mode decomposition and Hilbert-Huang transform -application to vortex shedding. In: Jose Manoel Balthazar. (Org.). **Springer-IFTOMM Series of Vibration Engineering and Technology of Machinery Proceedings** - VETOMAC XV 2019. 1ed.Berlin: Springer verlag, 2020, v. 95, p. 82-108.

OST, ANA; NEUMEISTER, ROBERTA FATIMA ; VIÇOSA MÖLLER, SERGIO . Hilbert-Huang Transform Applyed With Deterministic Perturbation And White Noise On Wake Signals From Cylinder With Tripwire. In: 25th International Congress of Mechanical Engineering, 2019, Uberlândia. **Proceedings of the 25th International Congress of Mechanical Engineering**, 2019.

NEUMEINSTER, R. F.; OST, A. P. ; MÖLLER, S. V. . Characteristics of the Wake After a Cylinder With Tripwire On Turbulent Crossflow. In: **EPTT2018 - XI Escola de Primavera de Transição e Turbulência**, 2018.

OST, A. P.; NEUMEINSTER, R. F. ; MÖLLER, S. V. . Analysis Of Wake Velocities And Pressure Fluctuations In A Bistable Flow Using Hilbert-Huang Transform And Wavelets. In: **ENCIT 2018 17th Brazilian Congress of Thermal Sciences and Engineering**, 2018, Águas de Lindóia.

OST, A. P.; MÖLLER, S. V.. Analysis Of The Switching Flow After Two Cylinders Side-By-Side Submitted to a High Turbulence Impinging Flow. In: **COBEM 2017 - 24th ABCM International Congress of Mechanical Engineering**, 2017, Curitiba. COBEM 2017, 2017.